

ORGAN-SPECIFIC, MULTIMODAL, WIRELESS OPTOGENETICS FOR HIGH-  
THROUGHPUT PHENOTYPING OF PERIPHERAL NEURAL PATHWAYS

A Dissertation

by

WOO SEOK KIM

Submitted to the Office of Graduate and Professional Studies of  
Texas A&M University  
in partial fulfillment of the requirements for the degree of

DOCTOR OF PHILOSOPHY

Chair of Committee,	Sung Il Park
Committee Members,	Byung-Jun Yoon
	Jun Zou
	Stephen Maren
Head of Department,	Aniruddha Datta

May 2021

Major Subject: Electrical Engineering

Copyright 2021 Woo Seok Kim

## ABSTRACT

In this study, I introduce an organ-specific scalable, multimodal, wireless optoelectronic device for precise and chronic optogenetic manipulations *in vivo*. When combined with an advanced, coil-antenna system and a multiplexing strategy for powering eight individual home cages using a single radio-frequency transmitter, the proposed wireless telemetry enables low cost, high-throughput, and precise functional mapping of peripheral neural circuits, including long-term behavioral and physiological measurements. Deployment of these technologies revealed an unexpected role for the stomach, non-stretch vagal sensory fibers in suppressing appetite, and demonstrated the durability of the miniature wireless device inside harsh gastric conditions. Together with an advanced machine learning algorithm and a novel switching mechanism, it enables experiments that can anatomically and physiologically map the functions of each targeted organ on the feeding control system in a freely behaving animal in a high-throughput manner.

## DEDICATION

*I dedicate this dissertation to my love Yoon Sung, who has entirely supported me throughout this journey.*

## ACKNOWLEDGEMENTS

I would like to express my deep appreciation to my advisor and committee chair, Dr. Sung Il Park for his thorough guidance and support during my graduate studies at Texas A&M University. I also want to thank my committee members, Dr. Byung-Jun Yoon, Dr. Jun Zou, and Dr. Stephen Maren for their encouragement and support throughout this research.

Thanks also to all our group members, Sungcheol Hong, Milenka Gamero, and Hyun-Myung Woo. And I would like to acknowledge my great collaborators: Dr. Carlos Campos and Dr. Richard D. Palmiter at the University of Washington; Dr. Vivekanand Jeevakumar, Clay M. Smithhart, and Dr. Theodore J. Price at the University of Texas at Dallas; Dr. Minju Jeong and Dr. Byungkook Lim at the University of California at San Diego; Dr. M. Ibrahim Khot, Thomas Maisey, and Dr. David G. Jayne at University of Leeds, UK; Dr. Ling Bai, Dr. Brooke C. Jarvie, and Dr. Zachary A. Knight at the University of California at San Francisco; MD. Clinton Morgan at Barrow Neurological Institute; Dr. Jianfeng Liu at Texas A&M University. I thank my friends, colleagues, faculty, and staff for making my time at Texas A&M University a great experience. Also, I want to express special thanks to Dr. Yilhwan You and Jeongyeol Kim for their friendship and valuable discussion.

Finally, thanks to my wife, parents, parents-in-law, brother, and brother-in-law for their unconditional love, guidance, support, and encouragement in everything I have done. And always thanks to Yoosilhoe members and our captain.

## CONTRIBUTORS AND FUNDING SOURCES

### **Contributors**

This work was supervised by a dissertation committee consisting of Dr. Sung Il Park (chair), Dr. Byung-Jun Yoon, Dr. Jun Zou of the Department of Electrical and Computer Engineering, and Dr. Stephen Maren of the Department of Psychological and Brain Science.

The data analyzed for Chapter 4 was provided by Dr. Carlos Campos. The Finite Element-Method analysis depicted in Chapter 2 and 3 were conducted in part by Sungcheol Hong and Milenka Gamero. The data analysis of machine learning depicted in Chapter 3 was conducted in part by Hyun-Myung Woo of the Department of Electrical and Computer Engineering.

All other work conducted for the dissertation was completed by the author independently.

### **Funding Sources**

Graduate study and this dissertation research were supported by a fellowship from Texas A&M University.

This work was also made possible in part by grants from the interdisciplinary X-Grants Program, part of the President's Excellence Fund at Texas A&M University, and by funding (EEC-164851) from the Engineering Research Center for Precise Advanced Technologies and Health Systems for Underserved Populations (PATHS-UP).

## NOMENCLATURE

3D	Three-dimensional
ANT	Antenna
Cu	Copper
FEM	Finite element-method
GI	Gastrointestinal
HF	High frequency
IC	Integrated circuit
LED	Light-emitting diode
$\mu$ C	Microcontroller
$\mu$ LED	Microscale light-emitting diode
ML	Machine learning
MUX	Multiplexer
NFC	Near-field communication
NTS	Nucleus tractus solitarius
PBS	Phosphate buffered saline
PBN	Parabrachial nucleus
PI	Polyimide
PNS	Peripheral nervous system
PDMS	Polydimethylsiloxane
RF	Radio frequency

RTPP	Real-Time, Place-Preference
RX	Receiver
TX	Transmission
UHF	Ultra-high frequency
UV	Ultraviolet

## TABLE OF CONTENTS

	Page
ABSTRACT .....	ii
DEDICATION .....	iii
ACKNOWLEDGEMENTS .....	iv
CONTRIBUTORS AND FUNDING SOURCES.....	v
NOMENCLATURE.....	vi
TABLE OF CONTENTS .....	viii
LIST OF FIGURES.....	x
LIST OF TABLES .....	xv
1. INTRODUCTION.....	1
2. ORGAN-SPECIFIC, SCALABLE, MULTIMODAL WIRELESS GASTRIC OPTOGENETIC IMPLANTS .....	7
2.1. Introduction .....	7
2.2. Methods.....	9
2.2.1. Device Fabrication .....	9
2.2.2. Finite Element-Method Analysis.....	12
2.2.3. Measurements of Mechanical, Optical, and Electrical Characteristics .....	12
2.3. Results .....	14
2.3.1. Characteristics of Organ-Specific, Wireless Gastric Optogenetic Implants ..	15
2.3.2. Characteristics of Dual-channel Gastric Optogenetic Implants .....	20
2.4. Discussions.....	24
2.4.1. Necessities for Increasing Device Life Span.....	24
2.4.2. Extension to Multichannel Gastric Optogenetic Implants .....	25
3. LOW-POWER, MULTICHANNEL WIRELESS TELEMETRY .....	27
3.1. Introduction .....	27
3.2. Methods.....	31
3.2.1. Fabrication of Dual-coil Antenna and Power Control System.....	31



3.2.2. Finite Element-Method Analysis.....	33
3.2.3. Characterization of Wireless Telemetry.....	33
3.2.4. Modification to DeepLabCut (DLC) Model .....	34
3.2.5. Quantitative Performance Assessment of the ML-Enabled Motion Tracking Algorithm.....	35
3.3. Results .....	36
3.3.1. Time Division Multiplexing.....	36
3.3.2. Dual-coil Antenna System.....	39
3.3.3. Machine Learning-Enabled Real-Time Motion Tracking of Multiple Animals .....	44
3.4. Discussions.....	50
3.4.1. Advanced Antenna Structure.....	50
3.4.2. Expansion of Time Division Multiplexing.....	51
3.4.3. Optimized Multi-coil Antenna System via an ML-based Algorithm.....	52
3.4.4. Applications to Scalability Using ML Algorithms.....	53
 4. <i>IN VIVO</i> VALIDATION OF THE PROPOSED WIRELESS TELEMETRY SYSTEM.....	 55
4.1. Introduction .....	55
4.2. Methods.....	56
4.2.1. Organ-Specific, Wireless, Gastric Optogenetic Device Implantation.....	56
4.2.2. Meal-Pattern Analysis .....	57
4.2.3. Fasting and Refeeding Experiments.....	57
4.2.4. Real-Time, Place-Preference and Open-Field Assays .....	58
4.2.5. Statistics.....	58
4.3. Results .....	59
4.3.1. Measurements of Light Propagation in the Stomach .....	59
4.3.2. Sham Study.....	62
4.3.3. Optogenetic Manipulation of Gastric Vagal Sensory Endings .....	63
4.4. Discussions.....	72
4.4.1. Chronic Stimulation of Vagal Nerve Endings in Obese Animals .....	72
 5. CONCLUSIONS.....	 75
 REFERENCES.....	 79
 APPENDIX A THE CODE AND DATA SAMPLES FOR 3D RECONSTRUCTION IMAGE.....	 97

## LIST OF FIGURES

	Page
Figure 2-1. Device layout of the proposed device. ....	11
Figure 2-2. Illustration of a soft, wireless gastric optogenetic implant in a mouse model. ....	13
Figure 2-3. Procedures for device fabrication; scale bar 5 mm. ....	14
Figure 2-4. 3D modeling of the bending stress results by mechanical simulation for the pre-curved (left) and post-curved (right) structures.....	16
Figure 2-5. Device lifetime cycling test for both structures when strain applied in the vertical (left) and horizontal (right) direction. ....	17
Figure 2-6. Equation for various curvatures of a tether (left). Device lifetime cycling test as three different curvatures (right).....	17
Figure 2-7. Durability test as various temperatures <i>in vitro</i> ; measurements of optical output power from devices when immersed in 10 % PBS at various temperatures, 25 °C, 60 °C, and 90 °C. ....	18
Figure 2-8. Thermal assessment of the proposed device. A device mounted on a sealed bag of 10 % PBS solution, immersed in saline solution, and itself in a cage, respectively. Plots of optical intensity as a function of time at duty cycle (a; 5 %) and (b; 10 %) in three different conditions; wet, dry, and PBS bag.....	19
Figure 2-9. An experimental assay with computed SAR distributions on a mouse mesh body.....	19
Figure 2-10. Measurement of device lifetime for pre- and post-curved structure when implanted (pre-curved, $n = 8$ ; post-curved, $n = 8$ ). Bar graphs are mean $\pm$ SEM. Statistical comparison was made using a two-tailed $t$ -test; *** $p < 0.001$ . ....	20
Figure 2-11. Illustration of wireless operation of a scalable, multimodal wireless gastric optogenetic implant (left), photos of an animal with the device implanted (middle), and photos of the device (right); scale bar 1 cm. ....	21
Figure 2-12. Dual-channel device circuit diagram: $C_{mat} = 412$ pF, $C_{rec} = 0.1$ $\mu$ F, $R_1 = 5$ k $\Omega$ , $R_2 = 20$ k $\Omega$ , $C_1 = 100$ pF, LED1 is green, LED2 is blue. ....	22

Figure 2-13. Flowchart of switching mechanism by a reed switch on the dual-channel device. ....	22
Figure 2-14. Dual-channel device circuit diagram based on memory logic: $C_{\text{mat}} = 412$ pF, $C_{\text{rec}} = 0.1 \mu\text{F}$ , $R_1 = 249 \text{ k}\Omega$ , $R_2 = 10 \text{ k}\Omega$ , $R_3 = 5 \text{ k}\Omega$ , $C_1 = 1 \mu\text{F}$ , LED1 is green, LED2 is blue, and $S_1 = S_2 = 1 \times 2$ analog switch. ....	24
Figure 3-1. Simulation results of electromagnetic couplings induced in an adjacent cage as a function of the distance between two cages along the horizontal (a), vertical (b), and diagonal (c) axes, respectively at a transmitted power level of 4 W. ....	28
Figure 3-2. Schematic illustration of the multiple cage wireless power TX system for high-throughput phenotyping of neural pathways. ....	36
Figure 3-3. Functional block diagram of the proposed wireless power TX system. ....	37
Figure 3-4. Electromagnetic simulation of wireless coverage for the proposed system (left) and a photo of the system (right). ....	38
Figure 3-5. Illustration of an antenna layout (top) and distribution of electromagnetic simulation of wireless coverage in a cage (bottom) for the proposed system (a) and single-coil antenna structure (b), respectively; scale bar 10 cm. ....	40
Figure 3-6. (a) Representative image of a cage with the proposed antenna coils installed. (b) Distributions of the electromagnetic field in a cage at each distance from the bottom. (c) Illustration of the measurement setup. (d) Measurements of output power at 5 different locations of the cage as a function of the distance along the z-axis. Dotted lines indicate the threshold electrical power (0.58 mW) required for the activation of light-sensitive opsins; 0.58 mW electrical power corresponds to an optical power of $10.12 \text{ mW mm}^{-2}$ . (e) Representative images of wireless operation in the cage at each distance. (f) Corresponding distributions of the electromagnetic field in the cage at each distance from the bottom. ....	41
Figure 3-7. Plots of a residual dependence of transmitted power on relative orientation angle between the TX antenna and the implantable device as a function of the angle, $15^\circ$ (a), $45^\circ$ (b), $75^\circ$ (c), and $85^\circ$ (d). Green dotted lines indicate 70 % higher (1 mW) than threshold electrical power level (0.58 mW) required for activation of light-sensitive proteins; 1 mW electrical power corresponding to an optical power of $17.44 \text{ mW mm}^{-2}$ . ....	42
Figure 3-8. Comparisons of wireless coverage; 1. Proposed dual-coil antenna, 2. Single-coil & dual-layered antenna[75], 3. a tilted antenna design with a	

time division multiplexing schematic[66], and 4.Single-coil & single-layered antenna at the TX power level of 1 W. ....	42
Figure 3-9. Illustration of antenna layouts (top) and 3D reconstructions of traces of an operating indicator LED (bottom): proposed dual-coil antenna (a), and single-coil antenna structure (b), respectively. ....	43
Figure 3-10. Overview of ML-enabled adaptive wireless TX system .....	45
Figure 3-11. Illustration of a step-by-step procedure for the ML algorithm.....	46
Figure 3-12. Two representative images were processed by the ML algorithm. The top image shows perfect alignments of five vectors with a selected coil antenna while the bottom image includes only three vector assignments. It is likely for the two non-assigned mice (or implanted devices) to receive not enough power due to a misalignment between an implanted device and a selected coil antenna. ....	47
Figure 3-13. Assessment of detection accuracy for three different antenna structures: 1. 4-coil (each two coil antennas are on the x- and y-axis, respectively), 2. Dual-coil (along the x-axis), and 3. Dual-coil (along the y-axis).....	48
Figure 3-14. Statistics of the number of frames for two representative cases; how long a selected antenna remains activated (a) and how many frames (how long an interval) exist between activation of an antenna and reactivation of itself after the first deactivation (b); 1. 4-coil (each two coil antennas are on x and y-axis, respectively), 2. Dual-coil (along the x-axis), and 3. Dual-coil (along the y-axis). ....	49
Figure 3-15. The advanced dual-coil and dual-layered configurations: (a) top is flat and bottom is diagonal-shaped; (b) top is diagonal-shaped and bottom is flat; and (c) top and bottom are diagonal-shaped. ....	51
Figure 4-1. Illustration of a soft, wireless gastric optogenetic implant: device implants location (left and middle) and a photo of wireless LED operation in the stomach of a mouse (right); scale bar 5 mm. ....	59
Figure 4-2. Light intensity measurements comparing LED implantation inside versus outside the stomach ( $n = 5, p < 0.01$ ), with varying RF powers ( $p < 0.001$ ). Dashed horizontal lines indicate light intensity needed for 10 % and 50 % maximal activation of channelrhodopsin2. Bar graphs are mean $\pm$ SEM. Statistical comparisons were made using two-way repeated-measures ANOVA, Tukey's post hoc; *** $p < 0.001$ . ....	60

- Figure 4-3. Light intensity measurements during varying RF wireless powering ( $p < 0.001$ ) of the gastric optogenetic device ( $n = 5$ ) and varying distances ( $p < 0.001$ ) from the LED. Measurements were taken from the front side (a), back side (b), and lateral side of the LED (c). Bar graphs are mean  $\pm$  SEM. Statistical comparisons were made two-way repeated-measures ANOVA; \*\*\*  $p < 0.001$ . .....61
- Figure 4-4. Comparison of total food intake (left), number of meals (middle), and meal size (right) in mice implanted with LED device ( $n = 7$ ) or sham operated ( $n = 6$ ) ( $p = 0.71$ ). Bar graphs are mean  $\pm$  SEM. Statistical comparisons were made using two-way repeated-measures ANOVA, Tukey's post hoc. ....63
- Figure 4-5. Schematic illustration of the activation of *Calca*<sup>+</sup> stomach vagal afferents. *Calca*-Cre transgenic mice received a left nodose ganglion injection of AAV9-DIO-ChR2:tdTomato or AAV9-DIO-tdTomato control virus. The LED was implanted in the stomach corpus-function junction.....64
- Figure 4-6. *Calca*-Cre transgenic mice received nodose ganglion injection of AAV9-DIO-ChR2:tdTomato. Images show fluorescence *in situ* hybridization of tdTomato and *Calca* mRNA, demonstrating the cell-type specificity of transgenic/viral approach; scale bars 25  $\mu$ m.....64
- Figure 4-7. tdTomato fluorescence labeling of central *Calca*<sup>+</sup> vagal afferent endings in the nucleus of the solitary tract (NTS); scale bar 25  $\mu$ m. ....65
- Figure 4-8. Fluorescence labeling of peripheral *Calca*<sup>+</sup> vagal afferent endings in the stomach mucosal layer; scale bar 50  $\mu$ m. ....66
- Figure 4-9. Frequency-dependent suppression of food intake in the ChR2:tdTomato group ( $n = 8$ ). (c) The tdTomato control group did not suppress food intake during photostimulation ( $n = 4$ ) ( $p = 0.06$ ). Bar graphs are mean  $\pm$  SEM. Statistical comparisons were made using two-way repeated-measures ANOVA, Tukey's post hoc; \*\*\*  $p < 0.001$ . ....66
- Figure 4-10. Abdominal activation of *Calca*<sup>+</sup> vagal afferent fibers. (a) Picture showing wirelessly powered LED device; two of these devices were inserted into the abdomen of *Calca*-Cre transgenic mice with left nodose ganglion injection of AAV9-DIO-ChR2:tdTomato or AAV9-DIO-tdTomato control virus; scale bar 5 mm. (b) top, frequency-dependent suppression of food intake during ChR2 activation of vagal afferents ( $n = 8$ ), bottom, no appetite suppression in tdTomato control group ( $n = 4$ ) ( $p = 0.80$ ). (c) Percent reduction of food intake (compared to RF off) during 10 and 20 Hz stimulation of *Calca*<sup>+</sup> vagal afferent endings using the stomach LED implant or non-attached LEDs (ChR2,  $n = 8$  per group) (interaction,  $p =$

0.01). Bar graphs are mean $\pm$ SEM. Statistical comparisons were made two-way repeated-measures ANOVA, Tukey's post hoc; * $p < 0.05$ ; ** $p < 0.01$ ; *** $p < 0.001$ .	67
Figure 4-11. Schematic illustration of an experimental assay (top) and distributions of the electromagnetic field in the assay (bottom) for open-field (a) and RTPP (b), respectively.	68
Figure 4-12. Activation of the LED device (20 Hz light pulses) did not induce a place preference nor avoidance in both Chr2 and tdTomato groups ( $n = 7$ per group) (left). Representative traces for RTPP assay (right). Bar graphs are mean $\pm$ SEM. Statistical comparisons were made using two-way repeated-measures ANOVA, Tukey's post hoc.	69
Figure 4-13. Photoactivation (20 Hz light pulses) of <i>Calca</i> <sup>+</sup> gastric vagal afferents decreased time spent in center of large open field box ( $n = 7$ per group) ( $p = 0.31$ ) (left). Representative traces from open-field test (right). Bar graphs are mean $\pm$ SEM. Statistical comparisons were made using two-tailed <i>t</i> -tests; ** $p < 0.01$ .	70
Figure 4-14. Locomotor activity comparison in the assays for RTPP (left), and open-field box (right). Both were conducted for 30 minutes and $n = 7$ per each group. Bar graphs are mean $\pm$ SEM. Statistical comparison was made using two-tailed <i>t</i> -test; *** $p < 0.001$ .	70
Figure 4-15. Mice were exposed to a novel sucrose solution on Day 1 followed by optogenetic activation of vagal sensory fibers (20 Hz). On Day 5, mice were water-restricted overnight and then given simultaneous access to a bottle of sucrose and a bottle of water. The graph is the sucrose preference score (Chr2, $n = 7$ ; tdT, $n = 5$ ). Bar graphs are mean $\pm$ SEM. Statistical comparisons were made using two-tailed <i>t</i> -tests; *** $p < 0.001$ .	71

## LIST OF TABLES

	Page
Table 2-1. Summary of procedures for fabrications.....	10
Table 2-2. Components information used for the wireless gastric optogenetic implant..	11
Table 3-1. Summary of customized TX antenna specification .....	32

## 1. INTRODUCTION

Optogenetics encompasses a technology that can rapidly control the function (gain or loss) of well-defined events within specific cells of complex biological systems, such as freely moving mammals[1]–[5]. This technology introduces microbial opsin genes to allow optical control of defined action potential patterns with the speed (millisecond-scale) and precision (cell-type-specific) required for biological processing in specific targeted neuron populations of living tissues. Therefore, optogenetics fundamentally requires an interdisciplinary perspective: engineered control tools that can easily target interesting cells, technology for light delivery into the tissue, and compatible readouts and analysis on how the optical control has been integrated.

From a biological perspective, since the first bacteriorhodopsin was recognized as a microbial single-component light-activated ion pump decades ago[6], many studies have not only reported a deeper understanding of bacteriorhodopsin, but also identified numerous microbial opsins. The microbial opsin family includes membrane-bound ion pumps, as well as channel-system pathways such as halorhodopsin[7] and channelrhodopsin[8], which can pass through many ions in and out of the cell membrane in response to light[7]–[14]. Despite the long-standing understanding of such widely known microbial opsin genes and their ability to mediate ion conductivity through single-component light-activation regulators, studies related to optical neural control have stalled for decades due to assumptions that optoelectronic currents are too weak and slow to control neurons efficiently. Accordingly, mammalian neuronal microbial



membrane proteins are not expressed as intended. However, the situation changed rapidly in 2005 after the introduction of a single-component microbial opsin gene into mammalian neurons, which allowed stable, precise, and continuous control of action potentials on a millisecond timescale[15]. Since then, numerous studies[16]–[19] have actively demonstrated that many types of ionic conductive microbial opsins can be used as optogenetic control tools in mammalian neurons, such as a mature mammalian brain[1], [20], and spinal tissues[21]. In short, the optogenetic approach has exposed a new context for biological research, including both aspects of health and disease, by providing optical control at the speed and precision required for biological control processing.

The first step in exploiting optogenetics technology is to target the opsins to the desired cells[22]–[28]. However, this stage is biologically oriented and beyond the scope of this dissertation, so I merely mention how it has evolved based on the following categories: viral promoter targeting, projection targeting, transgenic animal targeting, and spatiotemporal targeting. Once the desired opsin is targeted to the neurons of interest, the most important factor in the technology is how precise the light delivery and optical control can be in the targeted region[15], [29]. The requirements vary greatly depending on the experimental design. For example, multiple-opsin studies of rapid oscillations in brain sections require a different light delivery approach[30] than the studies of long-term stimulatory effects of the deep brain region in behavioral animals[22], [31], [32]. Also, in experiments that require long-term or light delivery to

spinal tissue, the spatial, temporal, and spectral control of the lighting must be well defined before lighting requirements of a particular experimental application can be met.

Early optogenetics began with *ex vivo* experiments for light to target surfaces, such as cultured neurons, brain fragments, and cortical surfaces[30], [33], [34]. However, the system was gradually applied to freely moving worms[35], [36] and individual living cells in the brain of animals[37], [38], opening up a new era in neuroscience. Experiments that transmit light *in vivo* present several distinct hurdles compared to *in vitro* experiments. The light should be able to illuminate the precise region of the deep brain on demand, minimizing damage to surrounding tissue, and should not significantly interfere with the natural behavior of the animal. To meet these requirements, researchers suggested optical neural interfaces to deliver light directly from light sources (typically lasers) to target areas *in vivo* using a thin optical fiber[22], [31]. They then continued to develop into interfaces that attached to the skull by permanent implantation of a short-length fiber ending in a small fiber-optic connector with the inserted cannula in the target brain region. This method provides chronic experiments for several reasons: 1) the exposed fibers are less damaging than large cannulas, 2) the brain is completely secured from the external environment, and 3) the pairing connectors are less destructive than when inserting fibers into the cannula. These systems as early solutions leveraged the stable nature of the brain-skull interface to enable continuous optogenetic modulation of the identified neural groups.

Nevertheless, these tethered systems impose significant constraints on experimental design and interpretation. In addition to requiring the researcher to attach

the optical fibers to the animals before conducting the behavioral tests, the connectors, including the inserted cannula, are physically bound to static skeletons of the animals, such as the skulls, to secure the fiber cables. This external fixation can cause device failure or injury to the nerve tissue around the inserted cannula due to inadvertent damage by the cage mate or housing[39], [40]. Also, these attached optical fibers physically restrict animal behavior, thus hindering the animal's natural movements in complex environments. Hence, there has been extensive effort to deliver light through a wireless head mount system: fortuitously, the researchers have achieved their goals by combining flexible, injectable LED systems and options for wireless power supply via head-mounted receivers or battery-powered module devices[41]–[43]. However, such wireless optogenetic technology is also restricted by the mass and size of the device[43], [44]. The known wireless systems weigh between 0.7 g and 3 g and cannot be attached to animals for long periods because they protrude several millimeters from the skin[45]–[47]. These structural restrictions prevent experimental designs that require small cages or normal social interaction with other mice. Thus, the head-mounted device ultimately narrows the extent of the research due to its structural limits and its concentration on only the brain region capable of emitting light.

Because of these constraints, studies in animals that extended beyond the boundaries of these devices and required optogenetic control past brain studies to the spinal cord or PNS remained in unknown territory. However, research in 2015 introduced a miniaturized, fully implantable biocompatible device that can safely interface with peripheral nerves and illuminate areas where light source delivery is

tricky[48], [49]. These devices can specifically and reversibly activate peripheral and spinal cord pain circuits in freely moving mice. The significance of research beyond the brain can also be perceived by noting the vagus nerve, which provides the only direct neural communication between internal organs and the brain. Peripheral endings of the vagal afferent fibers respond to a broad array of stimuli, including hormones, osmolytes, changes in pH, and mechanical distention that have diverging functions and contributions to behavior[50]. All of its diverse sensory cell bodies reside together within the nodose ganglia[50] but conventional viral and transgenic methods for targeting genetically distinct neuronal populations do not permit organ-specific manipulations. Although pioneering studies have used fiber optics to optogenetically manipulate mouse vagal afferents with organ specificity, these studies were conducted under anesthesia to investigate autonomic functions[51], [52]. Accordingly, studying functions beyond reflexes, such as the phenomenon of satiation in GI tracts, requires a more flexible approach. Given the widespread interest in using vagal nerve stimulation for treating obesity and other neurological disorders[53], [54], a key priority for this research field is to attain cell-type and organ-specific manipulations of the vagus nerve in awake animals. Although the aforementioned studies have attempted to implant devices into animal body parts beyond the brain region, no device has yet enabled chronic and durable cell-type-specific optogenetic manipulation of peripheral neurons within an organ.

In this dissertation, I describe the development of a durable, multimodal, wireless platform that enables chronic optogenetic stimulation of peripheral neurons

within organs in a high-performance manner. The miniaturized wireless device is fully implantable, utilizing a soft, thin, and low-modulus tether with a  $\mu$ LED for targeting inside an organ. A unique fabrication method is employed to offer a robust,  $\mu$ LED-housing tether, permitting long-term (>1 month), intimate interfacing with peripheral nerve endings in freely behaving mice. Combined with multichannel stimuli interfaces, these optogenetic implants can selectively and independently manipulate peripheral nerve activity within multiple target organs in the same animal using a monolithic design. Additionally, a channel isolation strategy is introduced for powering multiple cages using a single RF transmitter. Coupled with an advanced coil-antenna approach, a single telemetry system provides reliable wireless power in eight individual home cages, overcoming cage limitations of other wireless and fiber-optic-based systems. Furthermore, the concept of a channel isolation power TX system combines ML-based image processing technology in real-time to avail the chance of stable animal experiments in a large-scale cage with multiple mice at the same time. The utilities of the proposed wireless telemetry system have been demonstrated in an animal model, and in vivo deployment of this technology revealed an unexpected role for putative, gastric chemoreceptors in suppressing appetite and unveiled a valence mechanism by which appetite suppression occurs.

## 2. ORGAN-SPECIFIC, SCALABLE, MULTIMODAL WIRELESS GASTRIC OPTOGENETIC IMPLANTS\*

### 2.1. Introduction

Wireless optoelectronics has provided a way to bypass the physical limitations of fiber-optic cables to some extent[41]–[43], [47], [48], and this development has resulted in a fully implantable wireless device with reduced size and weight. As technology advances, many neuroscientists have gone beyond the brain and have used this optogenetic tool to understand how interconnected groups of peripheral neurons work together to carry out a behavior. However, wireless optogenetics for the PNS has not reached its full potential due to the limited durability of the device, harsh circumstances, such as natural continuous systolic/diastolic movements of an organ, and the difficulty of targeting precisely. Recently, a wirelessly powered  $\mu$ LED secured to a rat bladder using a circumferential elastomer sleeve was found to enable a similar level of functionality[55], but this approach impedes organ expansion. Efforts to wirelessly manipulate neural organ function in awake mice include studies that sutured a  $\mu$ LED onto the heart surface for pacemaking[56] or the intestinal surface for controlling colonic motility[57]. However, these devices were not described as being functional for more than 8 days[55]–[57], limiting behavioral studies subject to the recovery periods required

---

\*Reprinted with permission from “Organ-specific, multimodal, wireless optoelectronics for high-throughput phenotyping of peripheral neural pathways” by Kim, W.S.; Hong, S.; Gamero, M.; Jeevakumar, V.; Smithhart, C.M.; Price, T.J.; Palmiter, R.D.; Campos, C.; Park, S.I, 2021, *Nat Commun*, 12, 157, © 2021 by Springer Nature.

after thoracic and/or abdominal device implantation. Moreover, affixing the  $\mu$ LED to the target organ surface results in light back-scatter and nonspecific optogenetic illumination on nearby tissues. To sum up, these preexisting methods have several drawbacks: restrictions on device reliability due to the natural movement of animals and the correctness of the minute target region due to having to affix the light source on the outside of the specific organ.

Advanced wireless communication modules such as  $\mu$ C-embedded communication systems (NFC hardware or Bluetooth chips) have been described that can function, multichannel operation. Their user-friendly software interface and open-source circuit library provide easy access to the broader community. Although these wireless platform systems have some utilities, the power requirements for wireless operation ( $\sim 3$  mA for a  $\mu$ C-embedded communication system,  $\sim 3.5$  mA for an NFC chip, and  $\sim 10$  mA for a Bluetooth device) make them less ideal for small animal research or longitudinal experiments[17–20]. This could be compensated by an increase in transmitted power, but this could exceed the upper limits suggested by IEEE depending on class of neuroscience experiment[62]. Any exposures above the guidelines could potentially cause tissue damage associated with the absorption of RF signals[63].

In this chapter, I propose a soft, fully implantable HF range optoelectronic device that 1) directly interfaces with vagal afferent fibers in the stomach and 2) delivers light to the nerve endings in a freely behaving animal with chronic stability in operation. I also introduce a low-power, switching mechanism for multichannel operation; it allows for selective control of multichannel up to eight within a limited size (dimension: 1 cm

diameter). Overcoming these technical barriers will enable tools to diversify PNS function by organ-specific stimulation and provide insight into completely understanding the communication between the GI tract and the brain.

## **2.2. Methods**

### **2.2.1. Device Fabrication**

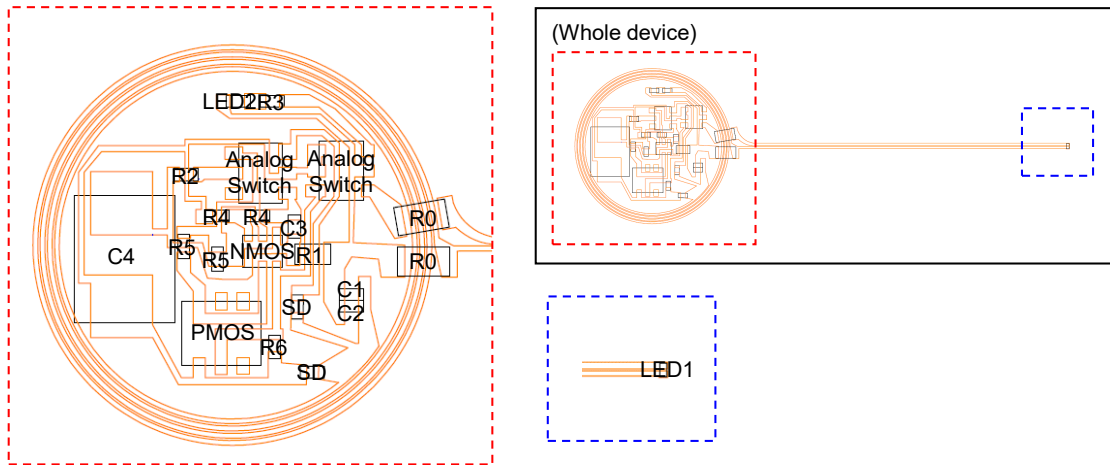
The process began with flexible Cu/PI bilayer films (thickness: 12  $\mu\text{m}$ /18  $\mu\text{m}$ , AC181200RY, Dupont<sup>TM</sup> Pyralux<sup>®</sup>) mounted onto a glass slide (dimensions: 5.08 cm by 7.62 cm). Then we deposited 2.5  $\mu\text{m}$  thickness of photoresistor on the Cu/PI substrate (AZ 1518, AZ<sup>®</sup>, recipe; spin-coated at 4,000 r.p.m. for 20 sec), and used UV lithography to define patterns for pads and interconnections (EVG610, EV Group, recipe; UV intensity for 100  $\text{mJ cm}^{-2}$ ). This was followed by immersion in developer solution (AZ Developer 1:1, AZ<sup>®</sup>) for 30 sec and rinses in distilled water for 10 sec. Immersion in copper etchant (LOT: Z03E099, Alfa Aesar<sup>TM</sup>) for 7 min and rinses with acetone, methanol, isopropanol, and distilled water for 1 min yielded Cu interconnections and pads on the flexible substrate. After samples dry, chip components were mounted, including a  $\mu\text{LED}$ , passive components, and IC components using a soldering machine. An additional PI/Cu layer (thickness: 18  $\mu\text{m}$ /12  $\mu\text{m}$ ) with the bottom chip-mounted Cu/PI substrate formed a sandwiched structure (PI/Cu/Cu/PI). For encapsulations, we applied a small amount of PDMS (Sylgard<sup>TM</sup> 184 silicone elastomer kit, Dow<sup>®</sup>; 10:1 mix ratio) using a pipette while a clamp held the body of a sample to form a thin, pre-curved, sandwiched structure. Then we encapsulated the body of a



sample with PDMS by a dip-coating process (thickness: 500  $\mu\text{m}$ ). Samples were cured in a vacuum oven at 100 °C for 1 h. These procedures yield a soft, low-power, wireless gastric optogenetic implant with a pre-curved, sandwiched tether. The summary of the fabrication procedure is in Table 2-1. And detailed information on device layouts and IC components are found in Figure 2-1 and Table 2-2, respectively.

**Table 2-1.** Summary of procedures for fabrications

	<b>Process</b>	<b>Purpose</b>	<b>Required time for 10 devices</b>	<b>Equipment</b>	<b>Progress level (%)</b>
<b>1</b>	Preparation of photoresist coated glass	Sampling for transfer	1 hour	Clean room Spin-coater	10
<b>2</b>	Baking	Stabilization, remove the solvent	0.5 hours	Clean room Hotplate	20
<b>3</b>	Photo lithography	Patterning for stretchable circuits	1 hour	Clean room Mask aligner	40
<b>4</b>	Photoresist development		0.5 hours	Clean room	50
<b>5</b>	Copper etching		1 hour	Clean room	60
<b>6</b>	Baking	Stabilization, remove the solvent	0.5 hours	Clean room Hotplate	65
<b>7</b>	Components transfer	Active components integration	5 hours	Soldering Iron Microscope	80
<b>8</b>	PDMS encapsulation	System packaging	10 hours	Vacuum oven	100



**Figure 2-1.** Device layout of the proposed device.

**Table 2-2.** Components information used for the wireless gastric optogenetic implant

	<b>Components</b>	<b>Product number</b>	<b>Vendor</b>
<b>LED1</b>	472nm, 220 × 270 × 50 μm	C460TR2227	Cree
<b>LED2</b>	632nm, 0.65 × 0.35 × 0.2 mm	APG0603SEC-E-TT	Kingbright
<b>SD</b>	Schottky Diode, 0.65 × 0.35 × 0.3mm	DSR01S30SL	Toshiba
<b>R0</b>	0 Ω, 1.6 × 0.9 × 0.55 mm	RCWPM-0603	VISHAY
<b>R1</b>	0 Ω, 1.00 × 0.55 × 0.35 mm	RCWPM-0402	VISHAY
<b>R2</b>	0 Ω, 0.65 × 0.35 × 0.25 mm	RCWPM-0201	VISHAY
<b>R3</b>	499 Ω, 0.6 × 0.3 × 0.23 mm	RC0603F4990CS	Samsung EM
<b>R4</b>	249 k Ω, 0.6 × 0.3 × 0.23 mm	RC0603F2493CS	Samsung EM
<b>R5</b>	10 k Ω, 0.6 × 0.3 × 0.23 mm	RC0603J103CS	Samsung EM
<b>R6</b>	20 k Ω, 0.6 × 0.3 × 0.23 mm	RC0603F203CS	Samsung EM
<b>C1</b>	82 pF, 0.6 × 0.3 × 0.33 mm	CL03C820JA3NNNC	Samsung EM
<b>C2</b>	330 pF, 0.6 × 0.3 × 0.33 mm	CL03B331KA3NNNC	Samsung EM
<b>C3</b>	1 μF, 0.6 × 0.3 × 0.33 mm	CL03A105KP3NSNC	Samsung EM
<b>C4</b>	11 mF, 3.2 × 2.5 × 0.9 mm	CPH3225A	Seiko
<b>NMOS</b>	1.0 × 1.0 × 0.34 mm	NTUD3170NZ	ON Semiconductor
<b>PMOS</b>	1.7 × 1.7 × 0.6 mm	NX3008PBKV	Nexperia
<b>A-SW</b>	Analog switch, 1.6 × 1.2 × 0.5 mm	SN74LVC1G3157	Texas Instruments

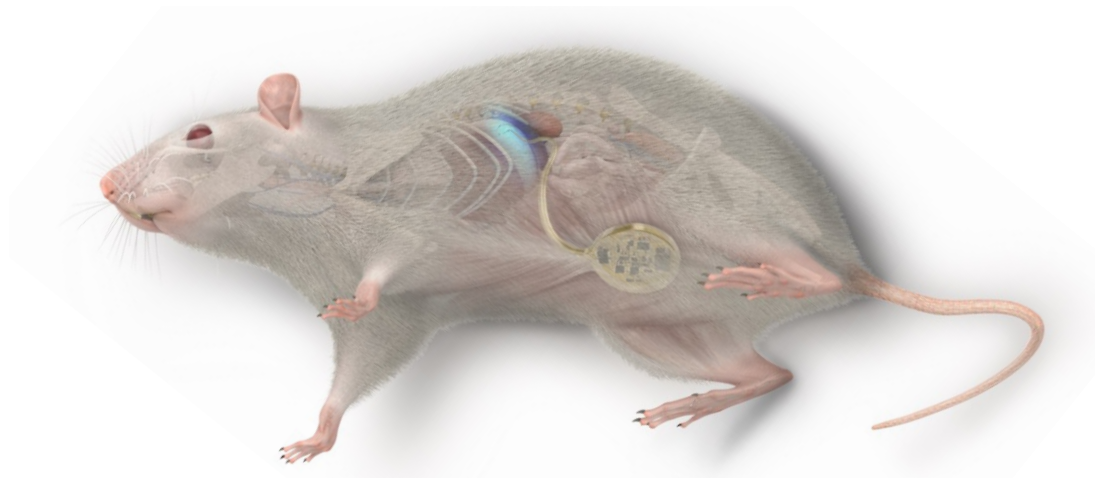
### **2.2.2. Finite Element-Method Analysis**

For numerical electromagnetic simulations of the proposed device, we used a finite element- method analysis tool (Ansys Electromagnetics Suite 17-HFSS, Ansys®) with Cole-Cole dielectric relaxation model where characteristics of biological tissues were described as a function of frequency. Organ systems and tissues of a mouse were modeled to one million meshes for numerical simulations, and antenna coils made of copper stripes or wires were modeled to materials with finite conductivity,  $58 \text{ MS s}^{-1}$ . For 3D modeling of the mechanics for the devices, we used a commercial finite element- method analysis tool (Abaqus/CAE 2018, Dassault Systems) to investigate strain effects on the pre-curved and post-curved structures. The following parameters were used for simulations: 500/18/12/12/18/500  $\mu\text{m}$  thickness (PDMS/PI/Cu/Cu/PI/PDMS) for the pre-curved structure and 510/12/18/510  $\mu\text{m}$  thickness (PDMS/Cu/PI/PDMS) for the post-curved structure; elastic properties Young's modulus MPa/Poisson's ratio: 1/0.49 for PDMS, 119000/0.34 for Cu, and 2500/0.34 for PI. The Cu/PI layer was modeled as a composite shell element (S4R). PDMS was modeled as a solid hexahedron element (C3D8R) in the pre-curved structure and as a shell element (S4R) in the post-curved one.

### **2.2.3. Measurements of Mechanical, Optical, and Electrical Characteristics**

We used a gauge-force machine (ESM303 Forced Test Stand, MARK-10) to perform device lifetime cycling tests with a significant load extended over a period of time (>200 kilocycles) for the pre-curved, post-curved, and pre-curved structures with three different curvatures (0.72 mm, 1.15 mm, and 2.87 mm) of a tether. The

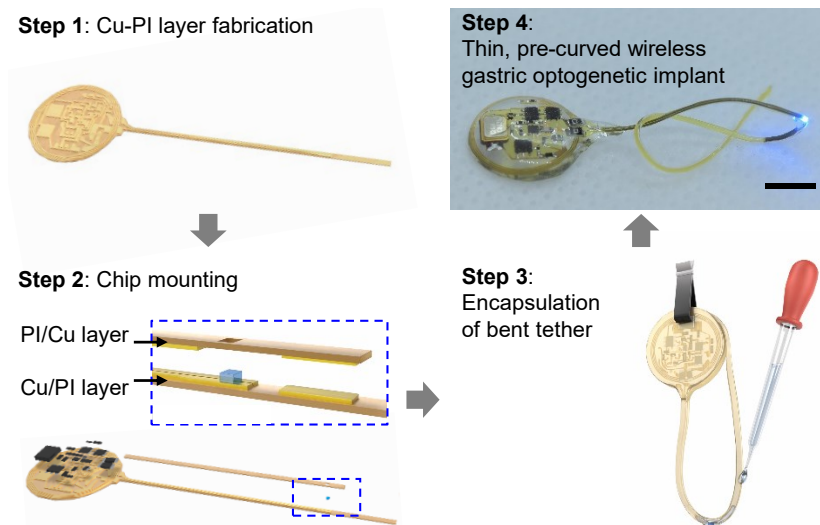
experiments involved application of strain in three different directions: 1) the x-direction, 2) the y-direction, and 3) the z-direction, respectively. After completion of each 1,000 cycles, we immersed a wireless device in 10 % PBS solution for 10 min and measured light intensity using a light meter (LT300, EXTECH). This test was repeated until a device stopped functioning. We also performed accelerated life testing where a device was immersed in 10 % PBS solution and light intensity was monitored as a function of time at various temperatures (25 °C, 60 °C, and 90 °C). For thermal assessments of wireless devices, we used an infrared camera (VarioCAM HDx head 600, InfraTech). Light intensity was fixed at an optical intensity of 10 mW mm<sup>-2</sup>, which is enough to activate light-sensitive proteins, and the camera measured variations in temperature when devices were operated with duty cycles of 20 %, 40 %, 60 %, 80 %, and 100 %.



**Figure 2-2.** Illustration of a soft, wireless gastric optogenetic implant in a mouse model.

### 2.3. Results

An illustration of the fully implantable wireless device shows the general strategy for targeting a  $\mu$ LED inside the stomach (Figure 2-2). The device consists of an analog, front-end electronic circuit for RF harvesting (5.5 mm radius and 1 mm thickness) and a tether that supplies current to a  $\mu$ LED. It harvests RF energy from a remotely located wireless RF power system, converts RF energy into optical energy, and illuminates targeted regions in the stomach. The  $\mu$ LED is situated in the middle rather than the end of a tether, allowing the tether to be threaded in and out of the stomach and secured at two contact points. We found that the tether remains secure with purse-string sutures. The ultra-thin tether (0.4 mm wide by 0.2 mm thick) is more than 3 times smaller than insulin syringe needles used for intraperitoneal injections and tubing used for intragastric infusions[64].

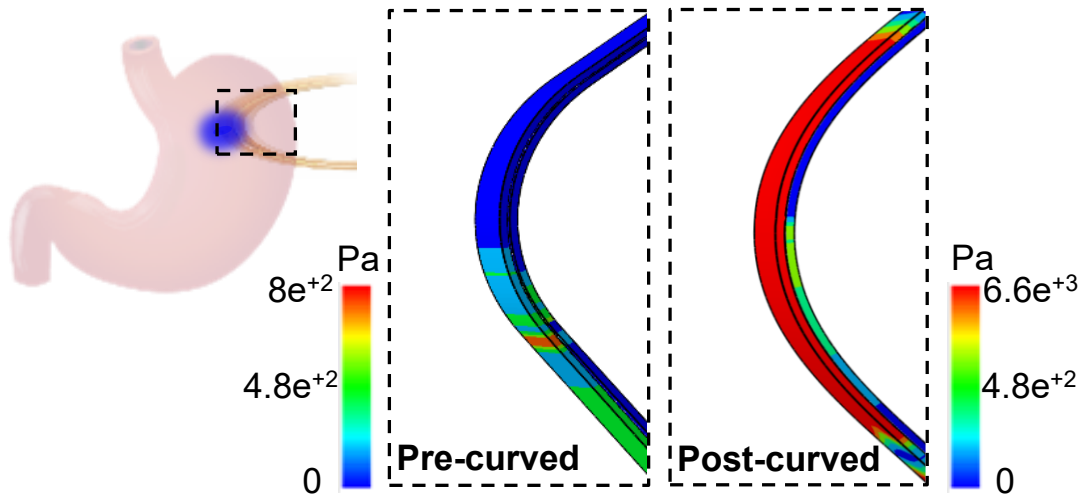


**Figure 2-3.** Procedures for device fabrication; scale bar 5 mm.

### 2.3.1. Characteristics of Organ-Specific, Wireless Gastric Optogenetic Implants

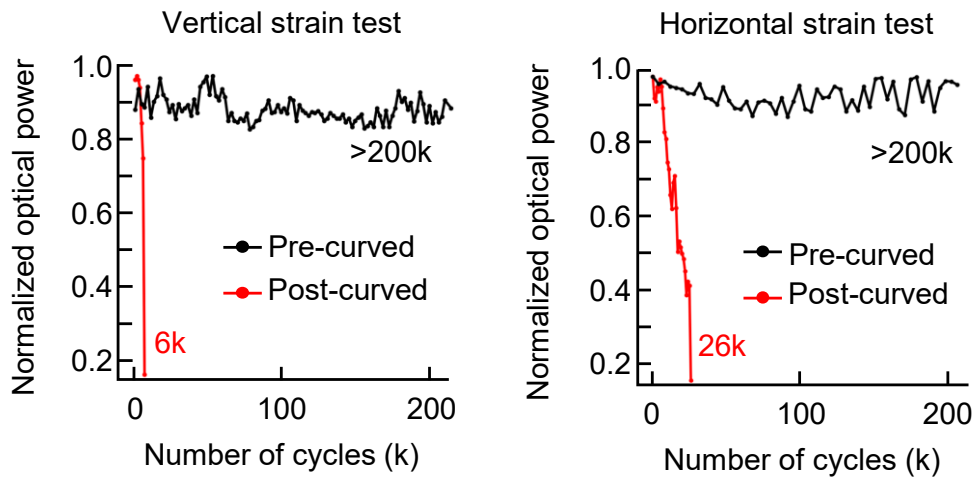
Essential features that allow for long-lasting operation of the ultra-thin tether are a pre-curved, sandwiched construction. In our prototype, the harvester and  $\mu$ LED were connected with thin Cu (12  $\mu$ m) electrical interconnects on top of flexible and durable PI (18  $\mu$ m) substrate, then coated with a biocompatible silicone polymer, PDMS. However, this design exhibited poor durability, and post hoc analysis revealed  $\mu$ LED tether damage likely caused by mechanical strains. To increase durability, the  $\mu$ LED was sandwiched in between a second Cu/PI bilayer, which also provided additional electrical contact (Figure 2-3; assembly steps 1,2). We further postulated that coating the tether with silicone in a curved position (pre-curved) would decrease strain compared to a tether that was coated in a flat orientation and then bent when securing it inside the stomach (post-curved). This was achieved by suspending the tether in a bent position, pipetting small amounts of melted silicone around the  $\mu$ LED, and coating the remaining components using a simple dipping process (Figure 2-3; assembly step 3). This resulted in a thin, soft, and lightweight ( $\sim$ 380 mg), wireless, gastric optogenetic implant (Figure 2-3; assembly step 4). The compliant, low-modulus properties eliminated constraints on natural motions of the animal while also minimizing mechanical strain at the connecting joints.

3D modeling of the mechanics showed that the maximum strain in the Cu traces and PDMS coating of the pre-curved tether ( $<800$  Pa) was dramatically reduced compared to the post-curve tether strain ( $>6,600$  Pa) (Figure 2-4). We further optimized the tether by mechanically testing various curvatures and identified a pre-curved

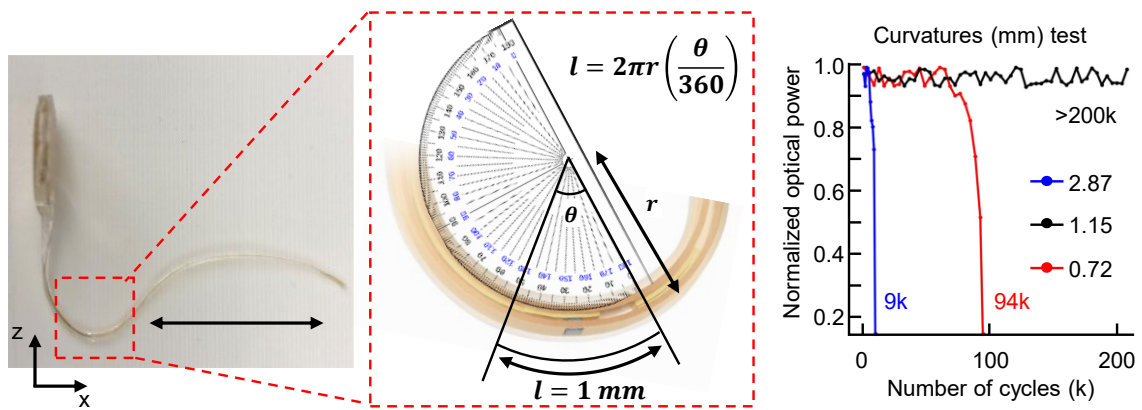


**Figure 2-4.** 3D modeling of the bending stress results by mechanical simulation for the pre-curved (left) and post-curved (right) structures.

configuration that was functional beyond 200 kilocycles. Lifetime mechanical cycle tests with a significant load (0.03 kgF) revealed that the pre-curved structure with a radius of 1.15 mm was functional for 200 kilocycles, a nearly 10-fold improvement compared to the post-curved structure (Figure 2-5). Although there was improved durability with pre-curved structures that had a radius of 2.87 mm and 0.72 mm, they were not as durable as 1.15 mm, likely because 2.87 mm is too similar to the flat structure, whereas the sharp angle with a radius of 0.72 mm interferes with  $\mu$ LED contact with the pad (Figure 2-6). The device was also subjected to waterproof testing by submerging it into a heated saline solution, revealing that it remained continually functional for over two months, even in extreme temperatures (Figure 2-7). Heat dissipation is another factor that can limit device functionality since nerve endings in the GI tract can be temperature sensitive[65].



**Figure 2-5.** Device lifetime cycling test for both structures when strain applied in the vertical (left) and horizontal (right) direction.

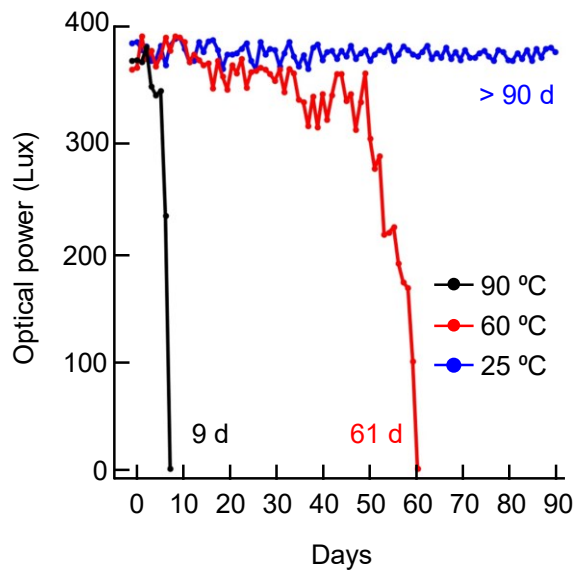


**Figure 2-6.** Equation for various curvatures of a tether (left). Device lifetime cycling test as three different curvatures (right).

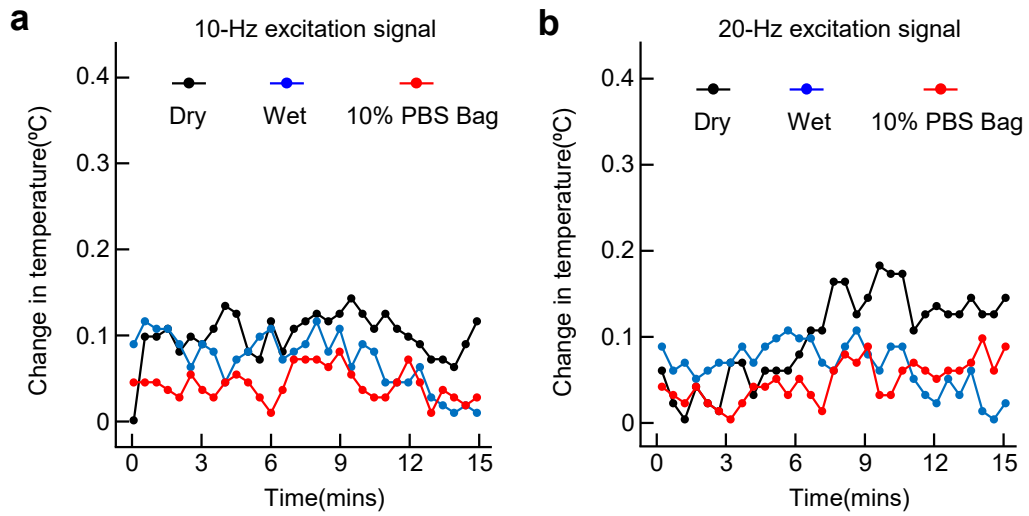
Thermal assessment of the wireless optogenetic implant demonstrated minimal temperature increases ( $\sim 0.2$  °C; Figure 2-8) during typical operating conditions (10 Hz



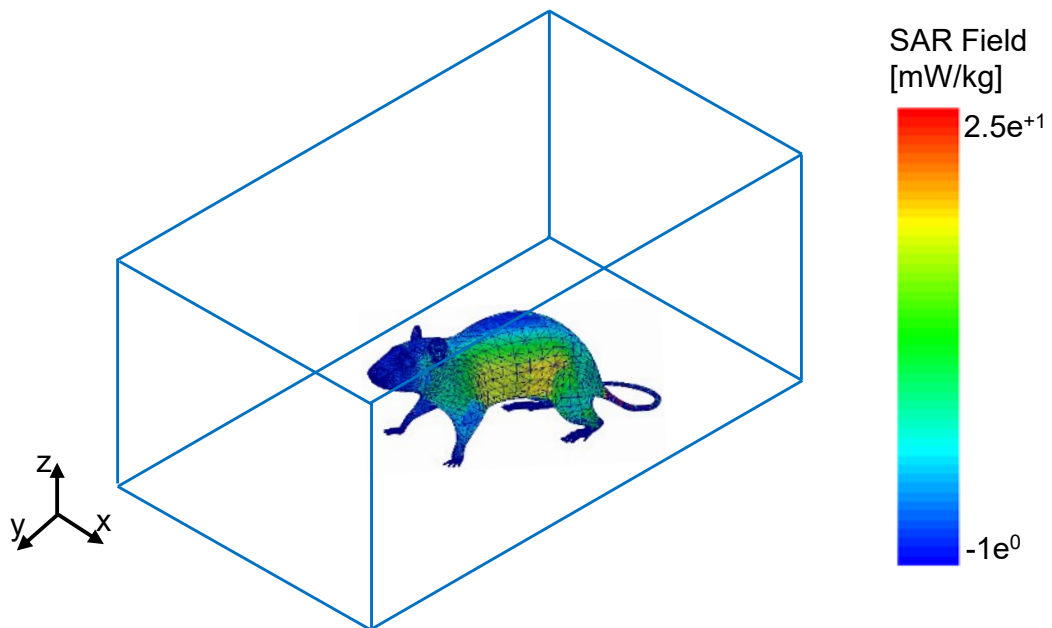
and 20 Hz with 5 ms light pulse; 5 % and 10 % duty cycles). Consistent with this, calculation of specific absorption rate using a finite-element method analysis tool showed that the specific absorption rate (SAR) distribution against localized RF exposure is below IEEE guidelines[62] (Figure 2-9). Finally, tests in mice showed that the pre-curved, sandwiched tether was functional for over a month, while the post-curved structure stopped working three days after implantation (Figure 2-10).



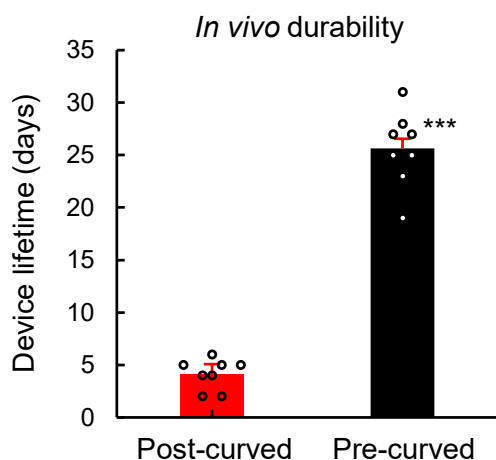
**Figure 2-7.** Durability test at various temperatures *in vitro*; measurements of optical output power from devices when immersed in 10 % PBS at various temperatures, 25 °C, 60 °C, and 90 °C.



**Figure 2-8.** Thermal assessment of the proposed device. A device mounted on a sealed bag of 10 % PBS solution, immersed in saline solution, and itself in a cage, respectively. Plots of optical intensity as a function of time at duty cycle (a; 5 %) and (b; 10 %) in three different conditions; wet, dry, and PBS bag.



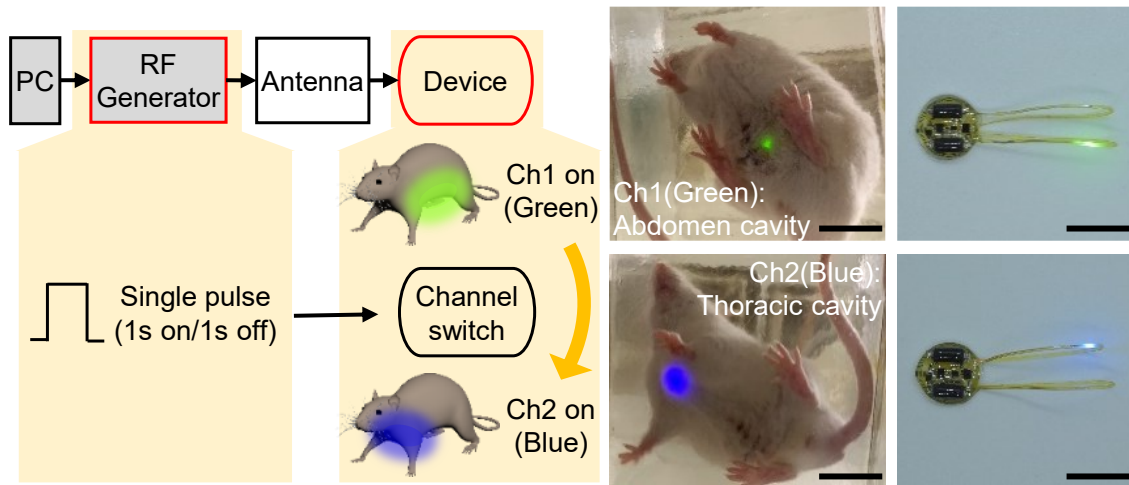
**Figure 2-9.** An experimental assay with computed SAR distributions on a mouse mesh body.



**Figure 2-10.** Measurement of device lifetime for pre- and post-curved structure when implanted (pre-curved,  $n = 8$ ; post-curved,  $n = 8$ ). Bar graphs are mean  $\pm$ SEM. Statistical comparison was made using a two-tailed  $t$ -test; \*\*\* $p < 0.001$ .

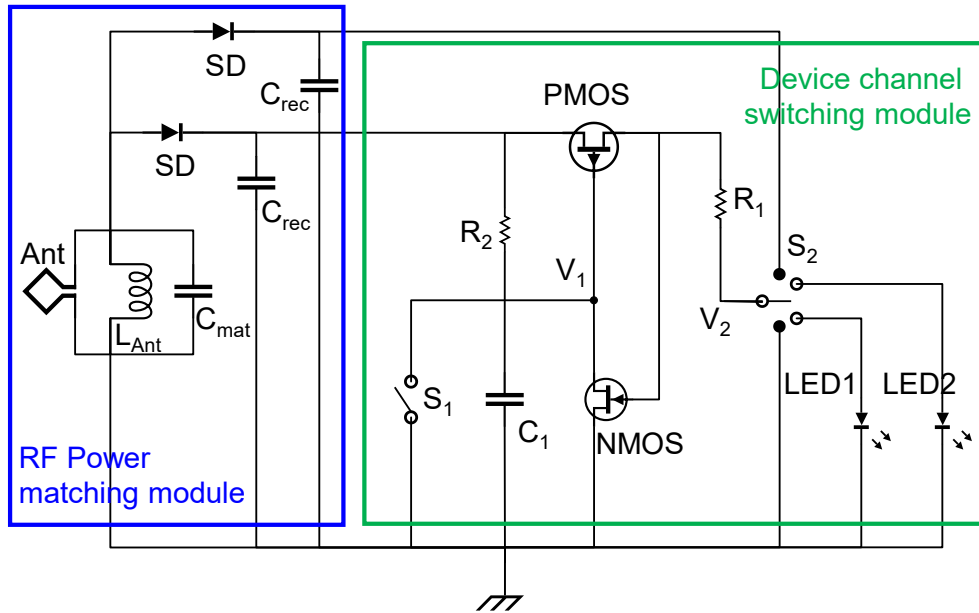
### 2.3.2. Characteristics of Dual-channel Gastric Optogenetic Implants

Multimodal device operation is another strategy for increasing the efficiency and throughput of wireless-optogenetic studies. Targeting multiple organs with a single device could enable multi-organ analysis in the same animal or even be used to examine organ-to-organ interactions. Realization of multimodal tools requires an actuation mechanism that can remotely manage channel selection. Previous efforts utilized higher operating frequencies,  $\mu$ C chip or Bluetooth kits for actuating separate channels, but these approaches require increased RF power (tens of mW) for operation and render them energy-hungry devices[55], [66]. Here, we use a reed switch in the device that responds to the pattern of externally applied electromagnetic RF pulses. In our example, a pulse width longer than 100 ms triggers the transition from a green  $\mu$ LED to a blue

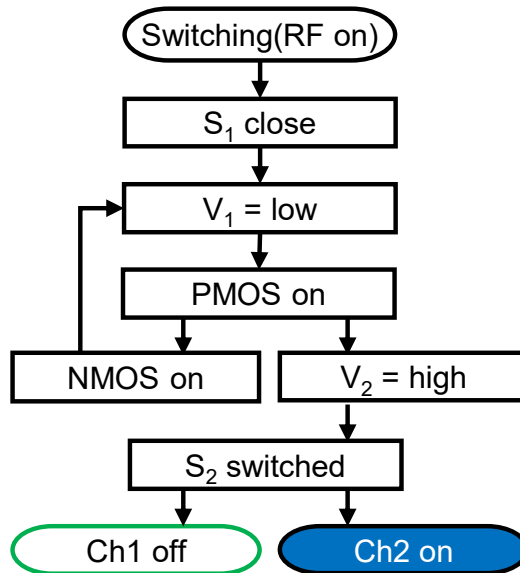


**Figure 2-11.** Illustration of wireless operation of a scalable, multimodal wireless gastric optogenetic implant (left), photos of an animal with the device implanted (middle), and photos of the device (right); scale bar 1 cm.

$\mu$ LED located on a separate tether (Figure 2-11). The actuation threshold can be adjusted by pairing different capacitors and resistors with the reed switch to prevent unwanted activation or deactivation, and could theoretically be tuned for switching between more than two channels[67], [68]; the circuit diagram and flowchart are shown in Figure 2-12 and Figure 2-13. Importantly, this strategy only requires 10  $\mu$ W for channel selection, which is 100-fold less power than other approaches[55], [66], [69]. When combined with the dual-coil antenna and multiplex coupling/decoupling, the proposed optoelectronic system enables robust, ultra-efficient wireless powering of optogenetic devices in multiple organs and multiple cages with independent and simultaneous control. Time slots allocated for each cage and threshold pulse for channel selection are tunable, suggesting many scenarios of multiplexing and multimodal operation. For example, we



**Figure 2-12.** Dual-channel device circuit diagram:  $C_{mat} = 412$  pF,  $C_{rec} = 0.1$   $\mu$ F,  $R_1 = 5$  k $\Omega$ ,  $R_2 = 20$  k $\Omega$ ,  $C_1 = 100$  pF, LED1 is green, LED2 is blue.

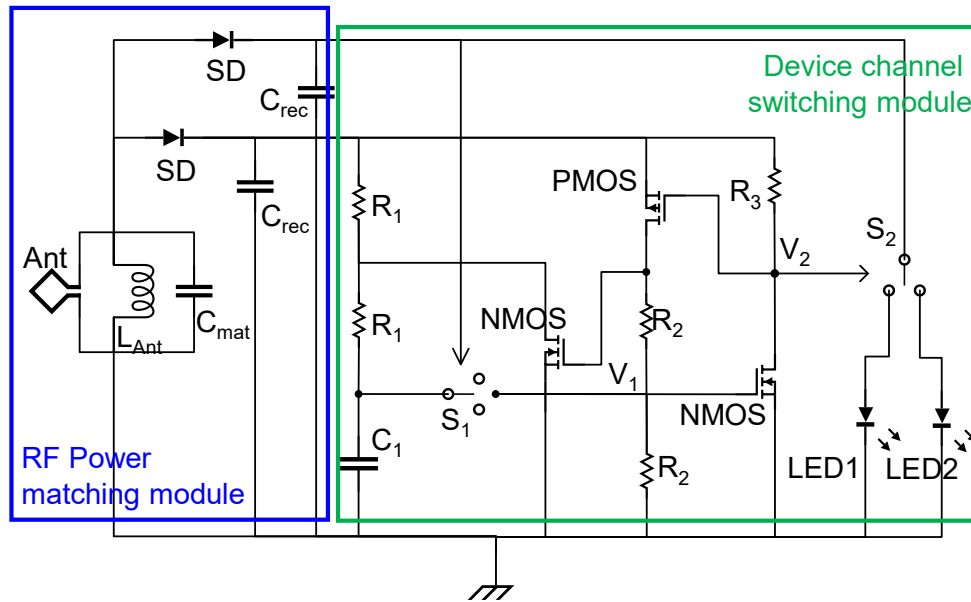


**Figure 2-13.** Flowchart of switching mechanism by a reed switch on the dual-channel device.

set threshold pulse for activation/deactivation of channels to 100 ms and allocate 250 ms for each cage. This provides enough time for an implant in each cage to switch its channel (from channel 1 to channel 2 or vice versa). It requires only two seconds ( $8 \times 0.25$  sec) for the switching operation of implants in cages. Next, the TX system can adjust time slots, depending on stimulation conditions.

However, the method mentioned above also has fatal flaws: an actuation mechanism enabled by a reed switch offers a one-time switching operation, and reverse operation (channel switch from channel 2 to channel 1) is not allowed due to the nature of memoryless logic circuits. This one-time switching operation can be accomplished by the employment of a sequential toggle logic circuit that accommodates both previous and current input states. Such event-driven sequential toggle logic is an asynchronous circuit that changes state immediately when enabled. Due to its form factor (8 mm by 1.7 mm), the platform cannot be extended to offer more channels ( $>3$ ) in the current compact design (1 cm in diameter).

To break these defects, I suggest another mechanism that enables selective activation of the channel while still having low-power consumption. It is based on a memory logic circuit that can store the previous state even the device lost power for a while, enabling reverse operation for switching between two channels. It utilizes an analog switch which is much smaller (1.6mm by 1.2 mm) than a reed switch. The circuit diagram appears in Figure 2-14.



**Figure 2-14.** Dual-channel device circuit diagram based on memory logic:  $C_{mat} = 412 \text{ pF}$ ,  $C_{rec} = 0.1 \text{ }\mu\text{F}$ ,  $R_1 = 249 \text{ k}\Omega$ ,  $R_2 = 10 \text{ k}\Omega$ ,  $R_3 = 5 \text{ k}\Omega$ ,  $C_1 = 1 \text{ }\mu\text{F}$ , LED1 is green, LED2 is blue, and  $S_1 = S_2 = 1 \times 2$  analog switch.

## 2.4. Discussions

### 2.4.1. Necessities for Increasing Device Life Span

Insufficient understandings of device failure mechanisms, or gaps between knowledge and reality regarding the impact of biological strain on a device, add substantial barriers to the development of a robust, biocompatible, implantable wireless device for chronic studies. For example, an animal's natural motion near a device's implanted region can induce the deformation of metal traces. In the long-term, such strains can also accelerate malfunction and the degradation of the quality of encapsulation material, leading to fatigue failure[70]. The implanted devices we proposed maintained functionality over one month (Figure 2-10) and the implantation

did not cause any inflammation or lesions to the stomach and abdominal cavity. The proposed strategy of securing a tether to the stomach was successful, suggesting expanded opportunities for the use of the technology in neuroscience. Despite this progress, the limited durability of implants makes it impossible to perform longitudinal studies that require long-term monitoring of behavior (e.g., obesity experiments that involve a high-fat diet) or extensive animal training (>4 months). To realize the full potential of optogenetics to study the PNS, it is essential to improve the durability of these devices so that they become as robust as the currently widely used fiber optics in the brain.

#### **2.4.2. Extension to Multichannel Gastric Optogenetic Implants**

When combined with memory logic, a sequential toggle logic circuit can make a transition from channel 1 to channel 2 or vice versa with chronic stability in operation. This approach can be extended to offer up to eight channels in a single platform device. In this method, the status of  $V_2$  is paramount (Figure 2-14). The switching time is determined by  $C_1$  and  $R_2$ , which can control  $V_2$ . In other words, we can define the switching time to change  $V_2$  by adjusting the  $C_1$  and  $R_1$  values. Here, each switching module can be connected in parallel, leading to a miniaturized, multichannel switching circuit. Such tools allow for the stimulation of sub-cell types innervating in an organ(s) simultaneously or independently. For example, meal termination is processed by two pathways that interact with peripheral nerves passing from the gut to the hindbrain or circulate to the hindbrain via the blood. However, little is known about the roles of vagal



or spinal sensory pathways and their dynamic interplay in feeding control due to the absence of technology that can stimulate only peripheral nerve endings in freely behaving animals. Therefore, by applying the proposed multichannel, organ-specific optoelectronics, we can test the hypothesis that exposure to a high-fat diet induces functional resistance to activate spinal cell types or the vagus nerve from distinct organs, thereby preventing normal meal regulation and promoting obesity.

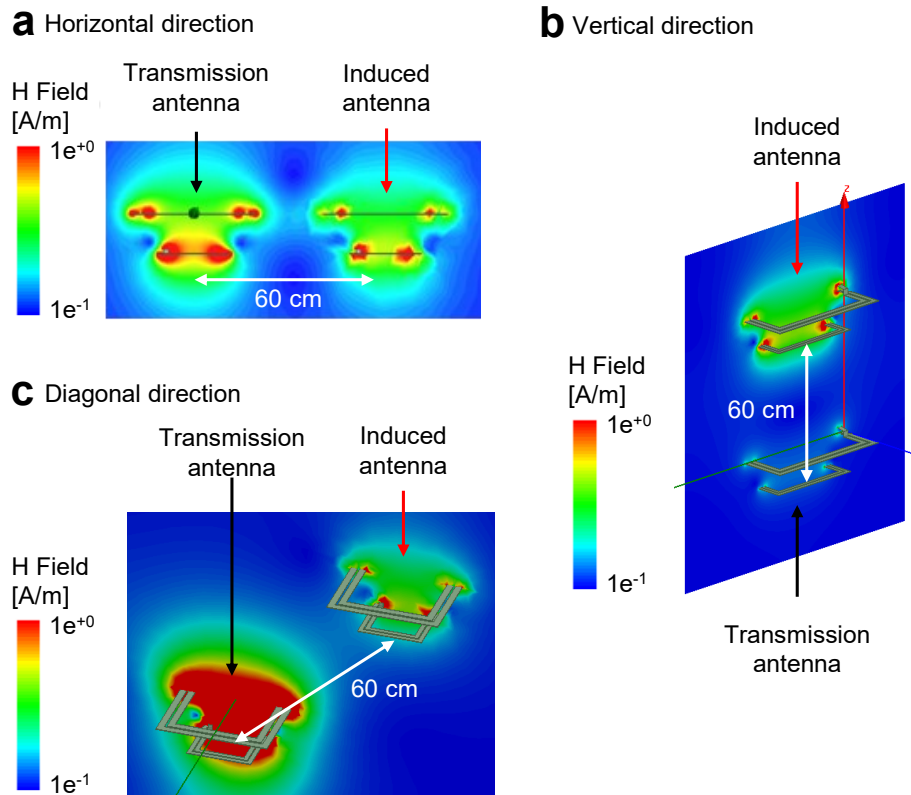
### 3. LOW-POWER, MULTICHANNEL WIRELESS TELEMETRY\*

#### 3.1. Introduction

As mentioned in the previous chapter, advances in wireless platforms have been able to bypass the limitations of preexisting fiber-optic interfaces and external connections[42], [43], [47]. Additionally, even the recently developed wireless power transfer systems have drawbacks: the biggest challenge of which is power transfer efficiency. Early wireless power transfer technology used the UHF (300-3,000 MHz) band, which causes the following barriers within or adjacent to the area of interest: signal reflection, absorption, and interference by other obstacles, including metal objects and skin tissues. In particular, this characteristic of wireless operation diminishes the efficiency of power transfer, hampering the available power of the device, which results in constraints in the size of the implants and feasible area of the experimental cage according to the TX antenna design[48], [49]. Accordingly, the most advanced research uses the HF (3-30 MHz) band, commonly at a frequency of 13.56 MHz, which is not sensitive to the presence of objects or physical obstacles and provides complete wireless coverage in various cage types and environments[71]–[74]. However, the wireless power delivery is still deficient due to the antenna structure, and the deficiency becomes more pronounced as the power requirements of implantable devices increase[75].

---

\*Reprinted with permission from “Organ-specific, multimodal, wireless optoelectronics for high-throughput phenotyping of peripheral neural pathways” by Kim, W.S.; Hong, S.; Gamero, M.; Jeevakumar, V.; Smithhart, C.M.; Price, T.J.; Palmiter, R.D.; Campos, C.; Park, S.I, 2021, *Nat Commun*, 12, 157, © 2021 by Springer Nature.



**Figure 3-1.** Simulation results of electromagnetic couplings induced in an adjacent cage as a function of the distance between two cages along the horizontal (a), vertical (b), and diagonal (c) axes, respectively at a transmitted power level of 4 W.

Another issue with optogenetic research is the strategy for experimental efficiency. Practical use of optogenetics depends on reliable and cost-effective light delivery in multiple animal subjects. A complete laser-based, optogenetics setup remains cost-prohibitive for many labs, given that each animal subject requires a laser, fiber-optic cannula, fiber-optic patch cord, and rotary joint to decrease the physical constraints of the patch cord[31]. Wireless optogenetics is similarly limited, typically requiring a single RF power generator for each home cage[42]. A researcher may use multiple RF

power generators, but they must be operated at least 1 m apart from each other to avoid electromagnetic interference[76] (Figure 3-1). Together, these constraints limit the group sizes used for studies, restrict the duration and type of behavioral experiments that can be conducted, and hinder the high-throughput utilization of optogenetics in limited space overall.

Also, in order to deliver lights to multiple animal subjects, we can design an experiment with multiple animals in one experimental space. However, since wireless power transfer systems have coverage issues according to the antenna structure and spatial area, the experiments using a large-scale cage have been difficult to achieve using wirelessly-powered platforms. Alternatively, a system has multiple antennas installed, and that selects optimized antennas depending on the position or pose of the animals increases power transfer efficiency. To apply this system, we introduce a technique that automatically regulates the TX system based on recently evolving computer vision algorithms. This ML-enabled adaptive TX system concept has become possible due to the development of image processing algorithms. In particular, progressive advances in deep neural networks for image and video analysis have enabled automated tracking of live animals and computer-based quantitative analysis of their behavior[77]. Monitoring and analyzing the differential response of animals to different stimuli under various experimental conditions are commonplace in many neuroscience studies, and human experts in the past analyzed video records of the animals manually[78]. Not only are these tasks labor-intensive and time-consuming, but the quality of the analysis results depends on the proficiency of the human expert. Due to the nature of the non-automated

process, we exclude adopting an efficient strategy for adaptive control of neural modulation devices, which requires real-time analysis. Fortunately, in recent years, deep convolutional neural networks (DCNNs) have been highly valuable for various image and video analysis tasks, including semantic segmentation, object recognition, and object tracking, often outperforming human experts[79], [80].

Alongside recent advances in deep learning, various tools have been developed that can facilitate and automate the quantitative behavioral analysis of live animals from videography[81]. For example, Mask R-CNN provides a powerful tool for object instance segmentation by utilizing and enhancing region-based CNN (R-CNN)[82]. Mask R-CNN can simultaneously detect multiple objects in a given image and yield accurate segmentation results for each instance. This framework can be extended to other tasks, such as human pose estimation, in a relatively straightforward manner. Another tool called DeepLab utilizes DCNNs and fully-connected conditional random fields (CRFs) for semantic image segmentation[83]. DeepLab has been extensively evaluated on various datasets and shown to excel in various challenging segmentation tasks, such as body parts[84]. Another example is DeepLabCut (DLC), a novel algorithm designed for automatic pose-estimation of body parts through video analysis based on deep neural networks[85]. By eliminating the need for explicit markers, DLC can effectively detect user-defined body parts of humans or animals in video recordings and accurately estimate their poses. This approach allows real-time quantitative behavioral analysis in animal-based neuroscience studies, paving the way toward efficient adaptive control of implanted devices to manipulate neural activities.

In this chapter, I introduce a low-power, multichannel wireless telemetry and dual-coil structure antenna that can resolve current flaws, such as cost-effectiveness and electromagnetic interference. First, this chapter describes a multichannel wireless power strategy that overcomes spatiotemporal limitations by avoiding the electromagnetic field interference dilemmas by combining the decoupling and RF switch mechanism with a time division strategy. After that, a proposed dual-layer structure antenna implies significant improvement to the efficiency of wireless power TX/RX in the experimental cage. Lastly, I introduce an ML-based adaptive TX system that, in combination with real-time image processing algorithms, can handle the experiment with multiple (here, five) mice in a large assay, such as an open-field box at the same time.

## **3.2. Methods**




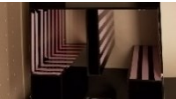


### **3.2.1. Fabrication of Dual-coil Antenna and Power Control System**

We used 8-ga bare Cu wire for the bottom antenna coil and Cu stripes (0.635 mm thick by 2.54 cm wide) for the top antenna coil. The bottom coil was placed under a cage while the top coil was situated 8 cm above the cage bottom. Impedance matching using Network Analyzer (ENA Series E5063A, Keysight) with discrete capacitor components yielded two antenna coils, each of which resonates at 13.56 MHz (the top coil) and 15 MHz (the bottom coil), respectively; these different frequencies offer broad bandwidth and stable coverage. Wireless power control systems consisted of an RF power supply (ID ISC.LRM2500-A, FEIG Electronics), matching board (ID ISC.DAT-A, FEIG Electronics), RF multiplexer (ID ISC.ANT.MUX.M8, FEIG Electronics), controller

(nRF52832 Development Kit, Nordic semiconductor), and decoupling multiplexer.

Dimensions of a representable coil antenna, capacitance, and inductance for different sizes of experimental assays, including home cages are found in Table 3-1.

**Table 3-1.** Summary of customized TX antenna specification

Cage image	Cage dimension*	Distance of top & bottom coils	Antenna dimension*		Inductance of Antenna		Required capacitance	
			Top**	Bottom***	Top**	Bottom***	Top**	Bottom***
1 	20×30×13	8 cm	19×29	16×25	660 nH	670 nH	120 pF	167 pF
2 	20×38×16	12 cm	20×37	16×29	780 nH	780 nH	102 pF	147 pF
3 	34×39×21	6 cm	34×36	29×29	940 nH	1.00 μH	85 pF	110 pF
4 	Inner box 18×18×30 Outer box 41×41×30	14 cm	18×18	16×16	485 nH	580 nH	164 pF	189 pF
5 	40×40×30	3 cm	41×41	37×37	1.04μH	1.42 μH	74 pF	79 pF
6 	28×28×30	5 cm	30×30	26×26	760 nH	1.23 μH	100 pF	92 pF

**All values are ±5% tolerance.**

\* dimension: (width) × (length) × (height) or (width) × (length); unit: cm

\*\*Top coil material: Cu stripes (2.54 cm wide; 0.635 mm thick)

\*\*\*Bottom coil material: 8-Gauge bare Cu wire

### **3.2.2. Finite Element-Method Analysis**

For numerical electromagnetic simulations of the proposed device and TX system, we used a finite element analysis tool, Ansys Electromagnetics Suite 17-HFSS, to look for the strength and uniformity of electromagnetic field in the mouse's home cage (dimensions: 16 (w)  $\times$  25 (l)  $\times$  13 (h) cm). Organ systems and tissues of a mouse were modeled to one million meshes for numerical simulations, and antenna coil made of Cu stripes were modeled to materials with finite conductivity,  $58 \text{ MS s}^{-1}$ . Most existing wireless powered optoelectronic devices have power delivery issues of angle and position dependency in a large area that allows experiments with freely moving animals. To prove that we have overcome this matter in our proposed system, we elicited simulation results in various positions and angles of the proposed device in the home cage with a dual-coil TX system. All simulations were conducted with 4 W, TX power level due to considering the safety level of electromagnetic fields[62].

### **3.2.3. Characterization of Wireless Telemetry**

We implanted a wireless device over the skull, under the skin of a mouse, and recorded their behaviors using three cameras (C615, Logitech). A red-colored  $\mu\text{LED}$  was embedded in an implanted device to serve as a signal that can be easily detected by cameras over a cage, and the wireless TX system transmitted RF signals at 1 W. One camera was positioned above a cage, and two cameras recorded from the left and right sides. They recorded behaviors of an animal in a cage for 2 min, and we extracted images from the recordings and analyzed them frame by frame to determine whether an



image had captured the wireless operation of a device (red  $\mu$ LED). Next, we counted the number of frames missing wireless operation. For a visual demonstration of wireless coverage, we reconstructed 3D continuous traces of a red  $\mu$ LED from extracted images: this analysis code for 3D reconstruction image is available from Zenodo[86]. We repeated the procedures described above for other wireless antenna technologies and obtained antenna performance comparison results.

For other validations of wireless power TX systems, we used an electromagnetic probe (TBPS01-TBWA2/40dB, Tekbox) to measure the output power at five representative positions (A, B, C, D, and E) and various heights from the bottom of the enclosure as a function of the distance and angle.

#### **3.2.4. Modification to DeepLabCut (DLC) Model**

We utilized, custom-trained, and modified the DLC python package (Ver. 2.2b7). Specifically, we used the custom-trained DLC model to estimate the locations of the body parts such as snouts and tails of the mice within an image. Note that the original DLC python package does not support a real-time processing feature, instead it only runs on video files. Hence, we directly modified the Python package in such a way that it can infer the locations of the body parts of the mice and estimate the optimal coil antenna through the functional modules in a real-time manner. We conducted all experiments including training the DLC on a GPU workstation (Lambda workstation with Intel Core i9-9960X, 128 GB RAM, and two GEFORCE RTX 2080 Ti graphics cards).

### **3.2.5. Quantitative Performance Assessment of the ML-Enabled Motion Tracking Algorithm**

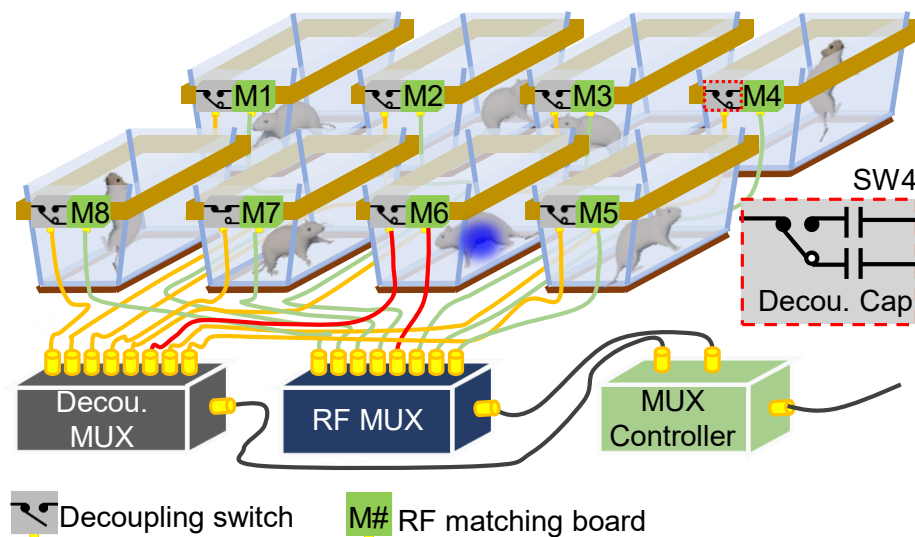
The proposed ML algorithm yields the following information for each frame: 1) the position of the snout and tail of each mouse, 2) the direction in which each mouse is heading toward, and 3) the angle between a vector along the length of each mouse and the y-axis. Based on this information, the algorithm selects an antenna coil that leads to the best wireless coverage in a cage. The following are three antenna settings in this study: 1) Two pairs of X-shaped coil antenna, X-shaped coil antenna in 2) the x-axis direction and 3) the y-axis direction. For the quantitative performance assessment of the algorithm, we used three video recordings, each of which is 10 minutes running time. We randomly extracted and evaluated 20 frames from a total of the 15,000 frames in each recording, and repeated the procedures twenty times for reliable evaluation. For each of 20 frames, we compared the decision made by the ML algorithm for each frame in the given set with the one made by a human expert in each antenna setup. To check the performance of each antenna setup and implanted devices, we focused on two statistics (in terms of the number of frames): 1) how long a selected antenna remains activated and 2) how many frames (i.e., how long of a time interval) it takes between activation of an antenna and its reactivation after the first deactivation. Here, a human expert extracted and analyzed the data, which had been processed by the ML algorithm, in every 20 frames. For case 1), we chose a mouse (implanted device) from the group and measured how long a selected antenna remains activated or aligned with a vector determined by the mouse as a function of frames. Similarly, for case 2), we measured a

time interval as a function of the number of frames between deactivation of an antenna and subsequent reactivation of it. These were averaged out after 20 trials, leading to statistics in Results 3.3.3.

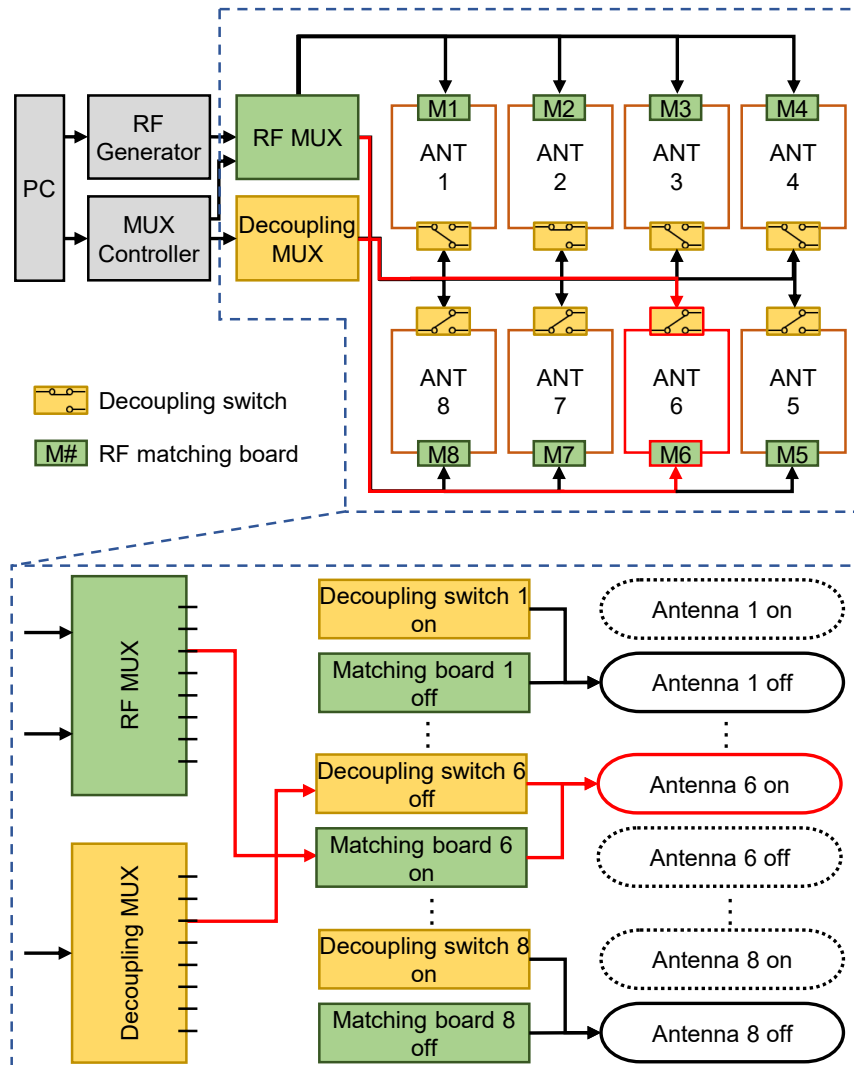
### 3.3. Results

#### 3.3.1. Time Division Multiplexing

We developed a multiplex approach to power 8 individual cages with a single RF-power generator. The wireless telemetry system consists of an RF-power generator, controller, an RF multiplexer, a decoupling multiplexer, and antenna sets for each of the 8 cages (Figure 3-2); each antenna set is made of a pair of top and bottom coil structure (Detailed in section 3.3.2). Simultaneous and independent control of the 8 cages is

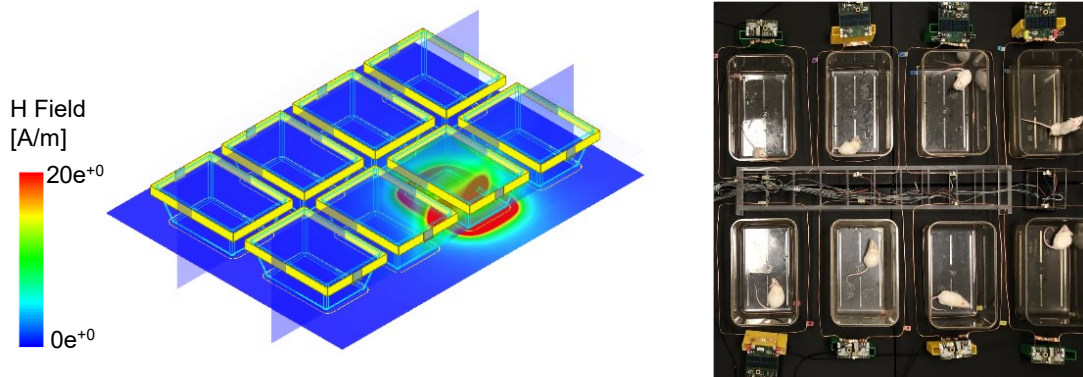


**Figure 3-2.** Schematic illustration of the multiple cage wireless power TX system for high-throughput phenotyping of neural pathways.



**Figure 3-3.** Functional block diagram of the proposed wireless power TX system.

achieved with coupling and decoupling circuits that manage the tuning of antennas to operational (13.56 MHz) and non-operational (100 MHz) device powering frequencies. For example, when the controller selects antenna set 6, the RF multiplexer tunes antenna set 6 to 13.56 MHz and Decoupling multiplexer detunes the other antenna sets to 100



**Figure 3-4.** Electromagnetic simulation of wireless coverage for the proposed system (left) and a photo of the system (right).

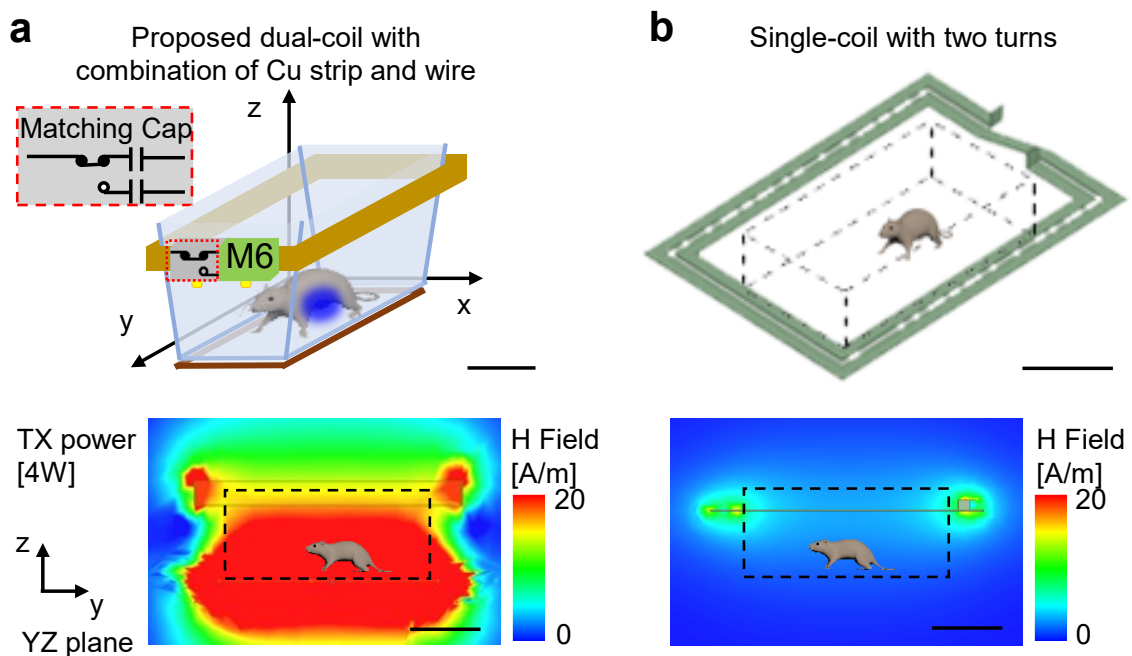
MHz (Figure 3-3). The other antennas that are detuned and deactivated can only pass a negligible amount of energy at a frequency of 100 MHz, which significantly deviates from the resonant frequency of 13.56 MHz. Therefore, the other 7 antenna sets do not cause interference even when directly adjacent to the actuating 13.56 MHz antenna; this was confirmed with electromagnetic simulation results and validation experiments *in vivo* (Figure 3-4). Since optogenetics typically requires brief intermittent light pulses to avoid depolarization block[31], this strategy can be used to toggle between multiple cages to deliver intermittent light pulses. Therefore, the limiting factors for the number of cages that can be operated simultaneously with a single RF-power generator are the stimulation frequency and duration of light pulses. With the proposed arrangement (Figure 3-2 and Figure 3-3), we conducted experiments within 8 cages simultaneously using 20 Hz and 5 ms pulse duration stimulation parameters. This extends the high-throughput utilizing optogenetics to do the experiments at least 8 mice (supposed a

mouse in a cage), a typical group size, at that same time. For example, measurements of food intake require 4 hours for each animal in the group. To complete analysis of feeding behavior for two groups of animals (experimental and control), each of which has 8 animals, it only takes 8 hours while approaches using existing wireless TX system, a single power source coupled with a single cage, demands 64 hours ( $8 \times 8$  hours). This makes it less ideal for longitudinal experiments, in particular those required for most obesity experimental designs, where a device needs to be chronically implanted for >2 months. Also, through the modification of the multiplexer board and controller, simultaneous activation of 16 cages at 10 Hz or 32 cages at 5 Hz frequency is possible when using a 5 ms light pulse duration.

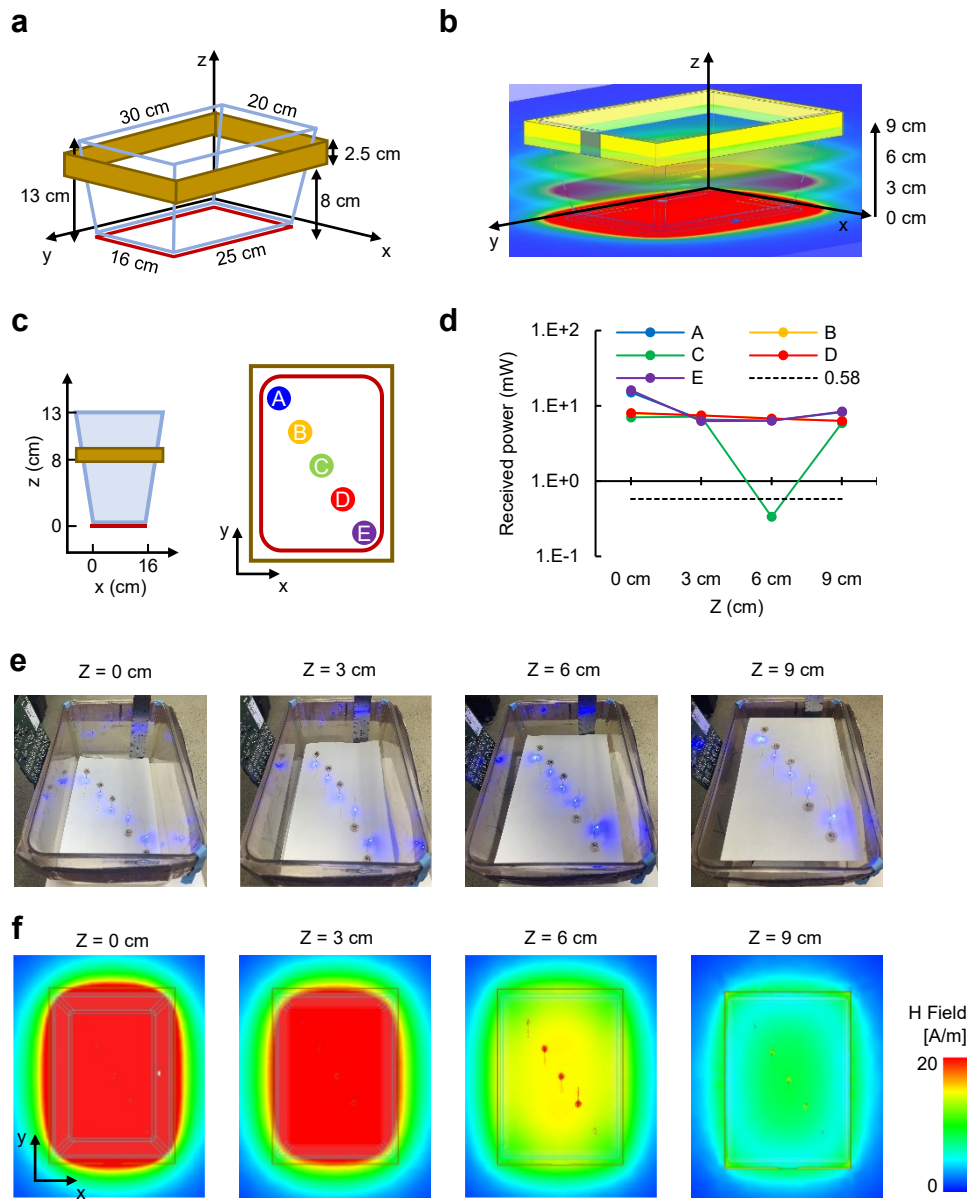
### **3.3.2. Dual-coil Antenna System**

In addition to couplings, wireless coverage remains a significant limitation for optogenetic experiments. Conventional systems utilize a single RF antenna below or around the sides of a home cage[42], [49]. Due to electromagnetic dissipation away from the RF source, wireless coverage can be as low as 30 % in a home cage[75] and worse in larger behavior boxes. Previously, these limitations were circumvented by increasing RF power, but this results in undesired RF energy to animal tissues and increased heat generation. Here, we introduce a simple dual-coil antenna system for increasing wireless coverage[87]. It consists of a top antenna coil that is connected to an RF generator and an unconnected antenna coil below the cage that passively attracts RF signals towards the animal subject and cage bottom. 3D electromagnetic modeling suggested that the

dual-coil antenna system could enable continuous operation throughout a location of interest (Figure 3-5). This was confirmed with light-power-output measurements and simulation results of wireless devices at five representative positions and heights from the cage bottom, which demonstrated robust device activation throughout the volume of a cage (Figure 3-6). Furthermore, the dual-coil antenna system minimized the dependence of transmitted power on the relative orientation angle between the TX antenna and RX antenna in the implant device (Figure 3-7). Comparison studies further indicated that the proposed antenna system outperforms other existing systems, offering virtually complete wireless coverage in a home cage (Figure 3-8).

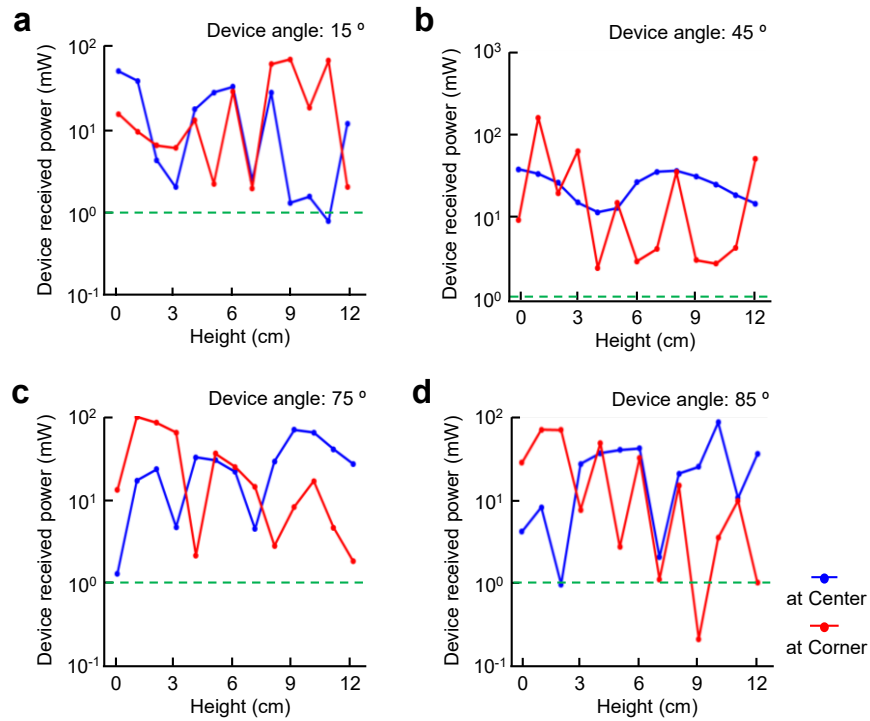


**Figure 3-5.** Illustration of an antenna layout (top) and distribution of electromagnetic simulation of wireless coverage in a cage (bottom) for the proposed system (a) and single-coil antenna structure (b), respectively; scale bar 10 cm.

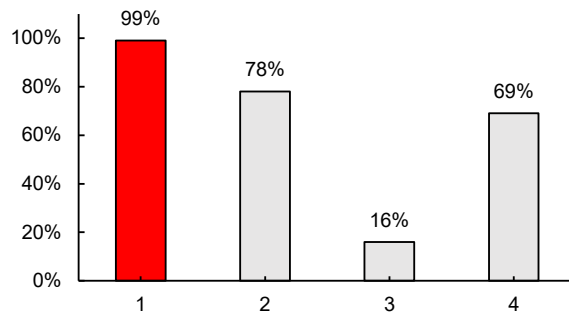


**Figure 3-6.** (a) Representative image of a cage with the proposed antenna coils installed. (b) Distributions of the electromagnetic field in a cage at each distance from the bottom. (c) Illustration of the measurement setup. (d) Measurements of output power at 5 different locations of the cage as a function of the distance along the z-axis. Dotted lines indicate the threshold electrical power (0.58 mW) required for the activation of light-sensitive opsins; 0.58 mW electrical power corresponds to an optical power of 10.12 mW mm<sup>-2</sup>. (e) Representative images of wireless operation in the cage at each distance. (f) Corresponding distributions of the electromagnetic field in the cage at each distance from the bottom.



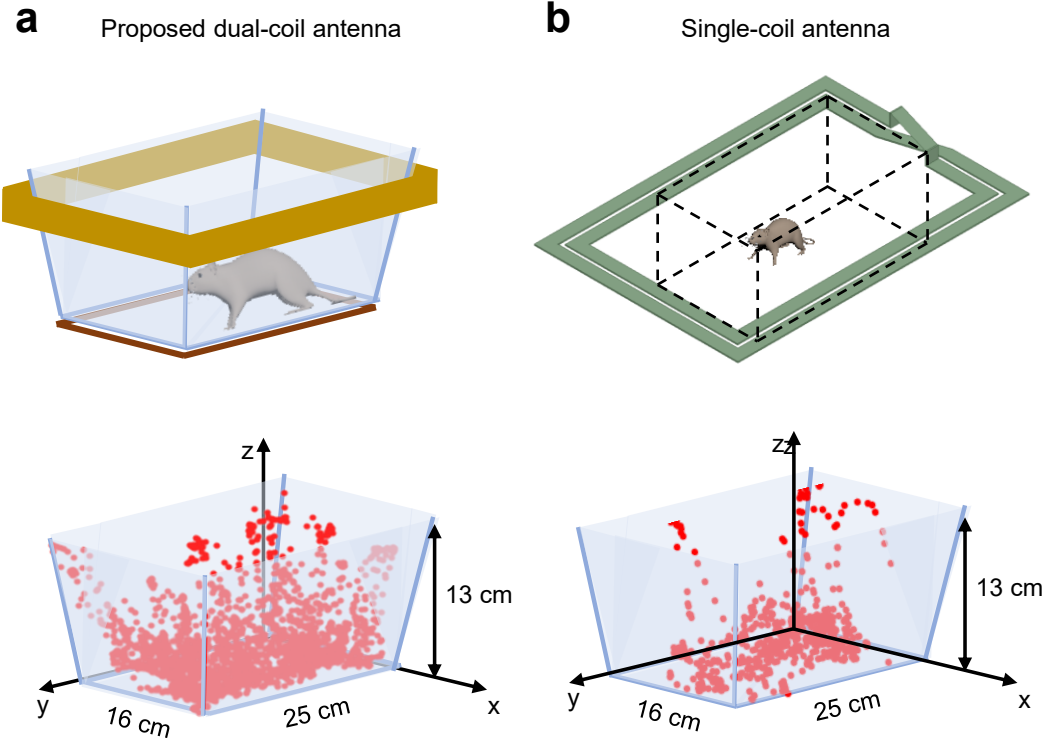


**Figure 3-7.** Plots of a residual dependence of transmitted power on relative orientation angle between the TX antenna and the implantable device as a function of the angle, 15 ° (a), 45 ° (b), 75 ° (c), and 85 ° (d). Green dotted lines indicate 70 % higher (1 mW) than threshold electrical power level (0.58 mW) required for activation of light-sensitive proteins; 1 mW electrical power corresponding to an optical power of 17.44 mW mm<sup>-2</sup>.



**Figure 3-8.** Comparisons of wireless coverage; 1. Proposed dual-coil antenna, 2. Single-coil & dual-layered antenna[75], 3. a tilted antenna design with a time division multiplexing schematic[66], and 4. Single-coil & single-layered antenna at the TX power level of 1 W.

To validate the performance advantages of the proposed dual-coil antenna TX system, we carried out *in vivo* experiments. A wireless optoelectronic device is implanted on the skull of a mouse, and light emitted from the wireless device through the skin serves as an explicit marker to determine wireless coverage. Three webcams above and sideward the cage capture motions of an animal in real-time with a focus on detecting light emitted from the implanted device. Then, images are extracted frame by frame from recordings, and only images indicating wireless operation are selected. Finally, the computation of the number of missing frames among total frames yields a



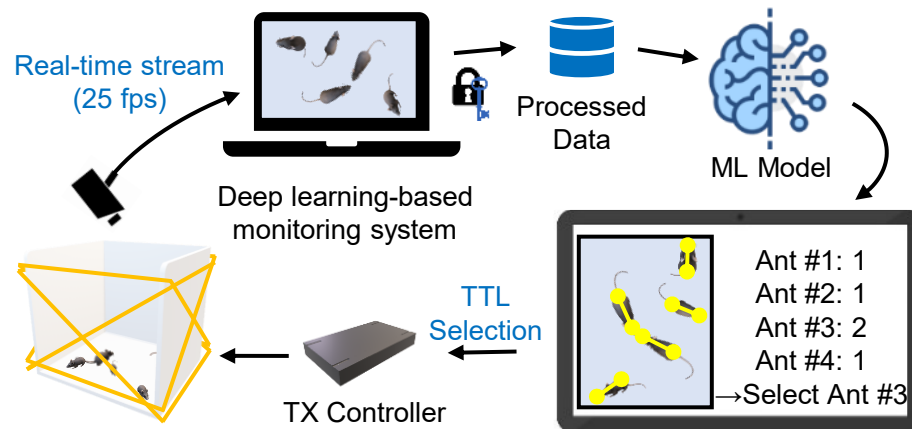
**Figure 3-9.** Illustration of antenna layouts (top) and 3D reconstructions of traces of an operating indicator LED (bottom): proposed dual-coil antenna (a), and single-coil antenna structure (b), respectively.

good indicator of wireless coverage. For a visual demonstration of wireless coverage, we reconstructed 3D continuous traces of the red LED from the recorded video. We repeated the procedures described above for wireless coverage comparison of the proposed method with other existing wireless antenna technologies[66], [75]. Comparison studies further indicated that the proposed antenna system outperforms other existing systems, offering visually complete wireless coverage in a home cage (Figure 3-9). In comparison with the existing time division multiplexing scheme or single-coil antenna systems, the proposed dual-coil or adaptive wireless TX system shows a 5× increase in coverage at a TX power level of 1W (Figure 3-8). Existing antenna systems could enable similar levels of function at higher levels of TX power (i.e., above 10 W) in the context of wireless coverage. However, a corresponding increase in TX power to compensate for their low efficiency could potentially result in exceeding the maximum exposure limits[88].

### **3.3.3. Machine Learning-Enabled Real-Time Motion Tracking of Multiple Animals**

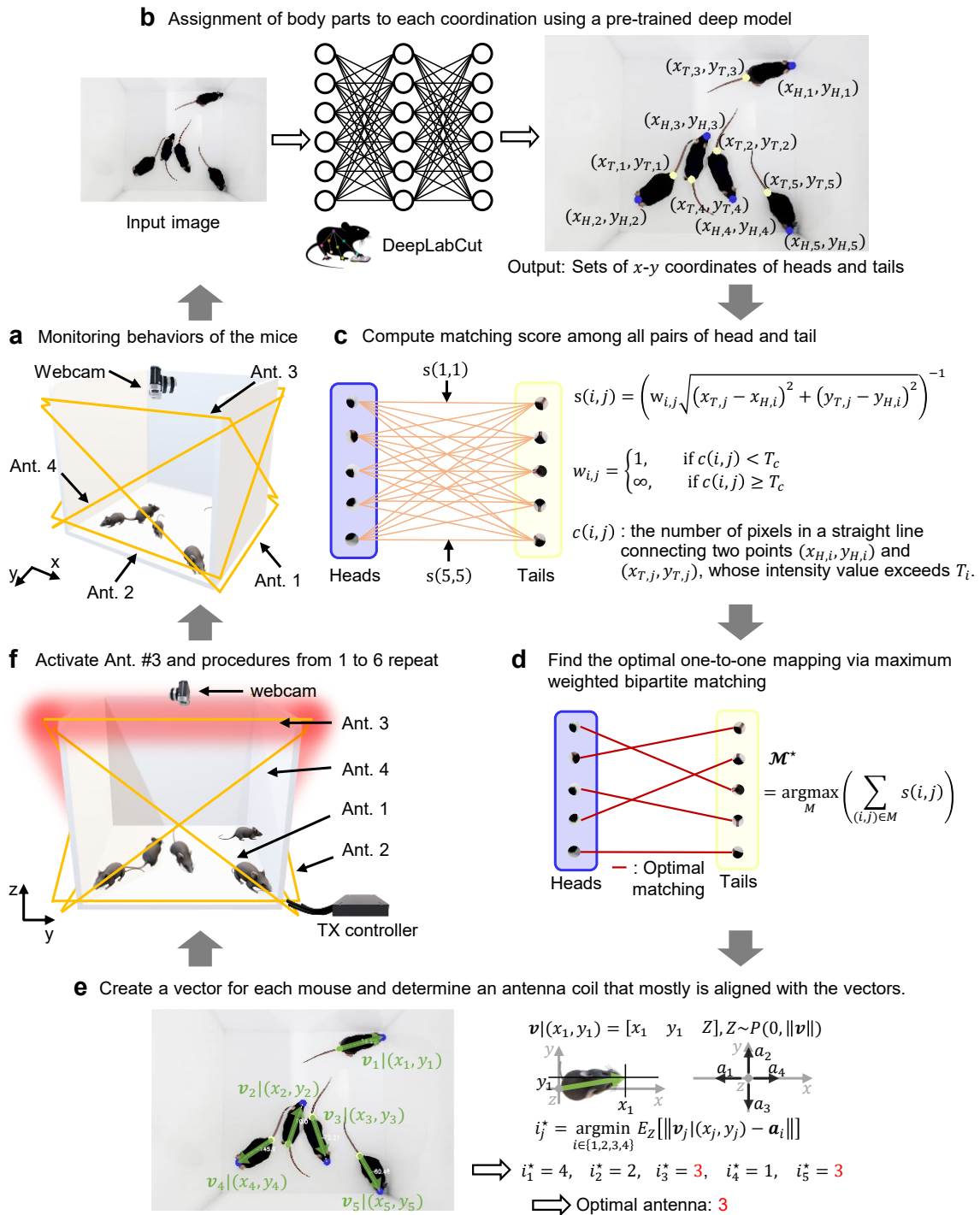
Overview of the proposed ML-driven adaptive wireless power TX system is shown in Figure 3-10. Here, an advanced ML algorithm allows for real-time motion tracking of mice (<5) in an open-field box through automated video analysis. This enables the optimal control of prearranged coil-antennas to offer uniform wireless coverage and thereby the robust activations of implanted devices in each animal.

Figure 3-11 illustrates step-by-step procedures for ML-enabled real-time motion tracking of mice in a cage where five mice with a device implanted freely behave and

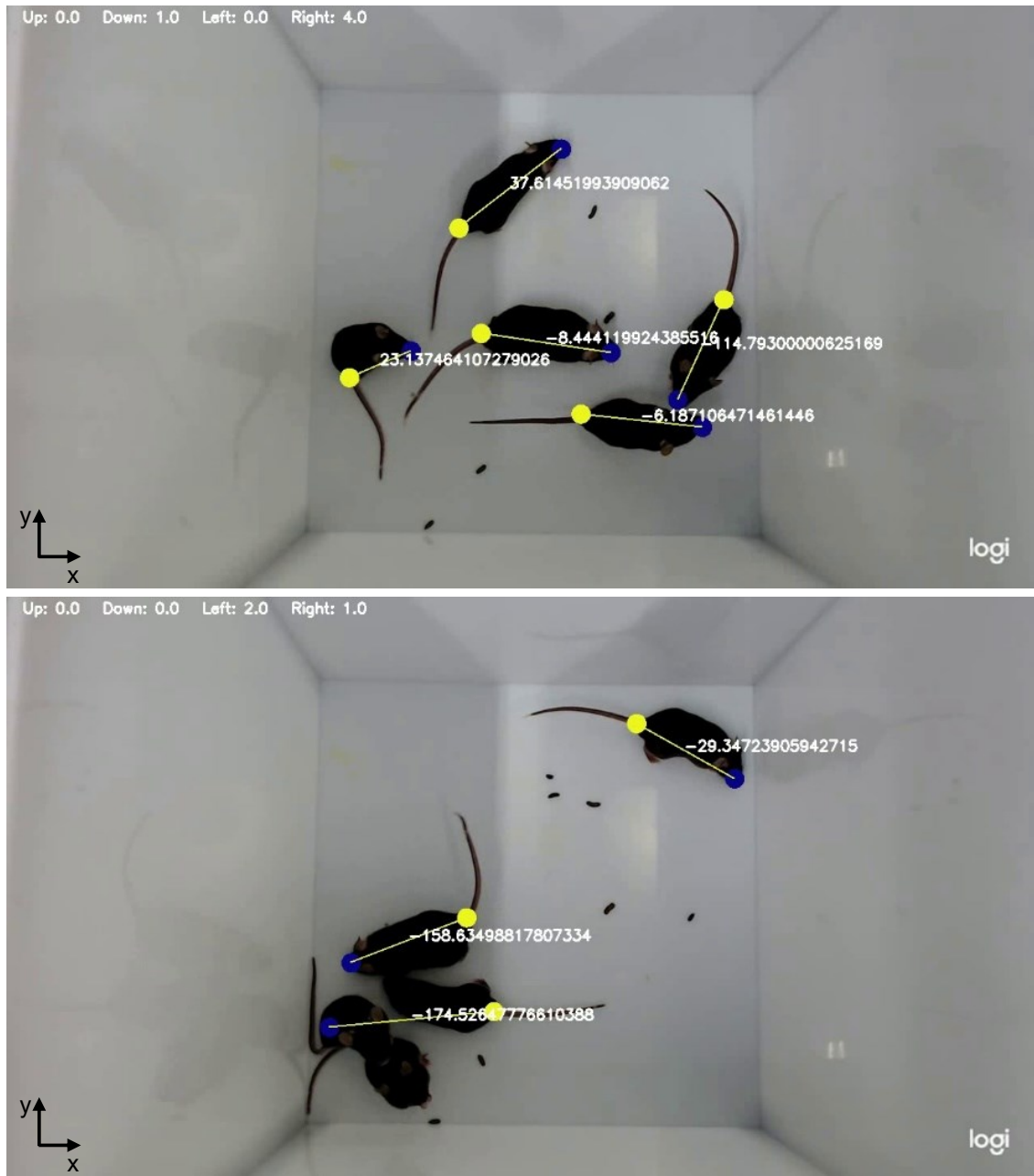


**Figure 3-10.** Overview of ML-enabled adaptive wireless TX system

four coil antennas are installed. Here, we use two pairs of X-shaped coil antennas, each of which is responsible for optimal power delivery according to the motion of an animal along the x-axis or y-axis (Figure 3-11(a)). A webcam on the top of the cage sends a stream of images to the custom-trained DLC[85] model at the rate of 25 fps (Figure 3-11(a)). As a frame arrives, the trained DLC model detects the locations of the snouts and tails, each of which has a confidence score for the prediction (Figure 3-11(b)). The decision threshold for what the ML model appraises as detection is set to 0.6 and any predicted body part with a confidence score below 0.6 is discarded. Next, the ML model quantifies the matching score between all possible combinations of the detected body parts (Figure 3-11(c)). Based on the matching scores, the ML model finds the optimal one-to-one mapping between the detected snouts and tails via the maximum weighted bipartite matching (Figure 3-11(d))[89]. Once the model completes the assignment of each snout-tail pair to every mouse, one can determine the orientation of each mouse in a

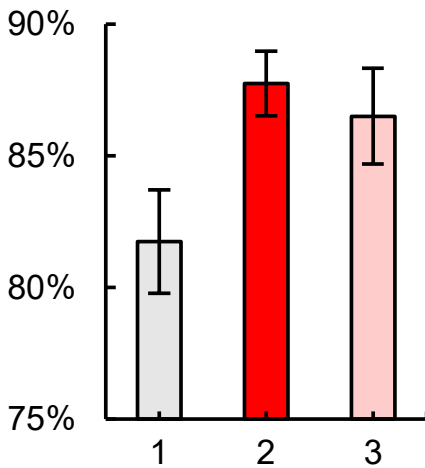


**Figure 3-11.** Illustration of a step-by-step procedure for the ML algorithm



**Figure 3-12.** Two representative images were processed by the ML algorithm. The top image shows perfect alignments of five vectors with a selected coil antenna while the bottom image includes only three vector assignments. It is likely for the two non-assigned mice (or implanted devices) to receive not enough power due to a misalignment between an implanted device and a selected coil antenna.

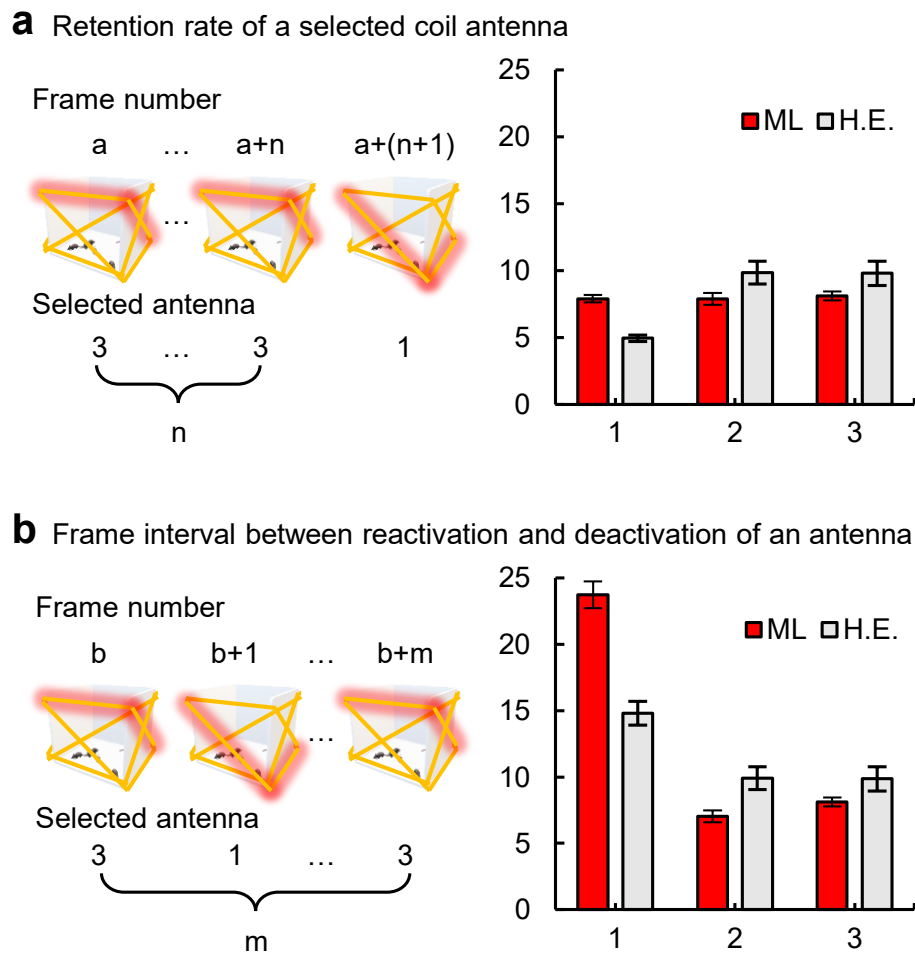
cage. This leads to the identification of the optimal coil antenna index  $i_j^*$  for  $j$ th mouse (Figure 3-11(e)) and creates a control signal for antenna selection. Figure 3-12 shows a representative example of an image processed by the algorithm. Once the controller receives the signal from the ML result, it activates one of the coil antennas. This results in optimum wireless power delivery to mice (implanted devices) (Figure 3-11(f)). The procedures from (a)-(f) are repeated.



**Figure 3-13.** Assessment of detection accuracy for three different antenna structures: 1. 4-coil (each two coil antennas are on the x- and y-axis, respectively), 2. Dual-coil (along the x-axis), and 3. Dual-coil (along the y-axis).

For assessments of the proposed ML algorithm, we use a metric, defined as the percentage of correct predictions for the data tested[90]. Figure 3-13 shows antenna selection accuracy for three different antenna settings: 1) two pairs of X-shaped antenna

coils, one pair of X-shaped coil aligning with 2) the x- or 3) y-axis. Results revealed that the ML algorithm guarantees the accuracy of 80 % or above in every setting that we tested (Figure 3-13). Figure 3-14 shows statistics of the number of frames for two representative cases; how long a selected antenna remains activated (Figure 3-14(a)) and



**Figure 3-14.** Statistics of the number of frames for two representative cases; how long a selected antenna remains activated (**a**) and how many frames (how long an interval) exist between activation of an antenna and reactivation of itself after the first deactivation (**b**); 1. 4-coil (each two coil antennas are on x and y-axis, respectively), 2. Dual-coil (along the x-axis), and 3. Dual-coil (along the y-axis).

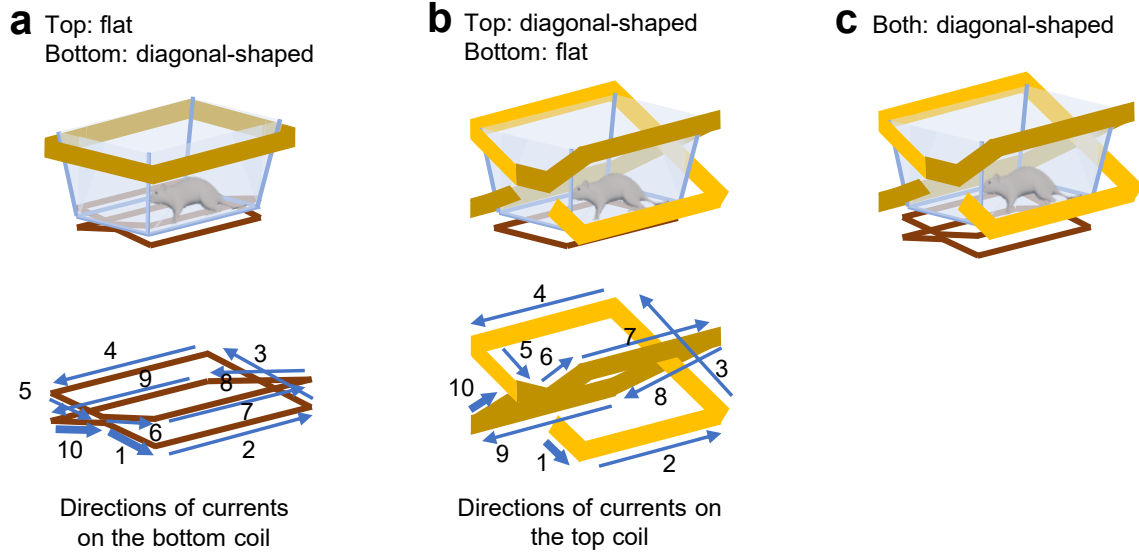


how many frames (or long interval times) it takes between activation of an antenna and reactivation of itself after the first deactivation (Figure 3-14(b)). It is likely that some occupants, to happen that a selected antenna coil covers some of the occupants, not all of them, in a cage may not allow for instantaneous power delivery to the rest due to misalignment between an antenna coil and an implanted device. This leads to a drop in harvesting efficiency and as a result, the devices involved may not be able to deliver enough light to activate a microbial opsin in cell-type specificity, but this can be compensated by stimuli conditions.

### **3.4. Discussions**

#### **3.4.1. Advanced Antenna Structure**

The proposed wireless power TX system utilizes a dual-coil antenna to achieve high transmission efficiency (>60 %). This results in robust activation of an implantable device in a cage. When combined with advanced antenna coil systems, wireless coverage could be further enhanced. Here, we suggest several configurations, including a combination of both flat and diagonally oriented dual-coil structures with Cu strips for the following strategies to support higher output power densities in various angular orientations (Figure 3-15). For example, a diagonal dual-coil design may allow for better power transfer efficiency even in the significantly tilted angles from the in-plane orientation. Multi-diagonal layouts can further enhance the efficacy and the uniformity of wireless transmittance over the bottom of the cage and across large areas. The proposed efforts on this advanced technological development will improve wireless



**Figure 3-15.** The advanced dual-coil and dual-layered configurations: (a) top is flat and bottom is diagonal-shaped; (b) top is diagonal-shaped and bottom is flat; and (c) top and bottom are diagonal-shaped.

coverage and eliminate a residual dependence of transmitted power on the relative orientation angle between the TX antenna and the implantable device. We expect that this improved power transmission efficiency without relative angular orientation of the implanted device will reduce the transmitted power to  $<2$  W, which is lower than the existing single coil antenna systems ( $>8$  W), as well as minimizing the undesired effects related to electromagnetic absorption in tissues[91], [92].

### 3.4.2. Expansion of Time Division Multiplexing

Our proposed channel isolation and time division strategies are based on wireless optoelectronics implants that transmit stimulus signals by intermittent time differences.

In this study, we demonstrate a high-throughput wireless power TX/RX platform with a total of eight cages activated in order under the assumption that target neurons require a 25 Hz frequency (5 ms on/35 ms off) stimulus. The proposed method is capable of multi-cage application following the stimulation cycle of neural signals, but inhibition experiments where light sources need to operate continuously cannot be executed in the current multi-cage system manner. Due to the nature of electromagnetic interference, this multi-cage scheme cannot simultaneously transmit power using adjacent antennas at the same resonant frequency. However, this limitation can be overcome by modifying the implantable device with a circuit employing a supercapacitor. The aforementioned strategy expects that a supercapacitor, which has stored power when the antenna is activated, can keep the LED lights bright enough while that antenna is deactivated. In sum, the proposed multi-cage system based on channel isolation and time division strategies allows for all *in vivo* experiments regardless of the excitation/inhibition of the neurons.

### **3.4.3. Optimized Multi-coil Antenna System via an ML-based Algorithm**

The proposed ML algorithm paired with advanced coil antennas enables robust activation of implantable optoelectronic devices in a cage. When a normal vector of an implanted device is aligned with that of the TX coil antenna, maximum wireless transmission occurs between the two coils[93]–[95]. When misaligned, the efficiency significantly drops. In general, reconfiguration of antennas such as adjustment of the gap between the coil and the ground without rematching of the impedance is not

recommended once they are installed in a cage[96]: doing so causes transmission efficiency to drop significantly. In contrast, animals freely behave in a cage, suggesting that angles or orientations between the implanted device and the TX coil antenna vary at different times. This could be problematic. For example, two vectors could become misaligned when an animal leans against the wall of a cage by standing on its hind legs or curls up. This results in a significant drop in harvesting efficiency and thereby no activation of the implanted device. When combined with an advanced antenna technology and an impedance matching circuit for switching, the proposed ML algorithm allows for a selection from prearranged pairs of antennas or adjustment of antenna formation, thereby leading to a realignment of the TX coil antenna with the implanted devices, which enables full wireless coverage of a cage. What this suggests goes beyond just the meaning of TX system development. This research focuses only on light delivery, making it easy to use implantable devices that demand low-power consumption. The aforementioned ML algorithm-adapted TX systems can deliver robust and homogeneous power to the implanted device, which can significantly increase the power available to the implant. In other words, high-performance chips can be mounted on the implanted devices, revealing new research directions that allow simultaneous nervous signal recording and stimulation, like a fully implantable closed-loop system in an animal.

#### **3.4.4. Applications to Scalability Using ML Algorithms**

We proposed an ML algorithm to analyze the orientation of each animal by

extracting the positions of the snout and tail pairs in several animals. However, this is only a small event compared to the research implemented ML algorithms, and there are a number of directions to improve the quality of the research depending on how the ML system is applied. For example, we envision an ML-based algorithm that analyzes the jaw joint and head movements of an animal to specify behavior and predict the amount of food they eat. We could then decipher the amount of food consumed per day by the animal by examining their food intake behaviors, poses, and patterns. This algorithm can support the accurate digitization data by objectifying food intake information for average, obese, and underweight mice. These data could be used for the development of better therapeutics for obesity. As such, ML-based algorithms are not only engineering aids for, e.g., increasing the efficiency of wireless power transfer systems and implantable optogenetic devices, but are also expected to expand their utility into various fields, including neuroscience, physiology, kinematic research, as well as behavioral analysis.

## 4. *IN VIVO* VALIDATION OF THE PROPOSED WIRELESS TELEMETRY SYSTEM\*

### 4.1. Introduction

Vagal afferent fibers are unique in that they innervate many different organ systems and receive direct inputs from those organs[97]–[99]. For example, meal cessation is to a large extent mediated by feedback from the gut to the brain. Distension of the stomach, the absorption of nutrients and the release of satiety hormones (GLP-1, peptide YY, and cholecystokinin) can activate vagal sensory afferents that relay satiety signals to the NTS in the hindbrain[100], [101]. Neurons in NTS then relay signals to the PBN and other nuclei to suppress feeding[102]. Because the vagus is a major origin of satiation signals, it is a logical place to intervene to treat obesity. Furthermore, several studies in obese animals indicate that the vagus becomes insensitive to satiation signals. Consequently, the ability to bypass this obesity-induced insensitivity and experimentally activate the vagus has significant potential[103], [104]. However, a human (or mouse) nodose ganglion contains 100,000 (or 5,000) neurons which can innervate multiple internal organs[105]. Therefore, cellular level control of nerves is crucial to this pursuit, and all the experiments using non-specific approaches that suggest that the vagus becomes insensitive to nutrients and hormones in response to obesity are indirect[106].

---

\*Reprinted with permission from “Organ-specific, multimodal, wireless optoelectronics for high-throughput phenotyping of peripheral neural pathways” by Kim, W.S.; Hong, S.; Gamero, M.; Jeevakumar, V.; Smithhart, C.M.; Price, T.J.; Palmiter, R.D.; Campos, C.; Park, S.I, 2021, *Nat Commun*, 12, 157, © 2021 by Springer Nature.

The proposed wireless platform can offer capabilities in specific targeting and long-term modulation of neuronal populations in a freely behaving animal with chronic stability in operation. Its utilities have been demonstrated in *in vivo* experiments using *Calca-Cre* mice. Our research finds that calcitonin gene-related peptide (CGRP) neurons innervating the mucosa rather than the stretch receptors, can inhibit food intake and elicit anxiety-related behavior. The results suggest interesting experiments that can determine whether appetite suppression induced by gastric vagal afferent activation is attenuated in obese mice and whether chronic activation of vagal afferent endings in the stomach can reverse obesity. Identification of viscerosensory pathways that suppress appetite will have direct clinical importance for potentially developing novel therapeutic targets for treating obesity.

## **4.2. Methods**

### **4.2.1. Organ-Specific, Wireless, Gastric Optogenetic Device Implantation**

Under surgical anesthesia (isoflurane, 1-2% inhalation), the animal's ventral side was shaved, sterilized with three alternating scrubs of betadine and alcohol, and the surgical field was restricted with sterile drapes. With the animal on its back, a 2 cm skin incision was made along the abdominal midline from the xiphoid cartilage extending to the mid-abdomen, and a second cut into the abdominal wall exposed the stomach for device implantation. Ringed forceps were used to gently grasp the fore-stomach and pull it out of the abdominal cavity onto gauze soaked with sterile saline. Fine-tipped Dupont forceps were then used to puncture the stomach fundus and thread the  $\mu$ LED tether in

and out of the stomach. With the  $\mu$ LED inside the stomach, the tether was secured in placed with purse-string sutures (5-0 PGA). The device harvester was then placed in the abdominal cavity and the stomach was placed back into its normal orientation. The abdominal wall was closed with interrupted stitches using absorbable suture (5-0 PGA), and the skin with non-absorbable suture (6-0 silk). Mice received analgesics during the surgery (ketoprofen, 5 mg kg<sup>-1</sup>) and daily post-operative care (provided with hydrating gel, monitor food intake and body weight). For multimodal device implantation, an incision was made in the abdominal cavity and the device was implanted with the blue LED positioned towards the thoracic cavity and the green LED towards the abdominal cavity. After recovery from surgery, all animals received daily post-operative care.

#### **4.2.2. Meal-Pattern Analysis**

To examine whether mice tolerate stomach device implantation, one group of mice was implanted with the device whereas another group underwent a sham surgery where the abdomen was opened near the stomach but it was not punctured nor implanted with a device. Two weeks after the surgeries, mice were placed in food-monitoring home cages (BioDAQ, v. 2.2). Feeding records were analyzed using BioDAQ Viewer (software v. 2.2.01). A feeding bout ( $\geq 0.01$  g) was defined as a meal if  $\geq 0.06$  g of food was ingested and if it was separated from another meal by  $\geq 5$  min.

#### **4.2.3. Fasting and Refeeding Experiments**

Mice were food-restricted overnight (16 h) and refed the following morning.



Food intake was manually measured 1 h, 2 h, and 3 h after refeeding. The same animals underwent multiple fasting-refeeding tests to examine different optogenetic stimulation parameters: no stimulation (RF antenna off), 10 Hz, and 20 Hz optogenetic stimulation (5 ms pulse width; RF power 4 W). Experiments were conducted 5 days apart.

#### **4.2.4. Real-Time, Place-Preference and Open-Field Assays**

Mice were placed in an RTPP box consisting of two chambers ( $20 \times 18$  cm) and a small transition area. Antennas were installed in both chambers, but only one chamber was connected to an RF generator to continuously deliver RF power (20 Hz, 5 ms pulse width, 4 W). The time spent in each chamber (20 min trial) was analyzed using video-tracking software (EthoVision XT 10, Noldus). Mice were placed in the center of a  $40 \times 40$  cm square open-field arena with non-transparent white Plexiglas. The total distance moved and time in the center ( $20 \times 20$  cm imaginary square), during the 10 min trial, were analyzed with video-tracking software with EthoVision. An RF antenna provided wireless power (20 Hz, 5 ms pulse width, 4 W) throughout the entire behavior box.

#### **4.2.5. Statistics**

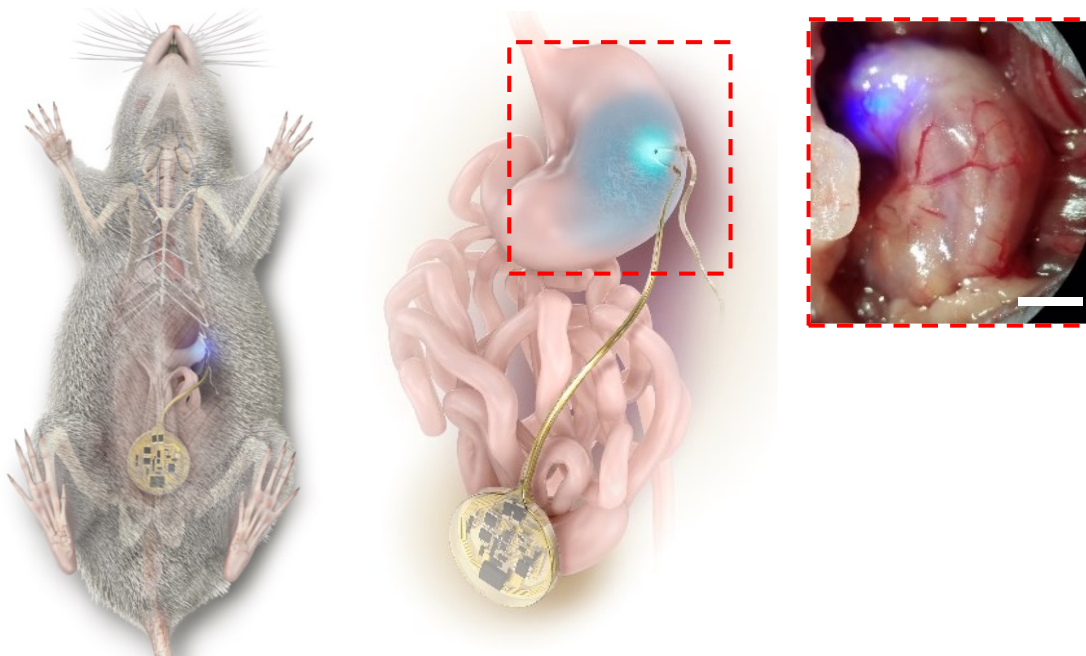
Data were analyzed using Prism 5.0 (GraphPad software). Sample sizes were estimated based on prior experience and expected variability in feeding behavior[107]. We excluded an animal from data analysis if post hoc histological analysis showed no viral transduction as indicated by an absence of tdTomato fluorescence. For graphs comparing two experimental conditions, we used unpaired two-tailed Student's *t*-test.

We analyzed data sets (multiple treatments and time-points) with repeated-measures two-way analysis of variance tests (time repeated factor) and Tukey's post hoc tests. All data sets were conducted using Shapiro–Wilk normality test, and all passed the normality tests.

### 4.3. Results

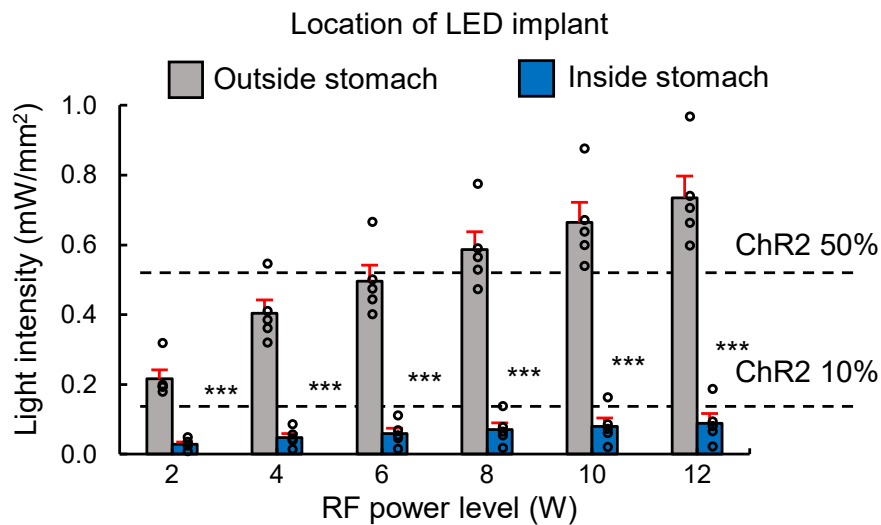
#### 4.3.1. Measurements of Light Propagation in the Stomach

An illustration of the fully implantable wireless device shows the general strategy

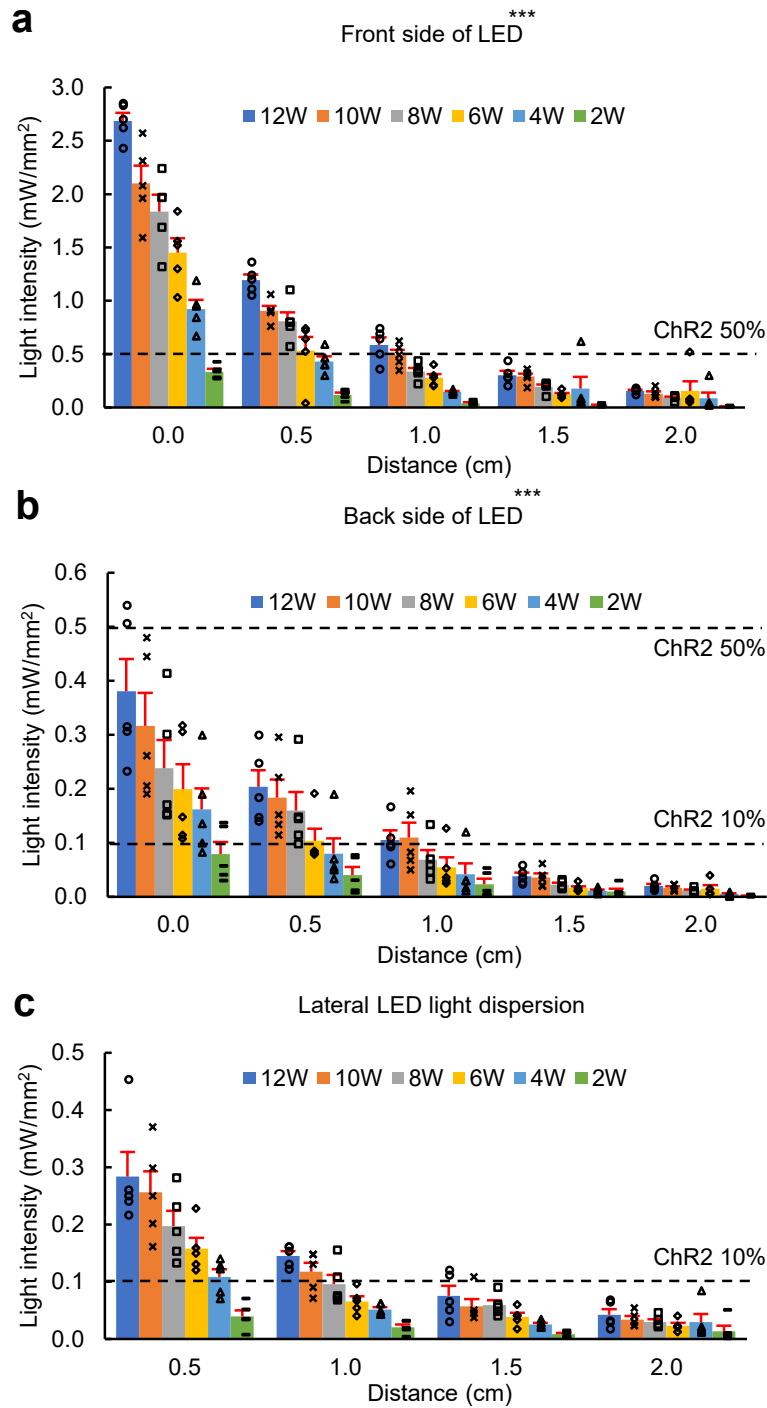


**Figure 4-1.** Illustration of a soft, wireless gastric optogenetic implant: device implants location (left and middle) and a photo of wireless LED operation in the stomach of a mouse (right); scale bar 5 mm.

for targeting a  $\mu$ LED inside the stomach (Figure 4-1). The device consists of an analog, front-end electronic circuit for RF harvesting (5.5 mm radius and 1 mm thickness) and a tether that supplies current to a  $\mu$ LED. It harvests RF energy from a remotely located wireless RF power system, converts RF energy into optical energy, and illuminates targeted regions in the stomach. The  $\mu$ LED is situated in the middle rather than the end of a tether, allowing the tether to be threaded in and out of the stomach and secured at two contact points. We found that the tether remains secure with purse-string sutures. The ultra-thin tether (0.4 mm wide by 0.2 mm thick) is more than 3-times smaller than insulin syringe needles used for intraperitoneal injections and tubing used for intragastric infusions[64]. To determine the utility of the optoelectronic system, we investigated the



**Figure 4-2.** Light intensity measurements comparing LED implantation inside versus outside the stomach ( $n = 5$ ,  $p < 0.01$ ), with varying RF powers ( $p < 0.001$ ). Dashed horizontal lines indicate light intensity needed for 10 % and 50 % maximal activation of channelrhodopsin2. Bar graphs are mean  $\pm$  SEM. Statistical comparisons were made using two-way repeated-measures ANOVA, Tukey's post hoc; \*\*\*  $p < 0.001$ .



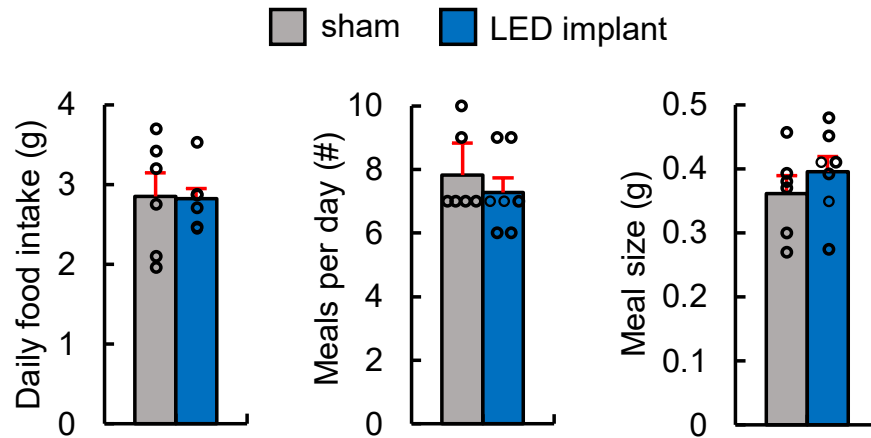
**Figure 4-3.** Light intensity measurements during varying RF wireless powering ( $p < 0.001$ ) of the gastric optogenetic device ( $n = 5$ ) and varying distances ( $p < 0.001$ ) from the LED. Measurements were taken from the front side (a), back side (b), and lateral side of the LED (c). Bar graphs are mean  $\pm$  SEM. Statistical comparisons were made two-way repeated-measures ANOVA; \*\*\*  $p < 0.001$ .

role of stomach vagal afferent endings in feeding behavior. We began by analyzing the  $\mu$ LED light spread and identified RF powering parameters needed for organ specificity. As expected, securing the  $\mu$ LED inside the stomach significantly restricts light spread (Figure 4-2), in contrast to surface affixation which results in light back-scatter intensities well above the threshold for opsin activation[108] (Figure 4-3). Finally, tests in mice showed that the pre-curved tether was functional for over a month, while the post-curved structure stopped working three days after implantation (Figure 2-10) and the multiplexing TX system enabled tests to conduct 8 individual cages simultaneously (Figure 3-6).

#### **4.3.2. Sham Study**

We examined whether implantation of the stomach device is well tolerated by showing that ad libitum food intake of mice implanted with the device was the same as sham operated mice (Figure 4-4). These results indicate that our wireless device should allow precise optogenetic manipulations in awake, behaving mice. A recent study identified genetically distinct vagal afferent neurons in the nodose ganglion that innervate the stomach and express either *Calca*, *Sst*, *Gpr65*, or *Glp1r* genes[107]. In contrast to *Sst* and *Gpr65*, which exhibit either mechanosensitive morphological endings in muscle layers (*Glp1r*) or chemosensitive endings in the mucosal layer (*Sst*, *Gpr65*), *Calca*<sup>+</sup> neurons form spatially-restricted chemosensitive mucosal endings in the corpus versus mechanosensitive intramuscular arrays in the stomach antrum[107]. Identification of a role for stomach chemosensation in appetite control has been elusive[109];

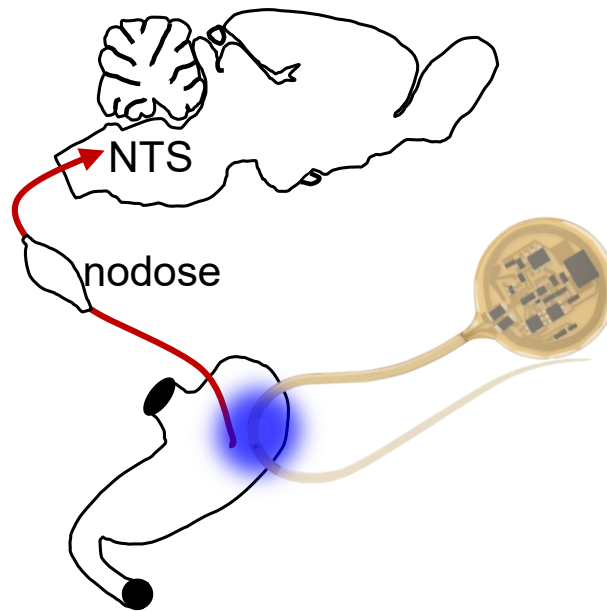
therefore, we used our wireless device to selectively activate *Calca*<sup>+</sup> vagal afferent chemosensitive endings in the corpus region of the stomach.



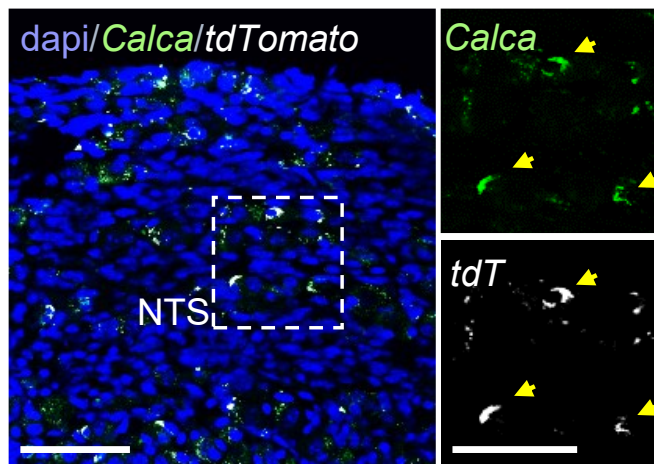
**Figure 4-4.** Comparison of total food intake (left), number of meals (middle), and meal size (right) in mice implanted with LED device ( $n = 7$ ) or sham operated ( $n = 6$ ) ( $p = 0.71$ ). Bar graphs are mean  $\pm$  SEM. Statistical comparisons were made using two-way repeated-measures ANOVA, Tukey's post hoc.

### 4.3.3. Optogenetic Manipulation of Gastric Vagal Sensory Endings

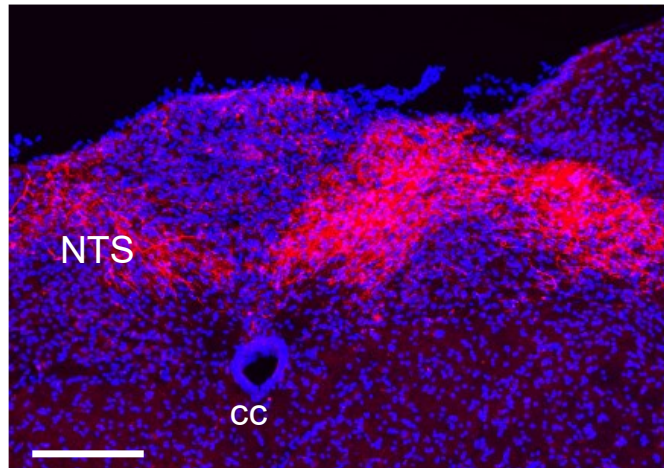
Overview of the activation of *Calca*<sup>+</sup> stomach vagal afferents is shown in Figure 4-5. To gain cell-type specificity, AAV9 was injected into the nodose ganglion of *Calca*Cre:GFP transgenic mice to introduce Cre-dependent ChR2:tdTomato opsin expression or a control group with just tdTomato fluorescent reporter (Figure 4-6 and Figure 4-7). Precise anatomical specificity was achieved by implanting the  $\mu$ LED into the fundus, immediately adjacent to the corpus. While *Calca*<sup>+</sup> vagal afferents do not



**Figure 4-5.** Schematic illustration of the activation of *Calca*<sup>+</sup> stomach vagal afferents. *Calca*-Cre transgenic mice received a left nodose ganglion injection of AAV9-DIO-ChR2:tdTomato or AAV9-DIO-tdTomato control virus. The LED was implanted in the stomach corpus-function junction.



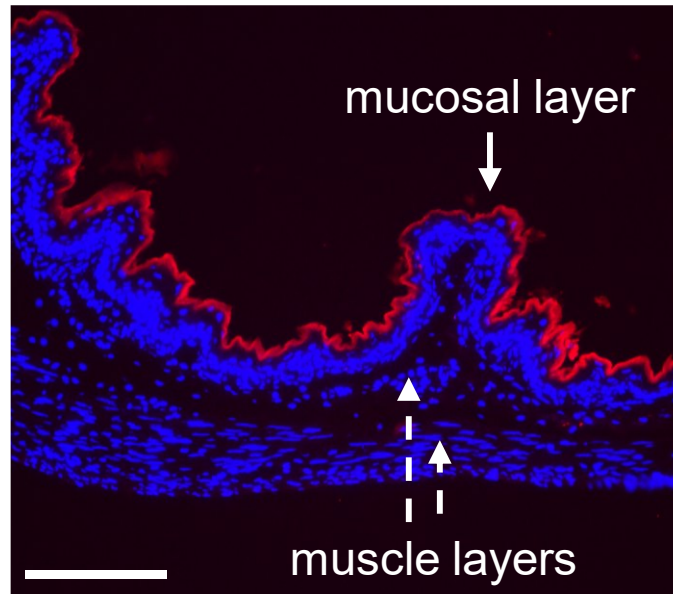
**Figure 4-6.** *Calca*-Cre transgenic mice received nodose ganglion injection of AAV9-DIO-ChR2:tdTomato. Images show fluorescence *in situ* hybridization of tdTomato and *Calca* mRNA, demonstrating the cell-type specificity of transgenic/viral approach; scale bars 25  $\mu$ m.



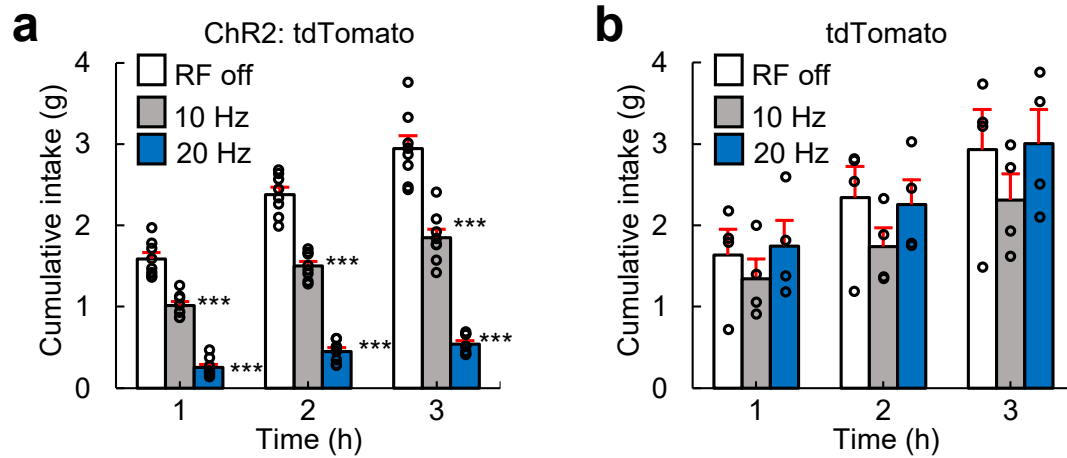
**Figure 4-7.** tdTomato fluorescence labeling of central *Calca*<sup>+</sup> vagal afferent endings in the nucleus of the solitary tract (NTS); scale bar 25  $\mu$ m.

innervate the fundus, we implanted the device away from the antrum to avoid activation of mechanosensitive fibers (Figure 4-8). Several weeks after recovering from device implantation, mice were fasted overnight and refed the following morning. Compared to no stimulation (RF antenna off), optogenetic activation produced robust suppression of food intake during refeeding, with greater stimulation frequencies almost completely suppressing intake (Figure 4-9a). Importantly, activation of the device in the control group without ChR2 did not alter feeding behavior, indicating that RF signals and activation of the device in itself do not influence feeding (Figure 4-9b). To further establish that the appetite suppression was due to activation of vagal afferent endings in the stomach, we compared these results to separate cohorts of mice implanted with six non-attached  $\mu$ LEDs in the abdomen. Although optogenetic stimulation of vagal afferents in this manner suppressed feeding, the effect was not as robust despite

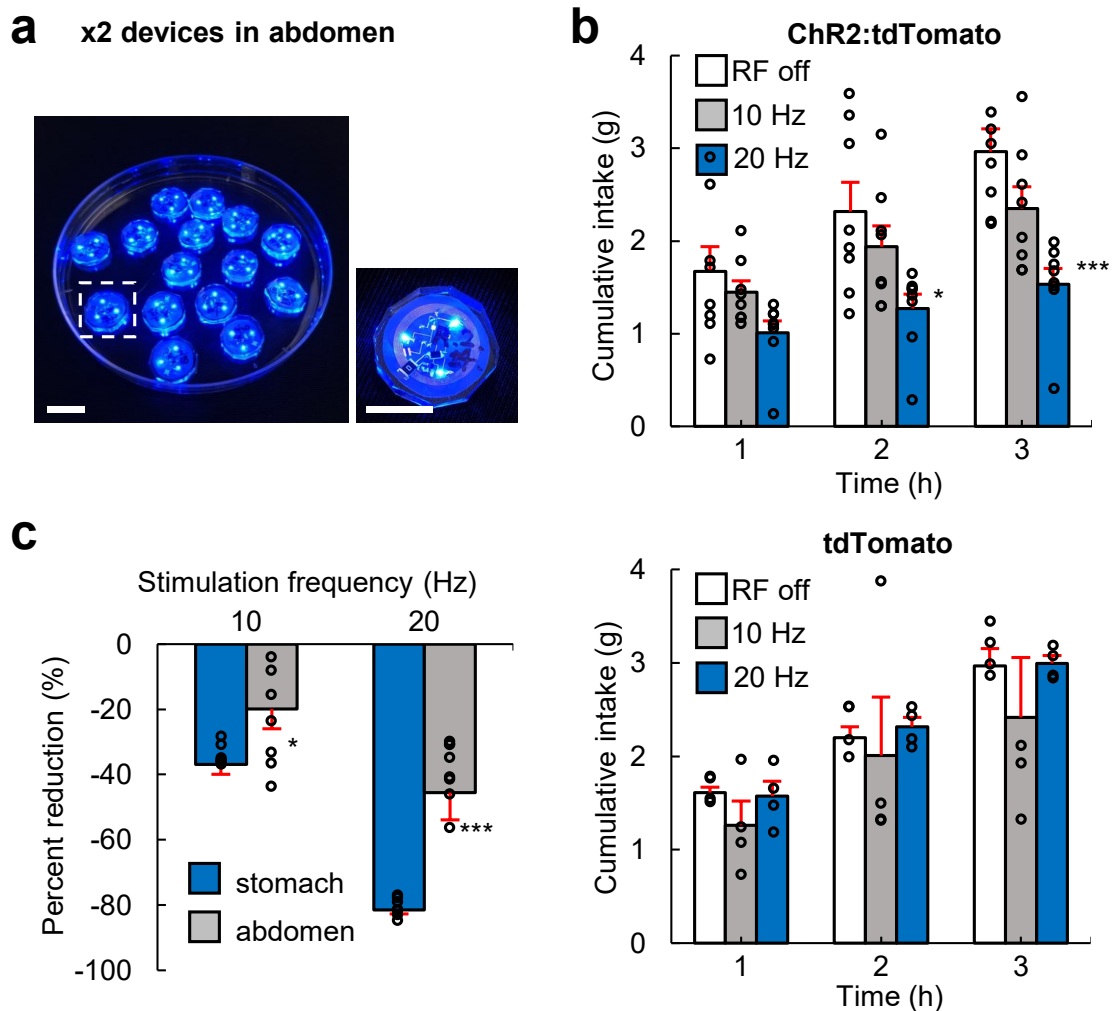




**Figure 4-8.** Fluorescence labeling of peripheral *Calca*+ vagal afferent endings in the stomach mucosal layer; scale bar 50  $\mu$ m.



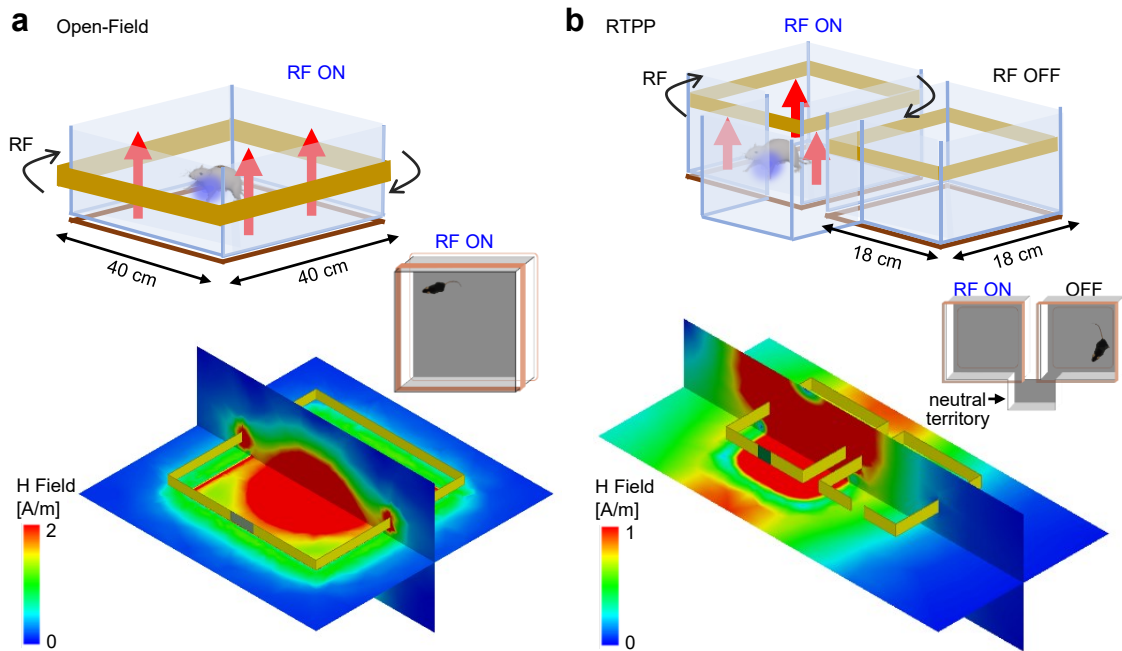
**Figure 4-9.** Frequency-dependent suppression of food intake in the ChR2:tdTomato group ( $n = 8$ ). (c) The tdTomato control group did not suppress food intake during photostimulation ( $n = 4$ ) ( $p = 0.06$ ). Bar graphs are mean  $\pm$  SEM. Statistical comparisons were made using two-way repeated-measures ANOVA, Tukey's post hoc; \*\*\*  $p < 0.001$ .



**Figure 4-10.** Abdominal activation of *Calca*<sup>+</sup> vagal afferent fibers. (a) Picture showing wirelessly powered LED device; two of these devices were inserted into the abdomen of *Calca*-Cre transgenic mice with left nodose ganglion injection of AAV9-DIO-ChR2:tdTomato or AAV9-DIO-tdTomato control virus; scale bar 5 mm. (b) top, frequency-dependent suppression of food intake during ChR2 activation of vagal afferents ( $n = 8$ ), bottom, no appetite suppression in tdTomato control group ( $n = 4$ ) ( $p = 0.80$ ). (c) Percent reduction of food intake (compared to RF off) during 10 and 20 Hz stimulation of *Calca*<sup>+</sup> vagal afferent endings using the stomach LED implant or non-attached LEDs (ChR2,  $n = 8$  per group) (interaction,  $p = 0.01$ ). Bar graphs are mean  $\pm$  SEM. Statistical comparisons were made two-way repeated-measures ANOVA, Tukey's post hoc; \*  $p < 0.05$ ; \*\*  $p < 0.01$ ; \*\*\*  $p < 0.001$ .

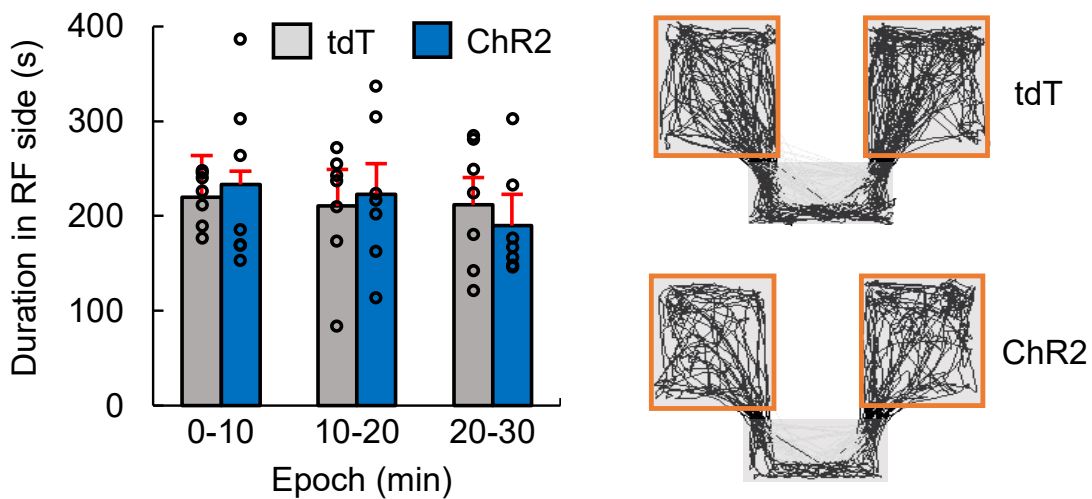
stimulating with six  $\mu$ LEDs rather than a single  $\mu$ LED directly implanted inside the stomach (Figure 4-10). Furthermore, the non-anchored LED approach required increased operating power to compensate for light dissipation, resulting in greater heat generation and potential tissue damage[110], [111]. Thus, the gastric optogenetic implant enables more robust optogenetic activation using less wireless power.

Appetite suppression can be associated with positive valence, potentially due to removal of aversive hunger signals[112], or aversion in response to harmful stimuli, such as uncomfortable gastric distension[113] or food poisoning[114]. To investigate affective mechanisms by which *Calca*<sup>+</sup> gastric vagal afferent neurons might suppress

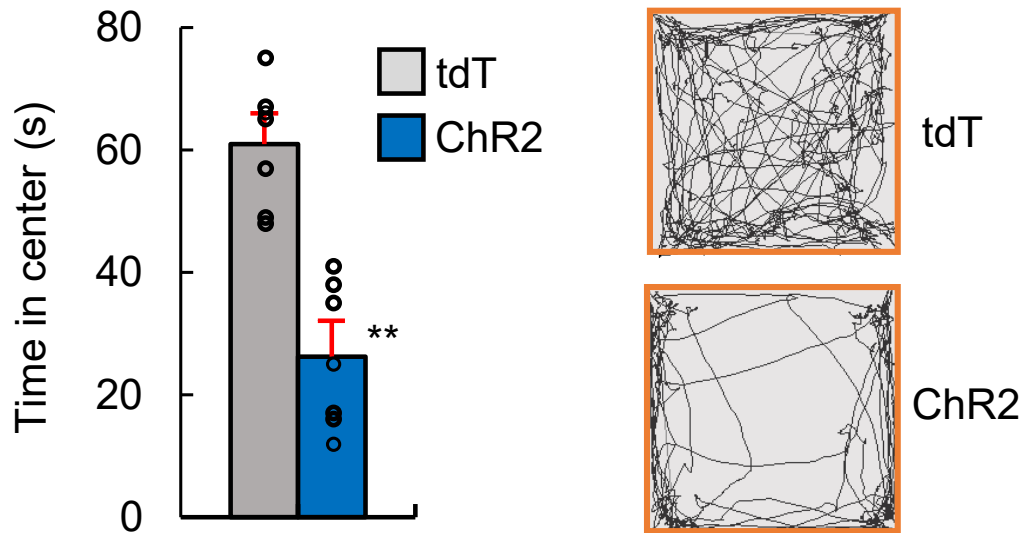


**Figure 4-11.** Schematic illustration of an experimental assay (top) and distributions of the electromagnetic field in the assay (bottom) for open-field (a) and RTPP (b), respectively.

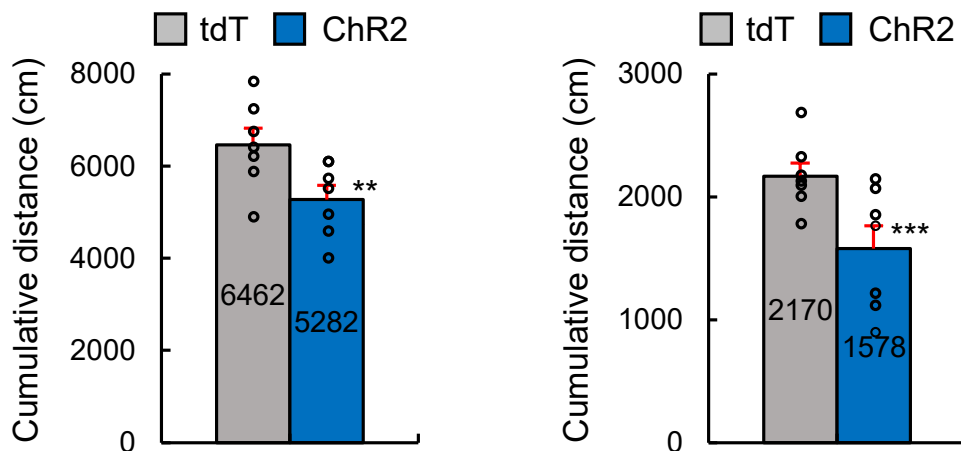
appetite, we constructed oversized dual-coil antennas for robust optogenetic activation in various behavior boxes (Figure 4-11 and Table 3-1). In an RTPP assay, mice were placed in a two-chamber box with RF power only in one chamber to determine whether mice form an aversion or preference for the optogenetic-stimulation chamber. Surprisingly, we did not observe differences in place preference or avoidance (Figure 4-12), similar to optogenetic stimulation of other vagal afferent cell-types that innervate the GI tract[107]. Conversely, an open-field assay demonstrated that optogenetic stimulation reduced the time mice spend in the center, indicative of anxiety-like behavior and suggesting that activation of *Calca*<sup>+</sup> gastric vagal afferent fibers might be aversive (Figure 4-13). We analyzed the locomotor activity from open-field and place-preference



**Figure 4-12.** Activation of the LED device (20 Hz light pulses) did not induce a place preference nor avoidance in both ChR2 and tdTomato groups ( $n = 7$  per group) (left). Representative traces for RTPP assay (right). Bar graphs are mean  $\pm$  SEM. Statistical comparisons were made using two-way repeated-measures ANOVA, Tukey's post hoc.

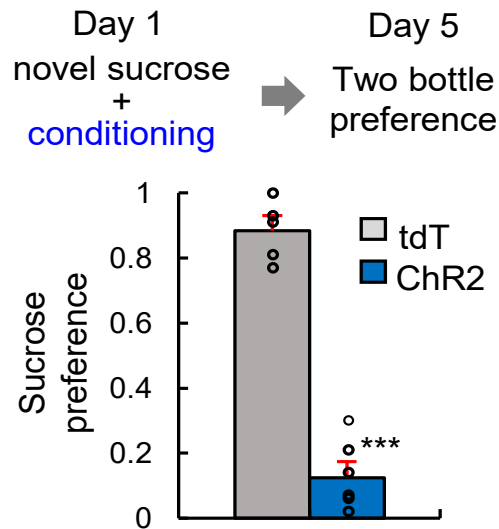


**Figure 4-13.** Photoactivation (20 Hz light pulses) of *Calca*<sup>+</sup> gastric vagal afferents decreased time spent in center of large open field box ( $n = 7$  per group) ( $p = 0.31$ ) (left). Representative traces from open-field test (right). Bar graphs are mean  $\pm$  SEM. Statistical comparisons were made using two-tailed  $t$ -tests; \*\*  $p < 0.01$ .



**Figure 4-14.** Locomotor activity comparison in the assays for RTPP (left), and open-field box (right). Both were conducted for 30 minutes and  $n = 7$  per each group. Bar graphs are mean  $\pm$  SEM. Statistical comparison was made using two-tailed  $t$ -test; \*\*\*  $p < 0.001$ .

tests, which revealed decreased locomotion during optogenetic activation of *Calca*+ gastric vagal afferent (Figure 4-14); presumably, the mice feel aversion and have decreased motivation.



**Figure 4-15.** Mice were exposed to a novel sucrose solution on Day 1 followed by optogenetic activation of vagal sensory fibers (20 Hz). On Day 5, mice were water-restricted overnight and then given simultaneous access to a bottle of sucrose and a bottle of water. The graph is the sucrose preference score (ChR2,  $n = 7$ ; tdT,  $n = 5$ ). Bar graphs are mean  $\pm$  SEM. Statistical comparisons were made using two-tailed  $t$ -tests; \*\*\*  $p < 0.001$ .

In addition, GI signals are closely associated with taste-sensory signals[115], suggesting that a learned food preference/aversion assay might be most indicative of the mechanism underlying appetite suppression. To test this hypothesis, mice were

habituated to overnight water-restriction for several days and then given access to 5 % sucrose solution followed by optogenetic stimulation of *Calca*<sup>+</sup> vagal afferent fibers for 4 h. Three days later mice were offered the choice of water or 5 % sucrose. This two-bottle preference test revealed that activation of stomach *Calca*<sup>+</sup> vagal afferents conditioned mice to avoid the sucrose solution (Figure 4-15). This suggests that appetite suppression occurs via a negative-valence mechanism that alters taste preferences. These results identified a role for stomach mucosal *Calca*<sup>+</sup> vagal afferents in appetite suppression and revealed a mechanism by which appetite suppression occurs.

#### **4.4. Discussions**

##### **4.4.1. Chronic Stimulation of Vagal Nerve Endings in Obese Animals**

Most existing approaches, where the focus is on neural circuits in the brain[42], [43], [47], [75], [116], are unable to monitor satiety signals in response to food intake and hence do not address some of the most important questions in the field, namely; 1) how is satiety information coming from the gut during or after the feeding process, 2) when are satiety signals from the gut relayed, and 3) how are long neurons, thought to be involved in adiposity negative feedback mechanism, active during or after feeding. A working hypothesis is satiation mechanisms in obese animals will differ from those of healthy animals[101]. Several studies in obese animals indicate that the vagus nerve becomes insensitive to satiation signals. However, these studies use a non-specific approach, and thus the experiments that suggest that the vagus becomes insensitive to nutrients and hormones in response to obesity are indirect[53]. Our approach allows for

selective regional photoactivation of neuronal populations and will enable experiments that determine whether chronic inhibition of vagal activity in obese animals can restore functions that regulate food intake or reverse the insensitivity. This research ultimately has the potential for identification of interventions to treat obesity.

We aim to target afferent fibers of the vagus nerve that project from the gut to the NTS in the hindbrain. Afferent fibers of the vagus nerve control the flow of satiety information and recording neural activity from vagal afferent nerves can provide significant insights into understanding of dynamic interplay between the brain and the gut during or after feeding[117]. We plan to use light-sensitive proteins for optogenetic manipulation of vagal fibers in mice that were exposed to a high-fat diet for two months and that were infected with an PHP.S-Ef1a-DIO-ChR2:YFP for stimulation & PHP.S-Ef1a-DIO-Jaws:tdTomato for inhibition. This will allow the implanted integrated wireless device in the targeted region to measure the selective expression of ChR2 & Jaws in afferent fibers of neurons. Specifically, the system allows activation and/or inhibition of vagal afferent fibers and for us to examine the effect on food intake, water intake, valence, and conditioned taste aversion. In parallel, we will perform *in vivo* recording experiments where the implanted integrated wireless device records neural activity from vagal afferent fibers in a freely behaving obese mouse in a cage after a fast, during feeding, and after feeding. Such efforts will greatly advance our understanding of the flow of satiety information and lead to identification and dissection of subpopulations of gastric viscerosensory pathways involved in the feeding. Collectively, research findings from this work will facilitate development of ultimate therapeutics for



the treatment of obesity. All *in vivo* experiments will occur within Prof. Knight's lab at UCSF under an approved Animal Use Protocol (AUP).

## 5. CONCLUSIONS\*

While many classical studies have established the important role of visceral signals in controlling behavior[103], [118], these surgical- and chemical-denervation experiments lacked organ specificity and did not reveal the identity of sensory neurons that can serve diverging functions. Here, we developed wireless  $\mu$ LED devices that permit organ-specific, optogenetic manipulations and an ultra-efficient wireless telemetry system for powering multiple cages. The miniaturized wireless device enabled precise optogenetic stimulation of genetically defined vagal afferents innervating the mouse stomach, revealing a function for *Calca*<sup>+</sup> mucosal sensory endings in suppressing food intake via a negative valence mechanism. Critically, the pre-curved, sandwiched construction significantly extended the lifespan of the  $\mu$ LED device and allowed for the testing of various stimulation parameters and behavioral tests within the same subjects. We envision that the current device could be used to optogenetically manipulate neural circuits throughout the GI tract and other hollow organs, such as the intestine, with little or no modification.

Prior methods for optogenetic activation of vagal afferents in awake mice have either lacked organ specificity[107] or involved gut injections of a retrogradely transported opsin virus and fiber-optic implantation in the hindbrain where vagal

---

\*Reprinted with permission from “Organ-specific, multimodal, wireless optoelectronics for high-throughput phenotyping of peripheral neural pathways” by Kim, W.S.; Hong, S.; Gamero, M.; Jeevakumar, V.; Smithhart, C.M.; Price, T.J.; Palmiter, R.D.; Campos, C.; Park, S.I, 2021, *Nat Commun*, 12, 157, © 2021 by Springer Nature.

afferents terminate[51]. While the latter provides organ specificity, retrograde viruses can be limited by tropism and incomplete infection of certain cell types. Moreover, vagal afferents express neuropeptides in their peripheral endings that are hypothesized to be released in the gut to exert efferent functions[54]. In other systems, such as somatosensation, the peripheral release of neuropeptides by afferent fibers can contribute to behaviors by sensitizing other afferent subtypes to ongoing stimuli[119]. Finally, fiber-optics cannot be used for optogenetically manipulating the enteric nervous system nor splanchnic sensory afferents, which synapse in the spinal cord. Investigating the function of these neural circuits and hypotheses, therefore, requires peripheral optogenetic stimulation that is now possible with the proposed wireless gastric optogenetic implant. Multimodal features could further enable investigation of peripheral interactions by using different-colored  $\mu$ LEDs to activate corresponding color-sensitive opsins expressed by separate neural substrates or multiple organs simultaneously and/or independently.

In addition to extending optogenetic functionality to the peripheral nervous system, we introduced advancements in wireless telemetry that generally improve the scalability and usability of optogenetics. The dual-coil antenna system, which enables reliable and complete wireless coverage, is easily constructed using inexpensive copper wire secured onto cardboard or plastic backing. The multiplexing approach further allows for the testing of large experimental cohorts, which was particularly important for our studies because of the extended duration of feeding behavior tests. This system can be set up in under an hour, is simple to operate, and dramatically decreases the cost and

time required for conducting optogenetic experiments. Furthermore, the wireless telemetry system has broad applicability for powering optogenetic devices in the periphery, brain[48], [116], or other wireless devices, such as those that measure bioelectrical signals[55].

In this work, we developed an ML algorithm based on a custom-trained DLC for real-time detection of the snouts and tails of multiple mice in a video frame, where maximum-weighted bipartite matching was used to match the snout and tail of each mouse. We used a matched pair of body parts (i.e., a snout-tail pair) to infer the orientation of a given mouse, which can subsequently be used to optimally control the TX coil antenna for efficient wireless power delivery. While the proposed algorithm yields fairly accurate predictions as discussed before, we expect that its performance may be further enhanced by incorporating a predictive model that can forecast the orientation of a given animal in the near future. Temporal sequence prediction models, such as recurrent neural networks (RNNs)[120], [121], may be used for this purpose and are currently being investigated. The potential applications also involve quantitative analysis of complex animal behaviors, such as their social interactions.

Future studies may take advantage of these enabled wireless optoelectronic features to chronically activate neural circuits for days, weeks, or even months. Because adaptations can occur with sustained activation of a neural pathway, such experiments are important for investigating the persistence of long-term physiological effects, including weight loss. This can enable experiments that determine whether appetite suppression induced by gastric vagal afferent activation is attenuated in obese mice and

whether chronic activation of vagal afferent endings in the stomach can reverse obesity. Identification of viscerosensory pathways that can either suppress or stimulate appetite will have direct clinical importance for potentially developing novel therapeutic targets for treating appetite disorders.

## REFERENCES

- [1] K. Deisseroth, G. Feng, A. K. Majewska, G. Miesenböck, A. Ting, and M. J. Schnitzer, “Next-generation optical technologies for illuminating genetically targeted brain circuits,” *J. Neurosci.*, vol. 26, no. 41, pp. 10380–10386, 2006, doi: 10.1523/JNEUROSCI.3863-06.2006.
- [2] M. Scanziani and M. Häusser, “Electrophysiology in the age of light,” *Nature*, vol. 461, no. 7266, pp. 930–939, 2009, doi: 10.1038/nature08540.
- [3] O. Yizhar, L. E. Fenno, T. J. Davidson, M. Mogri, and K. Deisseroth, “Optogenetics in Neural Systems,” *Neuron*, vol. 71, no. 1, pp. 9–34, 2011, doi: 10.1016/j.neuron.2011.06.004.
- [4] K. Deisseroth, “Optogenetics: 10 years of microbial opsins in neuroscience,” *Nat. Neurosci.*, vol. 18, no. 9, pp. 1213–1225, 2015, doi: 10.1038/nn.4091.
- [5] L. Fenno, O. Yizhar, and K. Deisseroth, “The Development and Application of Optogenetics,” *Annu. Rev. Neurosci.*, vol. 34, no. 1, pp. 389–412, 2011, doi: 10.1146/annurev-neuro-061010-113817.
- [6] F. H. Crick, “Thinking about the brain.,” *Sci. Am.*, vol. 241, no. 3, pp. 219–232, 1979, doi: 10.1038/scientificamerican0979-219.
- [7] A. Matsuno-Yagi and Y. Mukohata, “Two possible roles of bacteriorhodopsin; a comparative study of strains of *Halobacterium halobium* differing in pigmentation,” *Biochem. Biophys. Res. Commun.*, vol. 78, no. 1, pp. 237–243, Sep. 1977, doi: 10.1016/0006-291X(77)91245-1.

- [8] G. Nagel *et al.*, “Channelrhodopsin-1: A light-gated proton channel in green algae,” *Science (80-. )*, vol. 296, no. 5577, pp. 2395–2398, 2002, doi: 10.1126/science.1072068.
- [9] B. Schobert and J. K. Lanyi, “Halorhodopsin is a light-driven chloride pump,” *J. Biol. Chem.*, vol. 257, no. 17, pp. 10306–10313, 1982, doi: 10.1016/s0021-9258(18)34020-1.
- [10] J. K. Lanyi and D. Oesterhelt, “Identification of the retinal-binding protein in halorhodopsin,” *J. Biol. Chem.*, vol. 257, no. 5, pp. 2674–2677, 1982, doi: 10.1016/s0021-9258(18)34976-7.
- [11] O. Beja *et al.*, “Bacterial rhodopsin: Evidence for a new type of phototrophy in the sea,” *Science (80-. )*, vol. 289, no. 5486, pp. 1902–1906, 2000, doi: 10.1126/science.289.5486.1902.
- [12] G. Nagel *et al.*, “Cation-Selective Membrane Channel,” *Pnas*, vol. 100, no. 24, pp. 13940–13945, 2003.
- [13] E. Ritter, K. Stehfest, A. Berndt, P. Hegemann, and F. J. Bartl, “Monitoring light-induced structural changes of channelrhodopsin-2 by UV-visible and Fourier transform infrared spectroscopy,” *J. Biol. Chem.*, vol. 283, no. 50, pp. 35033–35041, 2008, doi: 10.1074/jbc.M806353200.
- [14] F. Zhang *et al.*, “Red-shifted optogenetic excitation: A tool for fast neural control derived from *Volvox carteri*,” *Nat. Neurosci.*, vol. 11, no. 6, pp. 631–633, 2008, doi: 10.1038/nn.2120.
- [15] E. S. Boyden, F. Zhang, E. Bamberg, G. Nagel, and K. Deisseroth, “Millisecond-

- timescale, genetically targeted optical control of neural activity,” *Nat. Neurosci.*, vol. 8, no. 9, pp. 1263–1268, 2005, doi: 10.1038/nn1525.
- [16] X. Li *et al.*, “Fast noninvasive activation and inhibition of neural and network activity by vertebrate rhodopsin and green algae channelrhodopsin,” *Proc. Natl. Acad. Sci. U. S. A.*, vol. 102, no. 49, pp. 17816–17821, 2005, doi: 10.1073/pnas.0509030102.
- [17] G. Nagel, M. Brauner, J. F. Liewald, N. Adeishvili, E. Bamberg, and A. Gottschalk, “Light activation of Channelrhodopsin-2 in excitable cells of *Caenorhabditis elegans* triggers rapid behavioral responses,” *Curr. Biol.*, vol. 15, no. 24, pp. 2279–2284, 2005, doi: 10.1016/j.cub.2005.11.032.
- [18] A. Bi *et al.*, “Ectopic Expression of a Microbial-Type Rhodopsin Restores Visual Responses in Mice with Photoreceptor Degeneration,” *Neuron*, vol. 50, no. 1, pp. 23–33, 2006, doi: 10.1016/j.neuron.2006.02.026.
- [19] T. Ishizuka, M. Kakuda, R. Araki, and H. Yawo, “Kinetic evaluation of photosensitivity in genetically engineered neurons expressing green algae light-gated channels,” *Neurosci. Res.*, vol. 54, no. 2, pp. 85–94, 2006, doi: 10.1016/j.neures.2005.10.009.
- [20] F. Zhang, L. P. Wang, E. S. Boyden, and K. Deisseroth, “Channelrhodopsin-2 and optical control of excitable cells,” *Nat. Methods*, vol. 3, no. 10, pp. 785–792, 2006, doi: 10.1038/nmeth936.
- [21] A. D. Douglass, S. Kraves, K. Deisseroth, A. F. Schier, and F. Engert, “Escape Behavior Elicited by Single, Channelrhodopsin-2-Evoked Spikes in Zebrafish



- Somatosensory Neurons,” *Curr. Biol.*, vol. 18, no. 15, pp. 1133–1137, 2008, doi: 10.1016/j.cub.2008.06.077.
- [22] A. R. Adamantidis, F. Zhang, A. M. Aravanis, K. Deisseroth, and L. De Lecea, “Neural substrates of awakening probed with optogenetic control of hypocretin neurons,” *Nature*, vol. 450, no. 7168, pp. 420–424, 2007, doi: 10.1038/nature06310.
- [23] W. Tan, W. A. Janczewski, P. Yang, X. M. Shao, E. M. Callaway, and J. L. Feldman, “Silencing preBötzinger Complex somatostatin-expressing neurons induces persistent apnea in awake rat,” *Nat. Neurosci.*, vol. 11, no. 5, pp. 538–540, 2008, doi: 10.1038/nn.2104.
- [24] K. Benzekhroufa, B. Liu, F. Tang, A. G. Teschemacher, and S. Kasparov, “Adenoviral vectors for highly selective gene expression in central serotonergic neurons reveal quantal characteristics of serotonin release in the rat brain,” *BMC Biotechnol.*, vol. 9, pp. 1–11, 2009, doi: 10.1186/1472-6750-9-23.
- [25] K. Benzekhroufa, B. H. Liu, A. G. Teschemacher, and S. Kasparov, “Targeting central serotonergic neurons with lentiviral vectors based on a transcriptional amplification strategy,” *Gene Ther.*, vol. 16, no. 5, pp. 681–688, 2009, doi: 10.1038/gt.2009.7.
- [26] W. Tan, S. Pagliardini, P. Yang, W. A. Janczewski, and J. L. Feldman, “Projections of prebötzinger complex neurons in adult rats,” *J. Comp. Neurol.*, vol. 518, no. 10, pp. 1862–1878, 2010, doi: 10.1002/cne.22308.
- [27] M. T. C. Brown *et al.*, “Drug-driven AMPA receptor redistribution mimicked by

- selective dopamine neuron stimulation,” *PLoS One*, vol. 5, no. 12, 2010, doi: 10.1371/journal.pone.0015870.
- [28] G. D. Stuber, T. S. Hnasko, J. P. Britt, R. H. Edwards, and A. Bonci, “Dopaminergic terminals in the nucleus accumbens but not the dorsal striatum corelease glutamate,” *J. Neurosci.*, vol. 30, no. 24, pp. 8229–8233, 2010, doi: 10.1523/JNEUROSCI.1754-10.2010.
- [29] J. P. Rickgauer and D. W. Tank, “Two-photon excitation of channelrhodopsin-2 at saturation,” *Proc. Natl. Acad. Sci.*, vol. 106, no. 35, pp. 15025–15030, Sep. 2009, doi: 10.1073/pnas.0907084106.
- [30] E. Papagiakoumou *et al.*, “Scanless two-photon excitation of channelrhodopsin-2,” *Nat. Methods*, vol. 7, no. 10, pp. 848–854, Oct. 2010, doi: 10.1038/nmeth.1505.
- [31] A. M. Aravanis *et al.*, “An optical neural interface: in vivo control of rodent motor cortex with integrated fiberoptic and optogenetic technology.,” *J. Neural Eng.*, vol. 4, no. 3, 2007, doi: 10.1088/1741-2560/4/3/S02.
- [32] F. Zhang *et al.*, “Optogenetic interrogation of neural circuits: Technology for probing mammalian brain structures,” *Nat. Protoc.*, vol. 5, no. 3, pp. 439–456, 2010, doi: 10.1038/nprot.2009.226.
- [33] S. M. Iyer *et al.*, “Virally mediated optogenetic excitation and inhibition of pain in freely moving nontransgenic mice,” *Nat. Biotechnol.*, vol. 32, no. 3, pp. 274–278, 2014, doi: 10.1038/nbt.2834.
- [34] K. Deisseroth, “Optogenetics,” *Nat. Methods*, vol. 8, no. 1, pp. 26–29, 2011, doi:

- 10.1038/nmeth.f.324.
- [35] A. M. Leifer, C. Fang-Yen, M. Gershow, M. J. Alkema, and A. D. T. Samuel, “Optogenetic manipulation of neural activity in freely moving *Caenorhabditis elegans*,” *Nat. Methods*, vol. 8, no. 2, pp. 147–152, 2011, doi: 10.1038/nmeth.1554.
- [36] J. N. Stirman *et al.*, “Real-time multimodal optical control of neurons and muscles in freely behaving *Caenorhabditis elegans*,” *Nat. Methods*, vol. 8, no. 2, pp. 153–158, 2011, doi: 10.1038/nmeth.1555.
- [37] A. Berndt, O. Yizhar, L. A. Gunaydin, P. Hegemann, and K. Deisseroth, “Bi-stable neural state switches,” *Nat. Neurosci.*, vol. 12, no. 2, pp. 229–234, 2009, doi: 10.1038/nn.2247.
- [38] O. Yizhar *et al.*, “Neocortical excitation/inhibition balance in information processing and social dysfunction,” *Nature*, vol. 477, no. 7363, pp. 171–178, 2011, doi: 10.1038/nature10360.
- [39] T. D. Y. Kozai *et al.*, “microelectrodes with bioactive surfaces for chronic neural interfaces,” *Nat. Mater.*, vol. 11, no. December, pp. 1065–1073, 2012, doi: 10.1038/nmat3468.
- [40] D. R. Sparta, A. M. Stamatakis, J. L. Phillips, N. Hovelsø, R. Van Zessen, and G. D. Stuber, “Construction of implantable optical fibers for long-term optogenetic manipulation of neural circuits,” *Nat. Protoc.*, vol. 7, no. 1, pp. 12–23, 2012, doi: 10.1038/nprot.2011.413.
- [41] J. W. Jeong *et al.*, “Wireless Optofluidic Systems for Programmable In Vivo

- Pharmacology and Optogenetics,” *Cell*, vol. 162, no. 3, pp. 662–674, 2015, doi: 10.1016/j.cell.2015.06.058.
- [42] J. G. McCall *et al.*, “Fabrication and application of flexible, multimodal light-emitting devices for wireless optogenetics,” *Nat. Protoc.*, vol. 8, no. 12, pp. 2413–2428, 2013, doi: 10.1038/nprot.2013.158.
- [43] S. Park *et al.*, “Ultraminiaturized photovoltaic and radio frequency powered optoelectronic systems for wireless optogenetics,” *J. Neural Eng.*, vol. 12, no. 5, p. 056002, Oct. 2015, doi: 10.1088/1741-2560/12/5/056002.
- [44] S. T. Lee, P. A. Williams, C. E. Braine, D. Lin, S. W. M. John, and P. P. Irazoqui, “A Miniature, Fiber-Coupled, Wireless, Deep-Brain Optogenetic Stimulator,” *IEEE Trans. Neural Syst. Rehabil. Eng.*, vol. 23, no. 4, pp. 655–664, Jul. 2015, doi: 10.1109/TNSRE.2015.2391282.
- [45] Y. Iwai, S. Honda, H. Ozeki, M. Hashimoto, and H. Hirase, “A simple head-mountable LED device for chronic stimulation of optogenetic molecules in freely moving mice,” *Neurosci. Res.*, vol. 70, no. 1, pp. 124–127, 2011, doi: 10.1016/j.neures.2011.01.007.
- [46] M. Hashimoto, A. Hata, T. Miyata, and H. Hirase, “Programmable wireless light-emitting diode stimulator for chronic stimulation of optogenetic molecules in freely moving mice,” *Neurophotonics*, vol. 1, no. 01, p. 1, 2014, doi: 10.1117/1.nph.1.1.011002.
- [47] T. Il Kim *et al.*, “Injectable, cellular-scale optoelectronics with applications for wireless optogenetics,” *Science (80-. )*, vol. 340, no. 6129, pp. 211–216, 2013,

doi: 10.1126/science.1232437.

- [48] S. Park *et al.*, “Soft, stretchable, fully implantable miniaturized optoelectronic systems for wireless optogenetics,” *Nat. Biotechnol.*, vol. 33, no. 12, pp. 1280–1286, 2015, doi: 10.1038/nbt.3415.
- [49] K. L. Montgomery *et al.*, “Wirelessly powered, fully internal optogenetics for brain, spinal and peripheral circuits in mice,” *Nat. Methods*, vol. 12, no. 10, pp. 969–974, 2015, doi: 10.1038/nmeth.3536.
- [50] H.-R. Berthoud and W. L. Neuhuber, “Functional and chemical anatomy of the afferent vagal system,” *Auton. Neurosci.*, vol. 85, no. 1, pp. 1–17, 2000, doi: [https://doi.org/10.1016/S1566-0702\(00\)00215-0](https://doi.org/10.1016/S1566-0702(00)00215-0).
- [51] R. B. Chang, D. E. Strohlic, E. K. Williams, B. D. Umans, and S. D. Liberles, “Vagal sensory neuron subtypes that differentially control breathing,” *Cell*, vol. 161, no. 3, pp. 622–633, 2015, doi: 10.1016/j.cell.2015.03.022.
- [52] E. K. Williams, R. B. Chang, D. E. Strohlic, B. D. Umans, B. B. Lowell, and S. D. Liberles, “Sensory Neurons that Detect Stretch and Nutrients in the Digestive System,” *Cell*, vol. 166, no. 1, pp. 209–221, 2016, doi: 10.1016/j.cell.2016.05.011.
- [53] G. de Lartigue, “Role of the vagus nerve in the development and treatment of diet-induced obesity,” *J. Physiol.*, vol. 594, no. 20, pp. 5791–5815, 2016, doi: 10.1113/JP271538.
- [54] G. J. Schwartz, “The role of gastrointestinal vagal afferents in the control of food intake: Current prospects,” *Nutrition*, vol. 16, no. 10, pp. 866–873, 2000, doi:

10.1016/S0899-9007(00)00464-0.

- [55] A. D. Mickle *et al.*, “A wireless closed-loop system for optogenetic peripheral neuromodulation,” *Nature*, vol. 565, no. 7739, pp. 361–365, 2019, doi: 10.1038/s41586-018-0823-6.
- [56] P. Gutruf *et al.*, “Wireless, battery-free, fully implantable multimodal and multisite pacemakers for applications in small animal models,” *Nat. Commun.*, vol. 10, no. 1, 2019, doi: 10.1038/s41467-019-13637-w.
- [57] T. J. Hibberd *et al.*, “Optogenetic Induction of Colonic Motility in Mice,” *Gastroenterology*, vol. 155, no. 2, pp. 514-528.e6, 2018, doi: 10.1053/j.gastro.2018.05.029.
- [58] Atmel, *8-bit Microcontroller with 2K/4K/8K Bytes In-System Programmable Flash*. 2012.
- [59] N. Semiconductors, *Kinetis KL03 32 KB Flash 48 MHz Cortex-M0+ Based Microcontroller*. 2017.
- [60] STMicroelectronics, *M24LR16E-R Dynamic NFC / RFID tag IC with 16-Kbit EEPROM*, vol. 8, no. June. 2013.
- [61] Nordic Semiconductor, *RFDUINO - nRF51822 Datasheet*, no. 3. 2014.
- [62] W. H. Bailey *et al.*, *Synopsis of IEEE Std C95.1<sup>TM</sup>-2019 IEEE Standard for Safety Levels With Respect to Human Exposure to Electric, Magnetic, and Electromagnetic Fields, 0 Hz to 300 GHz*, vol. 7. 2019.
- [63] S. Kodera and A. Hirata, “Comparison of thermal response for RF exposure in human and rat models,” *Int. J. Environ. Res. Public Health*, vol. 15, no. 10, 2018,

doi: 10.3390/ijerph15102320.

- [64] A. Ueno, R. Lazaro, P. Y. Wang, R. Higashiyama, K. MacHida, and H. Tsukamoto, “Mouse intragastric infusion (iG) model,” *Nat. Protoc.*, vol. 7, no. 4, pp. 771–781, 2012, doi: 10.1038/nprot.2012.014.
- [65] W. I. Li, C. L. Chen, and J. Y. Chou, “Characterization of a temperature-sensitive  $\beta$ -endorphin-secreting transformed endometrial cell line,” *Endocrinology*, vol. 125, no. 6, pp. 2862–2867, 1989, doi: 10.1210/endo-125-6-2862.
- [66] P. Gutruf *et al.*, “Fully implantable optoelectronic systems for battery-free, multimodal operation in neuroscience research,” *Nat. Electron.*, vol. 1, no. 12, pp. 652–660, 2018, doi: 10.1038/s41928-018-0175-0.
- [67] W. S. Kim, S. Hong, C. Morgan, P. Nakaji, M. T. Lawton, and S. Park, “A soft, biocompatible magnetic field enabled wireless surgical lighting patty for neurosurgery,” *Appl. Sci.*, vol. 10, no. 6, 2020, doi: 10.3390/app10062001.
- [68] W. S. Kim, M. Jeong, S. Hong, B. Lim, and S. Park, “Fully implantable low-power high frequency range optoelectronic devices for dual-channel modulation in the brain,” *Sensors (Switzerland)*, vol. 20, no. 13, pp. 1–14, 2020, doi: 10.3390/s20133639.
- [69] H. Zhang *et al.*, “Wireless, battery-free optoelectronic systems as subdermal implants for local tissue oximetry,” *Sci. Adv.*, vol. 5, no. 3, 2019, doi: 10.1126/sciadv.aaw0873.
- [70] C. Martin and W. Sun, “Fatigue damage of collagenous tissues: experiment, modeling and simulation studies.,” *J. Long. Term. Eff. Med. Implants*, vol. 25, no.

- 1–2, pp. 55–73, Jul. 2015, doi: 10.1615/jlongtermeffmedimplants.2015011749.
- [71] J. Kim *et al.*, “Epidermal electronics with advanced capabilities in near-field communication,” *Small*, vol. 11, no. 8, pp. 906–912, 2015, doi: 10.1002/sml.201402495.
- [72] J. Kim *et al.*, “Miniaturized Flexible Electronic Systems with Wireless Power and Near-Field Communication Capabilities,” *Adv. Funct. Mater.*, vol. 25, no. 30, pp. 4761–4767, 2015, doi: 10.1002/adfm.201501590.
- [73] R. R. Harrison *et al.*, “Low-Power Integrated Circuit,” vol. 17, no. 4, pp. 322–329, 2009.
- [74] M. A. Hannan, S. Mutashar, S. A. Samad, and A. Hussain, “Energy harvesting for the implantable biomedical devices: Issues and challenges,” *Biomed. Eng. Online*, vol. 13, no. 1, pp. 1–23, 2014, doi: 10.1186/1475-925X-13-79.
- [75] G. Shin *et al.*, “Flexible Near-Field Wireless Optoelectronics as Subdermal Implants for Broad Applications in Optogenetics,” *Neuron*, vol. 93, no. 3, pp. 509–521.e3, 2017, doi: 10.1016/j.neuron.2016.12.031.
- [76] J. Thaysen, “Mutual coupling between identical planar inverted-F antennas,” *IEEE Antennas Propag. Soc. Int. Symp. (IEEE Cat. No.02CH37313)*, vol. 4, pp. 504–507, 2002, doi: 10.1016/j.aeu.2006.09.004.
- [77] L. Giancardo *et al.*, “Automatic Visual Tracking and Social Behaviour Analysis with Multiple Mice,” *PLoS One*, vol. 8, no. 9, 2013, doi: 10.1371/journal.pone.0074557.
- [78] A. D. Steele, W. S. Jackson, O. D. King, and S. Lindquist, “The power of



- automated high-resolution behavior analysis revealed by its application to mouse models of Huntington’s and prion diseases,” *Proc. Natl. Acad. Sci. U. S. A.*, vol. 104, no. 6, pp. 1983–1988, 2007, doi: 10.1073/pnas.0610779104.
- [79] Y. Poleg, A. Ephrat, S. Peleg, and C. Arora, “Compact CNN for indexing egocentric videos,” *2016 IEEE Winter Conf. Appl. Comput. Vision, WACV 2016*, pp. 1–9, 2016, doi: 10.1109/WACV.2016.7477708.
- [80] Z. Liang *et al.*, “CNN-based image analysis for malaria diagnosis,” *Proc. - 2016 IEEE Int. Conf. Bioinforma. Biomed. BIBM 2016*, pp. 493–496, 2017, doi: 10.1109/BIBM.2016.7822567.
- [81] A. Arac, P. Zhao, B. H. Dobkin, S. T. Carmichael, and P. Golshani, “Deepbehavior: A deep learning toolbox for automated analysis of animal and human behavior imaging data,” *Front. Syst. Neurosci.*, vol. 13, no. May, pp. 1–12, 2019, doi: 10.3389/fnsys.2019.00020.
- [82] M. Danielczuk *et al.*, “Segmenting unknown 3D objects from real depth images using mask R-CNN trained on synthetic data,” *Proc. - IEEE Int. Conf. Robot. Autom.*, vol. 2019-May, pp. 7283–7290, 2019, doi: 10.1109/ICRA.2019.8793744.
- [83] L. C. Chen, G. Papandreou, I. Kokkinos, K. Murphy, and A. L. Yuille, “DeepLab: Semantic Image Segmentation with Deep Convolutional Nets, Atrous Convolution, and Fully Connected CRFs,” *IEEE Trans. Pattern Anal. Mach. Intell.*, vol. 40, no. 4, pp. 834–848, 2018, doi: 10.1109/TPAMI.2017.2699184.
- [84] F. Xia, P. Wang, X. Chen, and A. Yuille, “Joint Multi-Person Pose Estimation and Semantic Part Segmentation,” *Cvpr*, pp. 6769–6778, 2017.

- [85] A. Mathis *et al.*, “DeepLabCut: markerless pose estimation of user-defined body parts with deep learning,” *Nat. Neurosci.*, vol. 21, no. 9, pp. 1281–1289, 2018, doi: 10.1038/s41593-018-0209-y.
- [86] parkgroup-tamu, “parkgroup-tamu/3d\_reconstruction: First release of 3d\_reconstruction.” Zenodo, Nov-2020, doi: 10.5281/zenodo.4247753.
- [87] A. Kurs, A. Karalis, R. Moffatt, J. D. Joannopoulos, P. Fisher, and M. Soljačić, “Wireless power transfer via strongly coupled magnetic resonances,” *Science (80-. )*, vol. 317, no. 5834, pp. 83–86, 2007, doi: 10.1126/science.1143254.
- [88] P. Varaldo, *Exposure to high frequency electromagnetic fields, biological effects and health consequences (100 kHz-300 GHz)*. 2009.
- [89] Z. Zhang, Q. Shi, J. McAuley, W. Wei, Y. Zhang, and A. van den Hengel, “Pairwise Matching through Max-Weight Bipartite Belief Propagation,” in *2016 IEEE Conference on Computer Vision and Pattern Recognition (CVPR)*, 2016, vol. 2016-Decem, pp. 1202–1210, doi: 10.1109/CVPR.2016.135.
- [90] R. G. Congalton, “A review of assessing the accuracy of classifications of remotely sensed data,” *Remote Sens. Environ.*, vol. 37, no. 1, pp. 35–46, Jul. 1991, doi: 10.1016/0034-4257(91)90048-B.
- [91] S. Gabriel, R. W. Lau, and C. Gabriel, “The dielectric properties of biological tissues: II. Measurements in the frequency range 10 Hz to 20 GHz,” *Phys. Med. Biol.*, vol. 41, no. 11, pp. 2251–2269, 1996, doi: 10.1088/0031-9155/41/11/002.
- [92] S. Park, “Enhancement of wireless power transmission into biological tissues using a high surface impedance ground plane,” *Prog. Electromagn. Res.*, vol. 135,

- no. November 2012, pp. 123–136, 2013, doi: 10.2528/PIER12110902.
- [93] B. W. Flynn and K. Fotopoulou, “Rectifying loose coils,” *IEEE Microw. Mag.*, no. Mar./Apr., pp. 48–54, 2013.
- [94] O. Jonah, S. V. Georgakopoulos, and M. M. Tentzeris, “Orientation insensitive power transfer by magnetic resonance for mobile devices,” *2013 IEEE Wirel. Power Transf. WPT 2013*, pp. 5–8, 2013, doi: 10.1109/WPT.2013.6556868.
- [95] D. Liu, H. Hu, and S. V. Georgakopoulos, “Misalignment sensitivity of strongly coupled wireless power transfer systems,” *IEEE Trans. Power Electron.*, vol. 32, no. 7, pp. 5509–5519, 2017, doi: 10.1109/TPEL.2016.2605698.
- [96] A. K. RamRakhyani, S. Mirabbasi, and M. Chiao, “Design and optimization of resonance-based efficient wireless power delivery systems for biomedical implants,” *IEEE Trans. Biomed. Circuits Syst.*, vol. 5, no. 1, pp. 48–63, 2011, doi: 10.1109/TBCAS.2010.2072782.
- [97] Z. Cheng, T. L. Powley, J. S. Schwaber, and F. J. Doyle, “Vagal afferent innervation of the atria of the rat heart reconstructed with confocal microscopy,” *J. Comp. Neurol.*, vol. 381, no. 1, pp. 1–17, 1997, doi: 10.1002/(SICI)1096-9861(19970428)381:1<1::AID-CNE1>3.0.CO;2-5.
- [98] S. B. Mazzone and B. J. Udem, “Vagal afferent innervation of the airways in health and disease,” *Physiol. Rev.*, vol. 96, no. 3, pp. 975–1024, 2016, doi: 10.1152/physrev.00039.2015.
- [99] H. -R Berthoud and T. L. Powley, “Vagal afferent innervation of the rat fundic stomach: Morphological characterization of the gastric tension receptor,” *J.*

- Comp. Neurol.*, vol. 319, no. 2, pp. 261–276, 1992, doi: 10.1002/cne.903190206.
- [100] H. J. Grill and M. R. Hayes, “Hindbrain neurons as an essential hub in the neuroanatomically distributed control of energy balance,” *Cell Metab.*, vol. 16, no. 3, pp. 296–309, 2012, doi: 10.1016/j.cmet.2012.06.015.
- [101] G. J. Morton, T. H. Meek, and M. W. Schwartz, “Neurobiology of food intake in health and disease,” *Nat. Rev. Neurosci.*, vol. 15, no. 6, pp. 367–378, 2014, doi: 10.1038/nrn3745.
- [102] C. W. Roman, V. A. Derkach, and R. D. Palmiter, “Genetically and functionally defined NTS to PBN brain circuits mediating anorexia,” *Nat. Commun.*, vol. 7, no. May, pp. 1–11, 2016, doi: 10.1038/ncomms11905.
- [103] C. A. Campos, A. J. Bowen, M. W. Schwartz, and R. D. Palmiter, “Parabrachial CGRP Neurons Control Meal Termination,” *Cell Metab.*, vol. 23, no. 5, pp. 811–820, 2016, doi: 10.1016/j.cmet.2016.04.006.
- [104] Q. Wu, M. P. Boyle, and R. D. Palmiter, “Loss of GABAergic Signaling by AgRP Neurons to the Parabrachial Nucleus Leads to Starvation,” *Cell*, vol. 137, no. 7, pp. 1225–1234, 2009, doi: 10.1016/j.cell.2009.04.022.
- [105] K. Birmingham *et al.*, “Bioelectronic medicines: A research roadmap,” *Nat. Rev. Drug Discov.*, vol. 13, no. 6, pp. 399–400, 2014, doi: 10.1038/nrd4351.
- [106] T. H. Moran, A. R. Baldessarini, C. F. Salorio, T. Lowery, and G. J. Schwartz, “Vagal afferent and efferent contributions to the inhibition of food intake by cholecystokinin,” *Am. J. Physiol.*, vol. 272, no. 4 PART 2, 1997, doi: 10.1152/ajpregu.1997.272.4.r1245.

- [107] L. Bai *et al.*, “Genetic Identification of Vagal Sensory Neurons That Control Feeding,” *Cell*, vol. 179, no. 5, pp. 1129–1143.e23, 2019, doi: 10.1016/j.cell.2019.10.031.
- [108] J. Y. Lin, “A User’s Guide to Channelrhodopsin Variants,” *Exp. Physiol.*, vol. 96, no. 1, pp. 19–25, 2012, doi: 10.1113/expphysiol.2009.051961.A.
- [109] F. Reimann, G. Tolhurst, and F. M. Gribble, “G-protein-coupled receptors in intestinal chemosensation,” *Cell Metab.*, vol. 15, no. 4, pp. 421–431, 2012, doi: 10.1016/j.cmet.2011.12.019.
- [110] X. Luo, R. Hu, S. Liu, and K. Wang, “Heat and fluid flow in high-power LED packaging and applications,” *Prog. Energy Combust. Sci.*, vol. 56, pp. 1–32, 2016, doi: 10.1016/j.pecs.2016.05.003.
- [111] A. J. Welch, “The Thermal Response of Laser Irradiated Tissue,” *IEEE J. Quantum Electron.*, vol. 20, no. 12, pp. 1471–1481, 1984, doi: 10.1109/JQE.1984.1072339.
- [112] J. N. Betley *et al.*, “Neurons for hunger and thirst transmit a negative-valence teaching signal,” *Nature*, vol. 521, no. 7551, pp. 180–185, 2015, doi: 10.1038/nature14416.
- [113] M. E. Carter, S. Han, and R. D. Palmiter, “Parabrachial calcitonin gene-related peptide neurons mediate conditioned taste aversion,” *J. Neurosci.*, vol. 35, no. 11, pp. 4582–4586, 2015, doi: 10.1523/JNEUROSCI.3729-14.2015.
- [114] J. Paues, L. Mackerlova, and A. Blomqvist, “Expression of melanocortin-4 receptor by rat parabrachial neurons responsive to immune and aversive stimuli,”

- Neuroscience*, vol. 141, no. 1, pp. 287–297, 2006, doi:  
10.1016/j.neuroscience.2006.03.041.
- [115] J. Lin, J. Arthurs, and S. Reilly, “Conditioned taste aversions: From poisons to pain to drugs of abuse,” *Psychon. Bull. Rev.*, vol. 24, no. 2, pp. 335–351, Apr. 2017, doi: 10.3758/s13423-016-1092-8.
- [116] S. Park *et al.*, “Stretchable multichannel antennas in soft wireless optoelectronic implants for optogenetics,” *Proc. Natl. Acad. Sci.*, vol. 113, no. 50, pp. E8169–E8177, Dec. 2016, doi: 10.1073/pnas.1611769113.
- [117] Q. Wu, M. S. Clark, and R. D. Palmiter, “Deciphering a neuronal circuit that mediates appetite,” *Nature*, vol. 483, no. 7391, pp. 594–597, 2012, doi: 10.1038/nature10899.
- [118] H. D. Critchley and N. A. Harrison, “Visceral Influences on Brain and Behavior,” *Neuron*, vol. 77, no. 4, pp. 624–638, 2013, doi: 10.1016/j.neuron.2013.02.008.
- [119] I. M. Chiu, C. A. Von Hehn, and C. J. Woolf, “Neurogenic inflammation and the peripheral nervous system in host defense and immunopathology,” *Nat. Neurosci.*, vol. 15, no. 8, pp. 1063–1067, 2012, doi: 10.1038/nn.3144.
- [120] J. Martinez, M. J. Black, and J. Romero, “On Human Motion Prediction Using Recurrent Neural Networks,” in *2017 IEEE Conference on Computer Vision and Pattern Recognition (CVPR)*, 2017, pp. 4674–4683, doi: 10.1109/CVPR.2017.497.
- [121] B. Kim, C. M. Kang, J. Kim, S. H. Lee, C. C. Chung, and J. W. Choi, “Probabilistic vehicle trajectory prediction over occupancy grid map via recurrent

neural network,” in *2017 IEEE 20th International Conference on Intelligent Transportation Systems (ITSC)*, 2017, pp. 399–404, doi:  
10.1109/ITSC.2017.8317943.

## APPENDIX A

### THE CODE AND DATA SAMPLES FOR 3D RECONSTRUCTION IMAGE

#### 1. System Requirements

- Python 3.7.0 or higher
- OpenCV-4.1.1 or higher
- Any Python IDE and OS is available.
- This package has been developed the following IDE, OS and CPU: Spyder(Anaconda 3) at Windows 10 with Intel(R)\_Core(TM)i7-7500U\_CPU@\_2.70GHz.
- This package has been tested the following IDE, OS and CPU: Spyder(Anaconda 3) at Windows 10 with Intel(R)\_Core(TM)i7-4770K\_CPU@\_3.50GHz

#### 2. Installation Guide

- Users should download all video files in two folders\*:  
[01\_Antenna\_comparison\_figure2\_data] and  
[02\_3D\_View\_supplimentary\_figure10\_data]
- Users should download all codes in the same folder.
- Users should install OpenCV before running codes: pip install opencv.
- Each step normally takes within 2 minutes but downloading time might be slow depends on network condition.

\* Videos are available from Github ([https://github.com/%20parkgroup-tamu/3d\\_reconstruction](https://github.com/%20parkgroup-tamu/3d_reconstruction))

#### 3. Demo Instructions

- This project includes sample videos and codes that can generate figures and several processed data files with csv format.
- [01\_Antenna\_comparison\_figure2\_data] includes 4 video files which are source data for generating a bar graph that represents comparison result of wireless coverage corresponds to different antenna designs.
- [02\_3D\_View\_supplimentary\_figure10\_data] includes 9 video files which are source data for generating 3D reconstructed figures that trace an operating indicator LED and the cross-sectional view of it at each range of height for the three different antenna designs, respectively.

- A. To generate a Antenna comparison figure,
- Open "S0\_ANT\_comparison\_starter.py"



- Edit line 18, path = 'FILE\_PATH\_HERE\\'. FILE\_PATH means path of the folder which includes 4-video files in 01\_Antenna\_comparison\_figure2\_data
- User should insert double back-slashes('\\') when divide into directories.
- Run "S0\_ANT\_comparison\_starter.py" (Expected running time: 2 minutes)
- If this code run correctly, user can find following files in the data folder.
- Ant\_comparison\_plot.png, Ant1\_1W\_top.csv, Ant1\_1W\_rst.csv, Ant2\_1W\_top.csv, Ant2\_1W\_rst.csv, Ant3\_1W\_top.csv, Ant3\_1W\_rst.csv, Ant4\_1W\_top.csv, Ant4\_1W\_rst.csv

B. To generate 3D reconstruction figures,

- Open "S0\_3D\_View\_starter.py"
- Edit line 18, path = 'FILE\_PATH\_HERE\\'. FILE\_PATH means path of the folder which includes 9-video files in 02\_3D\_View\_supplimentary\_figure10\_data
- User should insert double back-slashes('\\') when divide into directories.
- Run "S0\_3D\_View\_starter.py" (Expected running time: 5 minutes)
- If this code run correctly, user can find following files in the data folder:  
a\_rst\_3d.png, a\_rst\_xy\_1layer.png, a\_rst\_xy\_2layer.png, a\_rst\_xy\_3layer.png, a\_rst\_xy\_4layer.png, a\_rst.csv, a\_top.csv, a\_side\_i.csv, a\_side\_w.csv  
b\_rst\_3d.png, b\_rst\_xy\_1layer.png, b\_rst\_xy\_2layer.png, b\_rst\_xy\_3layer.png, b\_rst\_xy\_4layer.png, b\_rst.csv, b\_top.csv, b\_side\_i.csv, b\_side\_w.csv  
c\_rst\_3d.png, c\_rst\_xy\_1layer.png, c\_rst\_xy\_2layer.png, c\_rst\_xy\_3layer.png, c\_rst\_xy\_4layer.png, c\_rst.csv, c\_top.csv, c\_side\_i.csv, c\_side\_w.csv

#### 4. Code

✓ File 1: S0\_3D\_View\_starter.py

```
# -*- coding: utf-8 -*-
"""
```

Created on Tue Jan 7 18:20:47 2020

@input: Nine mp4 video files that are recorded at the top and two sideward angles using three different antenna designs are required.

@output: 1. Four csv files that include x,y,z coordinates and summary of frame numbers from LED(color) detected frame according to each antenna design.

2. A 3D reconstruction image of traces of an operating indicator LED

3. Four xy plane reconstruction images in different height of the cage according to each antenna design.

```
"""
```

```
from S1_extract_xyz_from_video import Extractxyz
from S2_3dview_analysis import ThreeDimensionViewAnalysis
from S3_xy_view_z_analysis import ZaxisAnalysis
```

```
def main():
```

```

# Add folder path that includes nine mp4 videos which can generate supplementary figure 10.
# For example, path=
'C:\\Download\\3d_reconstruction\\02_3D_View_supplimentary_figure10_data\\'
path= 'FILE_PATH_HERE\\'

ifilename = 'a_Proposed_'
ofilename = 'a_'

Extractxyz.launch(path, ifilename + "top.mp4", ofilename + "top", 25, 90)
Extractxyz.launch(path, ifilename + "side_w.mp4", ofilename + "side_w", 25, 90)
Extractxyz.launch(path, ifilename + "side_i.mp4", ofilename + "side_i", 25, 90)

ThreeDimensionViewAnalysis.launch(path, ofilename + "top", ofilename + "side_w", ofilename +
"side_i", ofilename + "rst" )
ZaxisAnalysis.launch(path, ofilename + "rst")

ifilename = 'b_2turn_'
ofilename = 'b_'

Extractxyz.launch(path, ifilename + "top.mp4", ofilename + "top", 25, 90)
Extractxyz.launch(path, ifilename + "side_w.mp4", ofilename + "side_w", 25, 90)
Extractxyz.launch(path, ifilename + "side_i.mp4", ofilename + "side_i", 25, 90)

ThreeDimensionViewAnalysis.launch(path, ofilename + "top", ofilename + "side_w", ofilename +
"side_i", ofilename + "rst" )
ZaxisAnalysis.launch(path, ofilename + "rst")

ifilename = 'c_Singular_'
ofilename = 'c_'

Extractxyz.launch(path, ifilename + "top.mp4", ofilename + "top", 15, 40)
Extractxyz.launch(path, ifilename + "side_w.mp4", ofilename + "side_w", 15, 40)
Extractxyz.launch(path, ifilename + "side_i.mp4", ofilename + "side_i", 15, 40)

ThreeDimensionViewAnalysis.launch(path, ofilename + "top", ofilename + "side_w", ofilename +
"side_i", ofilename + "rst" )
ZaxisAnalysis.launch(path, ofilename + "rst")

if __name__ == "__main__":
    main()

```

✓ File 2: S1\_extract\_xyz\_from\_video.py

```

# -*- coding: utf-8 -*-
"""

```

Created on Mon Dec 9 10:26:01 2019

@author: WSK

@input: A mp4 video file is required.

@output: 1. A csv file which includes x,y,z coordinates and frame number from LED(color) detected  
frame  
"""

```
import numpy as np
import time
import math
import cv2

class Extractxyz:

    def nothing(x):
        #any operation
        pass

    def launch(path, ifilename, ofilename, a, lr):
        cap = cv2.VideoCapture(path + ifilename)
        time.sleep(2.0)

        cv2.namedWindow("Trackbars")
        cv2.createTrackbar("L-B", "Trackbars", 120, 255, Extractxyz.nothing) #90 #normal: 120
        cv2.createTrackbar("L-G", "Trackbars", 120, 255, Extractxyz.nothing) #90 #120
        cv2.createTrackbar("L-R", "Trackbars", lr, 255, Extractxyz.nothing) #150 #90
        cv2.createTrackbar("U-B", "Trackbars", 255, 255, Extractxyz.nothing)
        cv2.createTrackbar("U-G", "Trackbars", 255, 255, Extractxyz.nothing)
        cv2.createTrackbar("U-R", "Trackbars", 255, 255, Extractxyz.nothing)

        font = cv2.FONT_HERSHEY_COMPLEX
        bboxes = []
        areas = []
        frm_num = 0
        frm = []
        centroid_list=[]
        centroid_list.append([0,0,0,0,0])

        while cap.isOpened():
            ret, frame = cap.read()
            # if frame is read correctly ret is True
            if not ret:
                print("Can't receive frame (stream end?). Exiting ...")
                break

            l_b = cv2.getTrackbarPos("L-B", "Trackbars")
            l_g = cv2.getTrackbarPos("L-G", "Trackbars")
            l_r = cv2.getTrackbarPos("L-R", "Trackbars")
            u_b = cv2.getTrackbarPos("U-B", "Trackbars")
            u_g = cv2.getTrackbarPos("U-G", "Trackbars")
            u_r = cv2.getTrackbarPos("U-R", "Trackbars")

            lower = np.array([l_b,l_g,l_r])
            upper = np.array([u_b,u_g,u_r])
```

```

hsv = cv2.cvtColor(frame, cv2.COLOR_BGR2HSV)

mask = cv2.inRange(hsv, lower, upper)
output = cv2.bitwise_and(frame, frame, mask = mask)

cnts, hierarchy = cv2.findContours(mask, cv2.RETR_TREE, cv2.CHAIN_APPROX_SIMPLE)

idx = 0

# initialize an array of input centroids for the current frame
for cnt in cnts:
    area = cv2.contourArea(cnt)

    approx = cv2.approxPolyDP(cnt, 0.01*cv2.arcLength(cnt, True), True)
    x = approx.ravel()[0]
    y = approx.ravel()[1]

    if a < area :
        cv2.drawContours(frame, [approx], 0, (255,255,255), 1)
        rect = cv2.boundingRect(cnt)
        p1 = (int(rect[0]), int(rect[1]))
        p2 = (int(rect[0] + rect[2]), int(rect[1] + rect[3]))
        cv2.rectangle(frame, p1,p2, (255,0,0), 2, 1)

        rotatedRect = cv2.minAreaRect(cnt)
        vertices = cv2.boxPoints(rotatedRect)
        vertices = np.int0(vertices)
        centroidX = math.ceil((vertices[0][0]+vertices[1][0]+vertices[2][0]+vertices[3][0])/4)
        centroidY = math.ceil(
            (vertices[0][1]+vertices[1][1]+vertices[2][1]+vertices[3][1])/4)

        cv2.drawContours(frame,[vertices],0,(0,0,255),1)
        cv2.circle(frame,(centroidX,centroidY), 3, (0,255,0), -1)

        bboxes.append(rect)
        areas.append(area)
        idx = idx + 1
        text = "ID {}".format(area);
        cv2.putText(frame,text,(x,y), font, 1, (255,255,255))
        centroid_list.append([frm_num, centroidX, centroidY, area, 0])

cv2.imshow('frame', np.hstack([frame, output]))
frm.append(frm_num)
frm_num = frm_num + 1

if cv2.waitKey(1) == ord('p'):
    cv2.waitKey(-1)

if cv2.waitKey(10) == ord('q'):
    break

centroid_list[0]=['f','x','y','a','FrmNum']

```

```

if len(centroid_list)==1:
    centroid_list.append([0,0,0,0])
centroid_list[1][4] = frm_num

cap.release()
cv2.destroyAllWindows()

np.savetxt(path + ofilename + ".csv", centroid_list,delimiter=",", fmt='%s')

```

✓ File 3: S2\_3dview\_analysis.py

```

# -*- coding: utf-8 -*-
"""
Created on Mon Dec 9 18:58:04 2019

@author: WSK
@input: Three csv files from different angles (top and two sideways) are required.
        Each file should include information of x,y,z coordinates and number of detected frames.
@output: 1. Figure in 3-D view shows traces of mouse movement(operating indicator LED).
         2. A csv file that includes summary information of recorded data according to each planes.
"""

import matplotlib.pyplot as plt
from mpl_toolkits.mplot3d import Axes3D
import pandas
import numpy as np

class ThreeDimensionViewAnalysis:

    def Sort_fxya(f, x, y, a):

        def Sort(i,cnt):
            tmpA = a[i+cnt]
            result_cnt = cnt
            while(cnt):
                if(tmpA > a[i+cnt-1]):
                    cnt = cnt-1
                else:
                    tmpA = a[i+cnt-1]
                    cnt = cnt-1
            result_cnt = cnt

        return result_cnt

sorted_val = []
cnt = 1
det = 1
fix = 0
i = 0
while (i < len(f)):

```

```

while(det):
    if (i+cnt) == len(f):
        cnt = cnt-1
        det = 0
        break
    else:
        if f[i] == f[i+cnt]:
            cnt = cnt + 1
        else:
            cnt = cnt - 1
            det = 0
if cnt == 0:
    sorted_val.append([f[i], x[i], y[i], a[i]])
else:
    fix = Sort(i, cnt)
    sorted_val.append([f[i+fix], x[i+fix], y[i+fix], a[i+fix]])
det = 1
i = i + cnt + 1
return sorted_val

def launch(path, ifilenamet, ifilenamew, ifilenamei, ofilename):

    # put into the .csv file which is obtained using 'S1_extract_xyz_from_video.py'
    df_top = pandas.read_csv(path + ifilenamet + '.csv') # top view
    df_sidew = pandas.read_csv(path + ifilenamew + '.csv') # side view 1
    df_sidei = pandas.read_csv(path + ifilenamei + '.csv') # side view 2

    top_f = df_top['f']
    top_x = df_top['x']
    top_y = df_top['y']
    top_a = df_top['a']
    top_frmNum = df_top['FrmNum']

    sw_f = df_sidew['f']
    sw_x = df_sidew['x']
    sw_y = df_sidew['y']
    sw_a = df_sidew['a']
    sw_frmNum = df_sidew['FrmNum']

    si_f = df_sidei['f']
    si_x = df_sidei['x']
    si_y = df_sidei['y']
    si_a = df_sidei['a']
    si_frmNum = df_sidei['FrmNum']

    sorted_top = ThreeDimensionViewAnalysis.Sort_fxya(top_f,top_x, top_y, top_a)
    sorted_sidew = ThreeDimensionViewAnalysis.Sort_fxya(sw_f, sw_x, sw_y, sw_a)
    sorted_sidei = ThreeDimensionViewAnalysis.Sort_fxya(si_f, si_x, si_y, si_a)

    merge_side = sorted_sidew + sorted_sidei

```

```

merge_side.sort(key=lambda x: x[0])

sm_f = []
sm_x = []
sm_y = []
sm_a = []

for i in range(len(merge_side)):
    sm_f.append(merge_side[i][0])
    sm_x.append(merge_side[i][1])
    sm_y.append(merge_side[i][2])
    sm_a.append(merge_side[i][3])
sorted_side = ThreeDimensionViewAnalysis.Sort_fxya(sm_f, sm_x, sm_y, sm_a)

idx = 0
for i in range(0, len(sorted_top)):
    for j in range(0, len(sorted_side)):
        if sorted_top[i][0] == sorted_side[j][0]:
            k = i
            l = j
            idx = 1
            break
    if idx == 1:
        break
xy_frmNum = top_frmNum[0] - sorted_top[k][0]
if sw_frmNum[0] > si_frmNum[0] :
    yz_frmNum = sw_frmNum[0]-sorted_side[l][0]
else:
    yz_frmNum = si_frmNum[0]-sorted_side[l][0]

del sorted_top[0:k]
del sorted_side[0:l]

xy_Num = len(sorted_top)
yz_Num = len(sorted_side)

merge_xyz = sorted_top + sorted_side
merge_xyz.sort(key=lambda x: x[0])
m_f = []
m_x = []
m_y = []
m_a = []

for i in range(len(merge_xyz)):
    m_f.append(merge_xyz[i][0])
    m_x.append(merge_xyz[i][1])
    m_y.append(merge_xyz[i][2])
    m_a.append(merge_xyz[i][3])
merge_xyz = ThreeDimensionViewAnalysis.Sort_fxya(m_f, m_x, m_y, m_a)

sorted_xyz = []
x = []

```

```

y = []
z = []

i = 0
for i in range(len(sorted_top)):
    for j in range(len(sorted_side)):
        if sorted_top[i][0] == sorted_side[j][0]:
            sorted_xyz.append([sorted_top[i][0], sorted_top[i][1], sorted_top[i][2], sorted_side[j][2]])
            x.append(sorted_top[i][1])
            y.append(sorted_top[i][2])
            z.append(sorted_side[j][2])
            break

xyz_Num = len(sorted_xyz)

fX = np.array(x)
fY = np.array(y)
fZ = np.array(z)

fxmin = min(fX)
fxmax = max(fX)
fymin = min(fY)
fymax = max(fY)
fzmin = min(fZ)
fzmax = max(fZ)

fig = plt.figure()
ax = plt.axes(projection='3d')
ax.plot3D(fX, fY, fZ, 'red', ls='None', marker='.')
#ax.grid(b=None)
#ax.axis('off')
ax.set_xlim3d(fxmin-50,fxmax+50)
ax.set_ylim3d(fymin-50,fymax+50)
ax.set_zlim3d(fzmin-50,fzmax+50)
fig.savefig(path + ofilename + "_3d.png", transparent=True)

plt.show()

xyz_rst_list=[]

xyz_rst_list.append(['x','y','z','xy_total','yz_total','xy_calculated','yz_calculated','xyz_calculated','xy_or_
yz'])
i=0
for i in range(xyz_Num):
    xyz_rst_list.append([fX[i], fY[i], fZ[i], 0, 0, 0, 0, 0, 0])

xyz_rst_list[1][3] = xy_frmNum
xyz_rst_list[1][4] = yz_frmNum
xyz_rst_list[1][5] = xy_Num
xyz_rst_list[1][6] = yz_Num
xyz_rst_list[1][7] = xyz_Num
xyz_rst_list[1][8] = len(merge_xyz)

```



```
np.savetxt(path + ofilename + ".csv", xyz_rst_list, delimiter=",", fmt='%s')
```

✓ File 4: S3\_xy\_view\_z\_analysis.py

```
# -*- coding: utf-8 -*-  
"""
```

```
Created on Mon Dec 30 09:39:48 2019
```

```
@author: WSK
```

```
@input: A csv file is required. The file should include summary of x,y,z coordinates array  
corresponds to each antenna.
```

```
@output: Figures in x-y view by layers corresponds to each antenna.
```

```
"""
```

```
import matplotlib.pyplot as plt  
import pandas  
import numpy as np  
from operator import itemgetter
```

```
class ZaxisAnalysis:
```

```
    def typeTransfer(in_df):
```

```
        out = []
```

```
        in_df = in_df.dropna()
```

```
        for i in range(len(in_df)):
```

```
            out.append(in_df[i])
```

```
        return out
```

```
    def DrawFig(i, x, y, xmin, xmax, ymin, ymax, fname):
```

```
        xvar = xmax-xmin
```

```
        yvar = ymax-ymin
```

```
        fig = plt.figure(i)
```

```
        plt.plot(x, y, 'red', ls='None', marker='.')
```

```
        plt.xlim(xmin-xvar/25, xmax+xvar/25)
```

```
        plt.ylim(ymin-yvar/16, ymax+yvar/16)
```

```
        fig.savefig(fname + str(i) + "layer.png", transparent=False)
```

```
        return 0
```

```
    def launch(path, filename):
```

```
        df = pandas.read_csv(path + filename + '.csv')
```

```

x = ZaxisAnalysis.typeTransfer(df['x'])
y = ZaxisAnalysis.typeTransfer(df['y'])
z = ZaxisAnalysis.typeTransfer(df['z'])
xmin = min(x)
xmax = max(x)

ymin = min(y)
ymax = max(y)

zmin = min(z)
zmax = max(z)
zgap = int((zmax - zmin)/4)

xyz = np.transpose([x, y, z])
sortedlist = sorted(xyz, key = itemgetter(2))

x1 = []
x2 = []
x3 = []
x4 = []
y1 = []
y2 = []
y3 = []
y4 = []
z1 = []
z2 = []
z3 = []
z4 = []
i=0
for i in range(len(sortedlist)):
    if sortedlist[i][2] <= zmin + zgap*1:
        x4.append(sortedlist[i][0])
        y4.append(sortedlist[i][1])
        z4.append(sortedlist[i][2])
    elif sortedlist[i][2] <= zmin + zgap*2:
        x3.append(sortedlist[i][0])
        y3.append(sortedlist[i][1])
        z3.append(sortedlist[i][2])
    elif sortedlist[i][2] <= zmin + zgap*3:
        x2.append(sortedlist[i][0])
        y2.append(sortedlist[i][1])
        z2.append(sortedlist[i][2])
    else :
        x1.append(sortedlist[i][0])
        y1.append(sortedlist[i][1])
        z1.append(sortedlist[i][2])

ZaxisAnalysis.DrawFig(1, x1, y1, xmin, xmax, ymin, ymax, path + filename + "_xy_")
ZaxisAnalysis.DrawFig(2, x2, y2, xmin, xmax, ymin, ymax, path + filename + "_xy_")
ZaxisAnalysis.DrawFig(3, x3, y3, xmin, xmax, ymin, ymax, path + filename + "_xy_")
ZaxisAnalysis.DrawFig(4, x4, y4, xmin, xmax, ymin, ymax, path + filename + "_xy_")

```

```
plt.show()
```

✓ File 5: S0\_ANT\_comparison\_start.py

```
# -*- coding: utf-8 -*-
"""
Created on Tue Jan 7 16:22:19 2020

@author: WSK
@input: Four mp4 video files which are recorded at the top angle using different antenna types are
required.
@output: 1. Two csv files that include x,y,z coordinates and summary of frame numbers from
LED(color) detected frame according to each video file.
2. A plot that results in performance comparison by different antenna types.
"""

from S1_extract_xyz_from_video import Extractxyz
from S2_topview_analysis import TopViewAnalysis
from S3_detected_frames_comp import ComparisonPlot

def main():
    # Add folder path that includes four mp4 videos which can generate Figure 2(e).
    # For example, path=
    'C:\\Download\\3d_reconstruction\\01_Antenna_comparison_figure2_data\\'
    path= 'FILE_PATH_HERE\\'

    filename = 'Ant1_1W_top'
    Extractxyz.launch(path, filename + ".mp4", filename, 25, 90)
    TopViewAnalysis.launch(path, filename + ".csv", filename + "_rst.csv")

    filename = 'Ant2_1W_top'
    Extractxyz.launch(path, filename + ".mp4", filename, 25, 90)
    TopViewAnalysis.launch(path, filename + ".csv", filename + "_rst.csv")

    filename = 'Ant3_1W_top'
    Extractxyz.launch(path, filename + ".mp4", filename, 25, 90)
    TopViewAnalysis.launch(path, filename + ".csv", filename + "_rst.csv")

    filename = 'Ant4_1W_top'
    Extractxyz.launch(path, filename + ".mp4", filename, 25, 90)
    TopViewAnalysis.launch(path, filename + ".csv", filename + "_rst.csv")

    ComparisonPlot.launch(path, 'Ant_comparison_plot')

if __name__ == "__main__":
    main()
```

✓ File 6: S2\_topview\_analysis.py

```
# -*- coding: utf-8 -*-  
"""
```

```
Created on Thu Dec 12 08:27:13 2019
```

```
@author: WSK
```

```
@input: A csv file that includes x, y, z coordinates, and the number of frames that LED detected from  
the top angle of the cage is required.
```

```
@output: 1. A csv file that includes summary information of recorded data at top angle.
```

```
"""
```

```
import pandas
```

```
import numpy as np
```

```
class TopViewAnalysis:
```

```
    def Sort_fxya(f, x, y, a):
```

```
        def Sort(i,cnt):
```

```
            tmpA = a[i+cnt]
```

```
            result_cnt = cnt
```

```
            while(cnt):
```

```
                if(tmpA > a[i+cnt-1]):
```

```
                    cnt = cnt-1
```

```
                else:
```

```
                    tmpA = a[i+cnt-1]
```

```
                    cnt = cnt-1
```

```
                    result_cnt = cnt
```

```
            return result_cnt
```

```
sorted_val = []
```

```
cnt = 1
```

```
det = 1
```

```
fix = 0
```

```
i = 0
```

```
while (i < len(f)):
```

```
    while(det):
```

```
        if (i+cnt) == len(f):
```

```
            cnt = cnt-1
```

```
            det = 0
```

```
            break
```

```
        else:
```

```
            if f[i] == f[i+cnt]:
```

```
                cnt = cnt + 1
```

```
            else:
```

```
                cnt = cnt - 1
```

```
                det = 0
```

```
    if cnt == 0:
```

```
        sorted_val.append([f[i], x[i], y[i], a[i]])
```

```
    else:
```

```
        fix = Sort(i, cnt)
```

```
        sorted_val.append([f[i+fix], x[i+fix], y[i+fix], a[i+fix]])
```

```
    det = 1
```

```

        i = i + cnt + 1
    return sorted_val

def launch(path, ifilename, ofilename):

    df_top = pandas.read_csv(path + ifilename)

    top_f = df_top['f']
    top_x = df_top['x']
    top_y = df_top['y']
    top_a = df_top['a']
    top_frmNum = df_top['FrmNum']

    sorted_top = TopViewAnalysis.Sort_fxya(top_f,top_x, top_y, top_a)

    top_frmNum = top_frmNum[0] - sorted_top[0][0]
    xy_Num = len(sorted_top)

    xy_rst_list=[]
    xy_rst_list.append(['xy_total','xy_calculated'])
    xy_rst_list.append([top_frmNum, xy_Num])

    np.savetxt(path + ofilename, xy_rst_list,delimiter=",", fmt='%s')

```

✓ File 7: S3\_detected\_frames\_comp.py

```

# -*- coding: utf-8 -*-
"""
Created on Tue Dec 31 11:21:21 2019

@author: WSK
@input: Four csv files are required.
        Each file includes information on the total frame number and
        the number of extracted frames from the top angle(xy plane) according to the antenna design.
@output: 1. A plot of the antenna comparison result.

"""

import matplotlib.pyplot as plt; plt.rcParamsDefaults()
import numpy as np
import pandas
import matplotlib.pyplot as plt

class ComparisonPlot:

    def launch(path, ofilename):

        df1 = pandas.read_csv(path + 'Ant1_1W_top_rst.csv')
        df2 = pandas.read_csv(path + 'Ant2_1W_top_rst.csv')
        df3 = pandas.read_csv(path + 'Ant3_1W_top_rst.csv')

```

```

df4 = pandas.read_csv(path + 'Ant4_1W_top_rst.csv')

ant1 = df1['xy_total'][0]
ant1_xy = df1['xy_calculated'][0]
ant1_res = ant1_xy/ant1*100

ant2 = df2['xy_total'][0]
ant2_xy = df2['xy_calculated'][0]
ant2_res = ant2_xy/ant2*100

ant3 = df3['xy_total'][0]
ant3_xy = df3['xy_calculated'][0]
ant3_res = ant3_xy/ant3*100

ant4 = df4['xy_total'][0]
ant4_xy = df4['xy_calculated'][0]
ant4_res = ant4_xy/ant4*100

objects = ('1', '2', '3', '4')
y_pos = np.arange(len(objects))
performance = [ant1_res, ant2_res, ant3_res, ant4_res]

fig = plt.figure(1)
plt.bar(y_pos, performance, 0.45, align='center', alpha = 0.8, color = ('red', 'gray', 'gray', 'gray'))
plt.xticks(y_pos, objects)
plt.ylabel('Detected frame ratio')
plt.xlabel('Antennas')
plt.ylim(-10,120)

plt.show()

fig.savefig(path + ofilename + ".png", transparent=False)

```